

**Development and Application of an Area Recorded
Generalized Optical Scattering Technique**

by

SAAD ALI ALGARNI

A Dissertation

Submitted to the Faculty

of the

WORCESTER POLYTECHNIC INSTITUTE

In partial fulfillment of the requirements for the

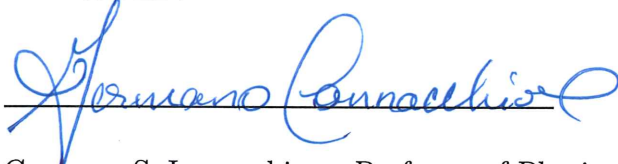
Degree of Doctor of Philosophy

in

Physics

Tuesday 16th December, 2014

APPROVED:



Germano S. Iannacchione, Professor of Physics, WPI, Advisor.



Padmanabhan K. Aravind, Professor of Physics, WPI.



Georgi Georgiev, Associate Professor of Physics, Assumption College

Abstract

A novel approach to a light scattering experiment that employs a lounge image capture assay has been developed for both static and dynamic measurement on a wide variety of samples. In this work, the "Development and Application of an Area Recorded Generalized Optical Scattering Technique", abbreviate as **ARGOS**, an approach is based on the placement of a translucent screen where the scattered light, now converted to a diffuse light, is imaged as a function of time. The placement and size of the screen determines the range of scattering wave-vectors, while the time between images determines the fastest dynamic resolvable . The overall experimental stability determines the slowest dynamic resolvable and so can be made arbitrarily long. The scattering intensity is measured by a camera whose dynamic range (number of bits per pixel) , resolution, and speed determines the sensitivity and accuracy of intensity of the scattered light. The system allows for an extremely well-defined scattering experiment geometry, where images may be manipulated to extract structure (i.e. $\langle I(q) \rangle_t$) and dynamics ($\langle I(q,t) \rangle_q$) for a wide range of samples(liquids and solids).

A number of innovation were developed. Instead of a beam stop to block the high intensity thru-beam, a thru-beam attenuator was developed such that the exact center of the scattering geometry is determined for each image acquired. A variety of image processing algorithms were also developed to correct for dead pixels, camera response, and intensity normalization. Of particular use was the development of the root-mean-square difference(RSD) image to probe dynamic. Here, the first image is taken as the time-zero reference image and subtracted from all succeeding images

where averaged over a specified q and plotted as a function of time revealing the build up image changes due to dynamics.

The technique was validated for both static and dynamic measurements with a set of dilute suspended latex spheres in water (sizes ranging from 0.01 to 2 μm). The static light scattering result in terms of particle radius and dimension closely matched the expected values.

The dynamic light scattering results could only reveal the end of the dynamics of these suspended latex spheres due to Brownian motion because of the speed limitation of the camera. However, sedimentation dynamics that are much slower, were early observed.

The ARGOS technique was then applied to two biological systems, the evolution of a dilute suspension of *E. Coli* bacteria through the life-cycle and the evolution of the same suspended bacteria but infected with the MS2 bacteria-phage virus. High temporal resolution data were obtained of the bacteria life-cycle which were correlated with size, structure, and dynamics that revealed potentially new insights on behavior not well understood in the literature . The MS2 infected bacteria revealed the effect of the bacteria-phage on every character of the *E. Coli* life-cycle. The successful development and implementation of ARGOS here has also revealed avenues to greatly improve the performance.

Acknowledgments

First and above all, I praise Allah, the almighty for providing me this opportunity and granting me the capability to proceed successfully.

This dissertation would have not seen the light in its current form without the assistance of several people during this work. I would therefore like to offer my sincere thanks to all of them.

Professor Iannacchione, my cordial thanks for your complaisance to accept me as a Ph.D student, your continuous encouragement, sober-minded guidance, pivotal comments, and organizing of the dissertation.

I would like to thank the members of the reading committee, Prof. Izabela Stroe. and Georgi Georgiev, for their excellent advice and detailed review during the preparation of this dissertation.

I want to express my deep thanks to my friend, Abigail Charest, for sharing with me her bacteria samples during part of this work, in addition great thanks to her for her brilliant ideas during our meeting and discussions.

I deeply thank, professor Alex Zozulya, for his help in the geometry correction for this work.

I would like to thank Hektor Kashuri, who pushed me towards the world of LabView. Also, big thanks to Roger Steele, for the trust, the insightful discussion, offering valuable advice and for his support during the whole period of the study.

Great thanks to Jackie Malone and Michele O'Brien for their spiritual support of

me during my PhD study.

Finally, I honestly can't express my thanks to my family for their support during my long trip in this dissertation. My mother and my father great thanks for your patience and support. Moreover, big thanks to my brothers and my sisters.

Saad Algarni

Tuesday 16th December, 2014

Worcester Polytechnic Institute

Worcester, MA

USA

Contents

List of Figures	vi
List of Tables	x
1 Introduction	1
1.1 Review of Light Scattering (LS)	1
1.1.1 What is Light Scattering?	1
1.1.2 Types of Light Scattering	2
1.1.2.1 Raleigh Scattering	2
1.1.2.2 Mie Scattering:	3
1.1.2.3 Tyndall Scattering:	4
1.1.2.4 Brillouin Scattering:	4
1.1.2.5 Raman Scattering:	4
1.2 Theoretical Background of Light Scattering	5
1.2.1 Static Light Scattering (SLS)	15
1.2.2 Dynamic Light Scattering (DLS)	19
1.2.2.1 Time-dependent Correlation Function	20

1.2.3	Measuring Scattered Light	22
1.2.4	Historical Review of LS	29
1.2.5	Development and Application of an Area Recorded General- ization Optical Scattering Technique ARGOS	33
2	Methodology	35
2.1	Hardware and Software	35
2.1.1	Devices and Tools	35
2.1.1.1	He-Ne Laser	35
2.1.1.2	CCD Monochrome USB Camera	36
2.1.1.3	Fixed Focal Length Lens	36
2.1.1.4	Anti-vibration Table	37
2.1.1.5	Screen and Beam Attenuator	37
2.1.1.6	Sample Holder	40
2.1.1.7	Slides Wafer	40
2.1.2	Sample Materials	42
2.1.3	Software	44
2.1.3.1	Laser Interaction with Particle Volume Program (LPV)	44
2.1.3.2	Taking Photos Program (TPP)	46
2.1.3.3	Total Photo Average Program (TPA)	47
2.1.3.4	Main Analysis Program (MAP)	48
2.2	Cell and Sample Procedure	49
2.2.1	Slides Cleaning Process	49
2.2.2	Sample Preparation	51
2.3	Experiment Set Up	55
2.3.1	Configuration	56
2.3.1.1	Laser Alignment	57

2.3.1.2	Optical Elements Arrangement	58
2.3.2	Calibration	60
2.3.2.1	Laser Stability	60
2.3.2.2	Dust Influence	61
2.3.2.3	CCD Pixels Defects	63
2.3.2.4	CCD Linearity	64
2.4	Images Capture Procedure	67
2.5	Data Analysis Methodology	69
2.5.1	Main Analysis Program (MAP)	69
2.5.2	Box Method Analysis Program (OAP)	75
2.5.3	Spherical to Plane Wave Front Correction	81
3	LATEX SPHERES	83
3.1	Results	83
3.1.1	Effect of Concentration	83
3.1.2	Static Light Measurements	85
3.1.2.1	Finding Radius of gyration by using Guinier Plot	85
3.1.2.2	Fractal Dimension Test	89
3.1.3	Dynamics Light Measurements	94
3.1.3.1	Defining The Root Square Difference	94
3.1.3.2	Sedimentation process	98
3.2	Discussion	101
3.2.1	Effect of Concentration	101
3.2.2	Static Light Scattering Measurements	101
3.2.2.1	Finding Radius of gyration by using Guinier Plot	101
3.2.2.2	Fractal Dimension Test	105
3.2.3	Dynamics Light Scattering Measurements	106

3.2.3.1	Studying The Root Square Difference	106
3.2.3.2	Sedimentation process	107
4	VIRUS INFECTED BACTERIA	108
4.1	Bacteria and Virus Background	109
4.2	Results	111
4.2.1	FAMP Characteristics	111
4.2.2	Topology of the FAMP	115
4.2.3	Fractal Dimension of the FAMP	116
4.2.4	Effective Radius	117
4.2.5	Four Panels Chart	119
4.2.6	Effect of Temperature change on FAMP	121
4.2.7	FAMP with MS2-Infection Characteristics	124
4.2.8	Topology of the FAMP with MS2-Infection	127
4.2.9	Fractal Dimension of the FAMP with MS2-Infection	128
4.2.10	Effective Radius of Infected FAMP	129
4.2.11	Four Panels of infected FAMP	130
4.2.12	FAMP and FAMP-MS2-infection Gallery	133
4.3	Discussions	139
4.3.1	FAMP Characteristics	139
4.3.2	Effect of Temperature Change	140
4.3.3	Topology of the FAMP	140
4.3.4	Fractal Dimension of the FAMP	141
4.3.5	Effective Radius	141
4.3.6	Four Panels Chart	142
4.3.7	FAMP with MS2-Infection Characteristics	143
4.3.8	Topology of the FAMP with MS2-Infection	143

4.3.9	Fractal Dimension of the FAMP with MS2-Infection	144
4.3.10	Effective Radius of Infected FAMP with MS2 Virus	144
4.3.11	Four Panels Chart of FAMP with MS2-Infection	144
4.3.12	FAMP and FAMP-MS2-infection Gallery	145
5	CONCLUSIONS	149
	Appendices	153
A	Programming Codes	A1
A.1	Laser interaction with Particle Volume	A1
A.1.1	LPV code	A1
A.2	Taking Photos Program	A2
A.2.1	TPP Codes	A3
A.3	Main Analysis Program (MAP)	A4
A.3.1	MAP Codes	A6
A.4	Box Analysis Program (OAP)	A12
A.4.1	Box Analysis Program codes	A14
B	Equipments and Materials	B1
B.1	Beam Filter	B1
B.2	The Wafer	B3
B.3	The Sample Holder	B5
B.4	<i>E. Coli</i> Sample Preparation	B5
	Bibliography	1

List of Figures

1.1	Redirection of light by obstacle.	5
1.2	Concept of Scattered Wave by Spherical Obstacle	8
1.3	Scattered light vectors	11
1.4	Difference between Rayleigh scattering and Mie scattering	17
1.5	Effect of different Particles sizes on Mie and Rayleigh scattering	18
1.6	Scattered Beam on Spherical particle	18
1.7	Scheme of the q-vector	19
1.8	Generic Light Scattering with Fractal Regimes.	28
1.9	General light scattering experiment configuration	30
1.10	Goniometer Technique	31
1.11	Multi Photo-multipliers Technique	32
1.12	Direct CCD Technique	33
1.13	ARGOS Technique	34
2.1	He-Ne Laser	35
2.2	CCD camera	36
2.3	The 16 mm focal lens	36

2.4	Anti-vibration Table	37
2.5	Semi translucent paper screen	38
2.6	Beam Attenuator	40
2.7	The specimen holder	41
2.8	Slides Wafer	42
2.9	The front panel of the LPV program	45
2.10	The interface of the TPP program	47
2.11	The panel of the TPA program	48
2.12	Draying Slides on the wafer	51
2.13	Experiment setting	56
2.14	Photo of the experiments on the anti vibration table	57
2.15	Laser stability	62
2.16	Camera Linearity	67
2.17	Donut Picture	71
2.18	MAP programs panel	74
2.19	Box method photo	75
2.20	The OAP input panel	78
2.21	OAP Output File	80
2.22	Correction Diagram	81
3.1	The effect of different concentrations	85
3.2	Plot of q^2 vs $\ln(I)$ for $2\mu\text{m}$	87
3.3	Plot of q^2 vs $\ln(I)$ for $1.0\mu\text{m}$	88
3.4	Plot of q^2 vs $\ln(I)$ for $0.5 \mu\text{m}$	89
3.5	Fractal Dimension for $2\mu\text{m}$	90
3.6	Fractal Dimension for $1.0\mu\text{m}$	91
3.7	Fractal Dimension for $0.5 \mu\text{m}$	92

3.8	Fractal Dimension for 0.5, 1.0, and 2.0 μm	93
3.9	Evolution of the R_Sq_Diffas a function of time at different q's for 2 μm	95
3.10	Different trends of the evolution of the R_Sq_Diffas a function of time for 2 μm at a single q	96
3.11	Relaxation Curve	97
3.12	Evolution of the R_Sq_Diffas a function of time for 1.0 μm	98
3.13	Evolution of the R_Sq_Diffas a function of time for 0.5 μm	99
3.14	Sedimentation of particle	100
4.1	E. Coli photo	109
4.2	Theoretical plot of FAMP	110
4.3	Intensity vs Time for FAMP	112
4.4	FAMP Root Square Difference	113
4.5	Two peaks FAMP	114
4.6	FAMP Topology	115
4.7	Fractal Dimension of FAMP	116
4.8	FAMP $\ln(I)$ vs q^2	117
4.9	Effective Radius of FAMP	118
4.10	FAMP 4 panels	120
4.11	Effect of hot and cold temp. on FAMP	122
4.12	Effect of hot and cold temp. on FAMP log-scale	123
4.13	Effect of FAMP cycle when infected by MS2	125
4.14	FAMP cycle life after infected by MS2	126
4.15	FAMP-MS2 Topology	127
4.16	FAMP-MS2 Fractal Dimension	129
4.17	FAMP-MS2 Effective Radius	130
4.18	FAMP-MS2 4 panels	132

4.19	FAMP-MS2 Life C. Comparison	135
4.20	Growth-Death FAMP-MS2	136
4.21	FAMP vs MS2 Fractal Dimension Comparison	137
4.22	FAMP MS2 Effective Radius Comparison	138
A.1	LPV CODE	A2
A.2	Taking Photos Code	A3
A.3	Taking Photos Code	A3
A.4	MAP Front Panel	A5
A.9	MAP Code	A11
A.10	OAP Front Panel	A13
A.16	OAP code	A20
B.1	Attenuator photos	B2
B.2	Wafer photo	B3
B.3	The wafer groves	B4
B.4	Sample Holder	B5

List of Tables

2.1	Dummy table which shows the information that were supplied to "Taking Photos Program" as it will be seen next.	46
2.2	Taking Photos Table Model. Here the first column is the selected number of photos and the second column determines the interval of time between images in seconds.	69
2.3	Table shows the out put of analysis by using MAP program. Where r is the distance from the center of the photo to point where q-intensity was measured.	72
3.1	Here are the 2, 1, and 0.5 μm latex spheres sizes that were resumed by using Mie's method. As it can be seen that Mie's method is more accurate for large sizes comparing to the smaller ones.	105
4.1	Differences between the three major points in FAMP's effective radius plot before infection in table [A] and after infection in table [B]. . . .	148

Chapter 1

Introduction

1.1 Review of Light Scattering

1.1.1 What is Light Scattering?

Deflection to the propagation of electromagnetic waves by a medium is called **scattering**. If these electromagnetic waves have wavelengths within the visible band, then this phenomena is called **Light Scattering (LS)**. In fact, most of what is visible to living creatures is a result of light scattering. Here it can be distinguished between two types (behaviors) of the scattered light (or photons in general), when light passes through any medium, the wavelength of the deflected (scattered) light is different from the original one, i.e, there is a change in the energy [1]. This kind of scattering is called *inelastic scattering* (Tyndall and Raman scattering [2]), but this type of scattering is out of the focus of this work. On the other hand, if the reflected light has a wavelength that is the same as the original one (Mie scattering [3] and

Raleigh scattering [4]), this is what is called *elastic scattering*, which is a focus of this work.

There are three parameters that are always associated with light scattering calculations. There are, the wave length of the incident beam, the medium refractive index n and the non-dimensional size parameter (\mathbf{x}) [5, 6]. The wavelength λ of the light and the refractive index n of the media will be integrated with parameter q , which is a very useful parameter in characterizing the scattered light [7]. The new quantity will be discussed in detail later. The parameter (\mathbf{x}) will be the bridge between the scattering regimes (Mie, Raleigh).

$$x = \frac{2\pi a}{\lambda}, \quad (1.1.1)$$

where a is the particle radius and λ is the wavelength of the scattered light.

This interaction between light and matter produces interference (speckles) which can be studied to extract useful information about the structure (static properties) and the dynamic properties as a cause of a slight shift in the wavelength of the incident light as an application of Doppler effect [8, 9].

1.1.2 Types of Light Scattering

1.1.2.1 Raleigh Scattering

Raleigh scattering is also called elastic scattering. It occurs from scattered light on small particles (1 to 100 nm when using a $\lambda = 633$ nm He-Ne laser source). This type of scattering causes the color of the sky [10], as well as the colors observed from

shade of soap bubbles and red of sunset [11]. It is also one major effect of the loss of signal strength in communication by fiber optics [12].

The particle size and the light wavelength have a major effect in the intensity strength of the scattered light, where if I is the intensity of the scattered light of wavelength λ , I is $\propto 2R$ by a factor of 10^6 , where R is the radius of the particle. On the other hand, I is $\propto \lambda$ by a factor 10^{-4} [13].

Raleigh scattering is a special case of Mie scattering, and it is usually the preferable analysis regime when studying small spherical particles $\sim 1/20$ of the light source's wave length. It also helps to avoid the complexity of Mie interpretation.

1.1.2.2 Mie Scattering:

This kind of scattering represents the effect of scattering more or less equally by any particle's size. Mie scattering is an appropriate analysis method [14] when the indecent light is scattered off by particles larger than those in Rayleigh scattering (≥ 100 nanometer).*

Mie scattering intensity (I) is scattering angle dependent (θ), as well as proportional to the solvent refractive index (n_d) and the wave length of the source (λ). All of these parameters are represented the scattering wave vector (q) [15].†

*Mie can also be used for small particles, but this adds unnecessary complexity to the calculations which can be avoided by using Raleigh method. Also it has no limit on the size of the particles.

†This parameter (q) will talk discussed in detail later in the experimental part.

1.1.2.3 Tyndall Scattering:

When laser beam is scattered inside a colloid solution, this is called Tyndall scattering. Blue light (shorter wave length) scatters more than longer wave length (such as red light). This kind of scattering will not be covered in this work.

1.1.2.4 Brillouin Scattering:

Photons that hit acoustic phonons[‡], usually in a solid, produces Brillouin scattering. This kind of scattering is inelastic, so the loss of energy creates the Stokes or the anti-Stokes process. Where as in Stokes case, the energy of the scattered wave is lower in energy than the incident wave, while the anti-Stokes case, the energy of the scattered wave will have a higher energy then the incident one. [18]

1.1.2.5 Raman Scattering:

Raman scattering is an inelastic scattering with optical phonons instead of acoustic scattering such as in Brillouin. The intensity and the energy in Raman scattering are much larger than Brillouin, so the produced spectrum lines are stronger than those of Brillouin. This makes Raman scattering very useful for chemical spectroscopy [19]. Raman differs from elastic Raleigh scattering, where there is no change from the frequency of the incident photon. Raman occurs when the absorbed photons are emitted with a slightly different frequency (Stokes and anti-Stokes' phenomena).

[‡]Phonons can be represented as quanta of vibrational energy in the acoustic frequency range. Solid state or QED books describe the meaning of this phenomena, for example check these two references [16,17].

1.2 Theoretical Background of Light Scattering

When a polarized electric field of wavelength λ propagates linearly towards a particles (e.g. molecules) along the x-direction, the equation which describe this system will take this form :

$$E(x, t) = E_0 \cos(kx - \omega t + \phi), \quad (1.2.1)$$

where, k is the wave number, ω is the angular frequency, and ϕ is the phase.

Maxwell equations describe the propagation of electromagnetic waves (light) when it has been redirected by obstacles [20]. See Fig.(1.1).

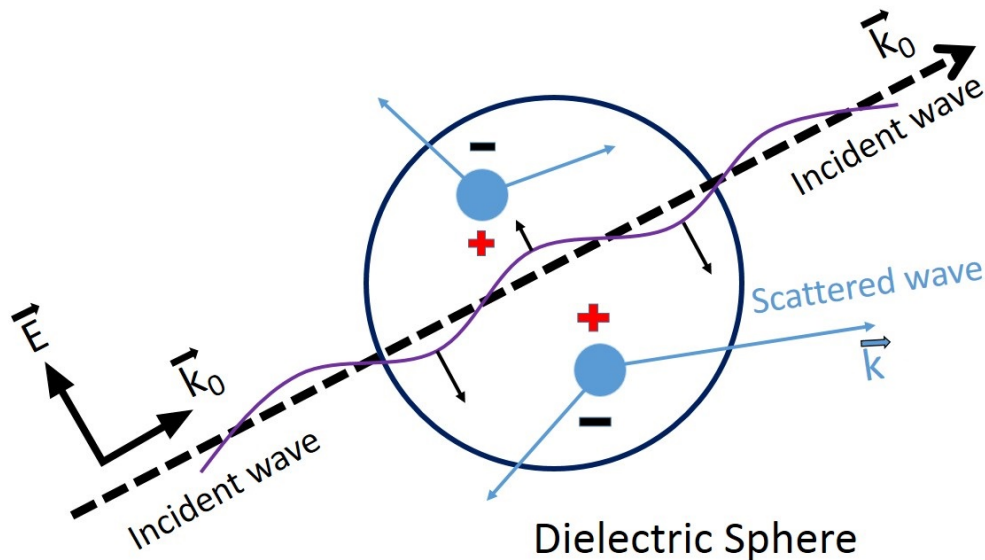


Figure 1.1: This figure shows the redirection of light when it encounters an obstacle. Inside the sphere the charge dipole which is presented by two blue circles can be seen.

$$\begin{aligned}
\nabla \times \mathbf{H} &= \frac{1}{c} \frac{\partial \mathbf{D}}{\partial t} + \frac{4\pi}{c} \mathbf{j}, \\
\nabla \times \mathbf{E} &= -\frac{1}{c} \frac{\partial \mathbf{B}}{\partial t}, \\
\nabla \cdot \mathbf{D} &= 4\pi\rho, \\
\nabla \cdot \mathbf{B} &= 0.
\end{aligned}
\tag{1.2.2}$$

So, from the elastic scattering where $|\vec{k}_i| = |\vec{k}_f|$, which can be either Rayleigh scattering or Mie scattering .

Solution of Mie Scattering

Most of this section is based on a paper by Professor Kuo-Nan. See Ref. [21]. Also for more detailed information about Mie solution see Ref. [22, 23].

Mie solution refers to a solution of Maxwell equations with specific constraints. These constraints are as follows: First, obstacles are assumed to be spheres, second, these particles are homogeneous (i.e. all have the same refractive index). The Mie approach has no limits on the size of the scattering particles whenever they are comparable to the wavelength, as well as the absorption of light. So in this sense it is a general solution. As it will be seen later , Rayleigh scattering will be a special case of Mie scattering formalism .

As a result of the vector electromagnetic theory, a harmonic wave of the form $e^{-i\omega t}$ can be a solution of the scalar wave equation:

$$\frac{1}{r^2} \frac{\partial}{\partial r} \left(r^2 \frac{\partial \psi}{\partial r} \right) + \frac{1}{r^2 \sin \theta} \frac{\partial}{\partial \theta} \left(\sin \theta \frac{\partial \psi}{\partial \theta} \right) + \frac{1}{r^2 \sin^2 \theta} \frac{\partial^2 \psi}{\partial \phi^2} + k^2 m^2 \psi^2 = 0. \quad (1.2.3)$$

As well as satisfying Maxwell's reduced equations in the special case of uniform optical medium (free of charge):

$$\begin{aligned} \nabla \times \mathbf{H} &= -i\omega\epsilon\mathbf{E}, \\ \nabla \times \mathbf{E} &= i\omega\mu\mathbf{H}, \\ \nabla \cdot \mathbf{E} &= 0, \\ \nabla \cdot \mathbf{H} &= 0, \end{aligned} \quad (1.2.4)$$

where, ϵ is the permittivity [24] and ω is the permeability of the media.

By solving the wave Eq.(1.2.3) in spherical coordinates by using separation of variables for r , θ and ϕ , and by applying the boundary conditions at the surface of the particle, we result in the Legendre functions, spherical harmonics, and modified Bessel functions of half integer order.

The following is a brief description of this process:

Based on Mie theory the light scattering by a spherical particle in non-absorbing media is formalized in this work. See Fig.(1.2). If the media absorbs some of the light , then some modification of the Mie equations will be required [25].

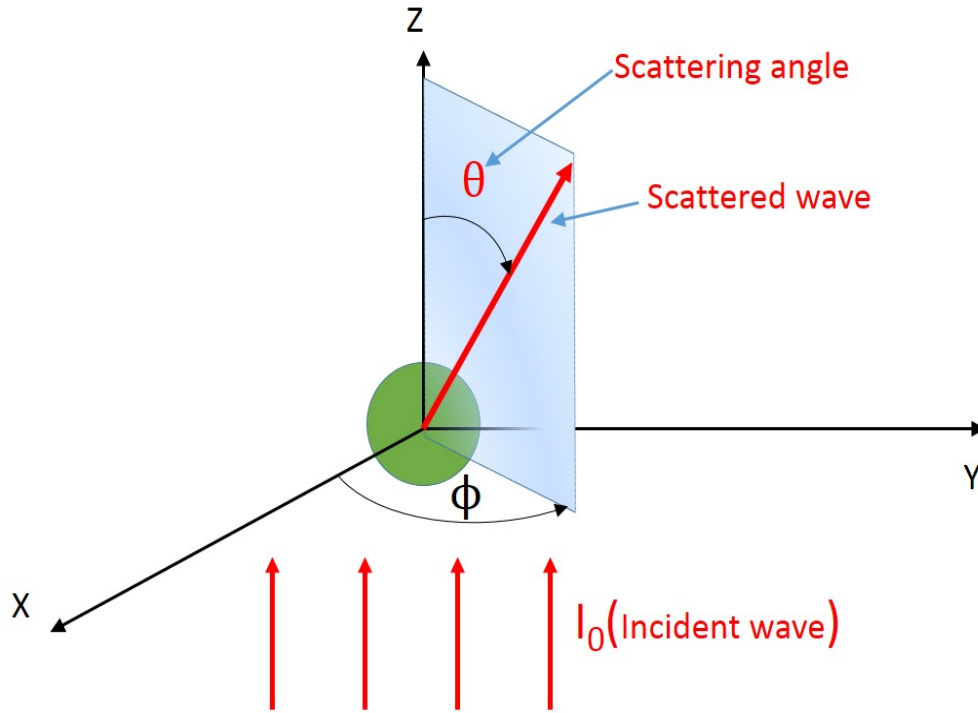


Figure 1.2: This scheme shows the concept of scattered wave by a spherical dielectric obstacle, where the incident beam intensity is I_0 which has an energy E flows towards the Z direction, ϕ is the angle of the planes which encloses the scatter wave vector, and θ is the angle of scattering.

For far-field[§], the two scattering amplitudes can be represented as [26] :

$$S_1(\theta) = \sum_{n=1}^{\infty} \frac{2n+1}{n(n+1)} [a_n \pi_n(\cos\theta) + b_n \tau_n(\cos\theta)], \quad (1.2.5)$$

$$S_2(\theta) = \sum_{n=1}^{\infty} \frac{2n+1}{n(n+1)} [b_n \pi_n(\cos\theta) + a_n \tau_n(\cos\theta)]. \quad (1.2.6)$$

So, if the incident light is unpolarized, the scattering intensity (I_s) is correlated to

[§]Far-field means that the scattering angle is relatively small so that $\sin(\theta) \approx \theta$.

the scattering amplitude functions[¶] (S_1 & S_2) as:

$$I_s \propto |S_1|^2 + |S_2|^2. \quad (1.2.7)$$

where, a_n and b_n are the scattered wave coefficients:

$$a_n = \frac{\Psi'_n(mx)\Psi_n(x) - m\Psi_n(mx)\Psi'_n(x)}{\Psi'_n(mx)\xi_n(x) - m\Psi_n(mx)\xi'_n(x)}, \quad (1.2.8)$$

$$b_n = \frac{m\Psi'_n(mx)\Psi_n(x) - \Psi_n(mx)\Psi'_n(x)}{m\Psi'_n(mx)\xi_n(x) - \Psi_n(mx)\xi'_n(x)}. \quad (1.2.9)$$

where, Ψ_n and ξ_n are related to spherical Bessel functions.

The two functions π_n and τ_n can be written in this form:

$$\pi_n(\cos\theta) = \frac{1}{\sin\theta} P_n^1(\cos\theta), \quad (1.2.10)$$

$$\tau_n(\cos\theta) = \frac{d}{d\theta} P_n^1(\cos\theta) \quad (1.2.11)$$

So, at the far-field approximation, the components of the electric field vectors. See Fig.(1.3), can be expressed as the following:

$$E_\theta^s = -\frac{i}{kr} e^{-ikr} \cos\phi S_2(\theta), \quad (1.2.12)$$

$$-E_\phi^s = -\frac{i}{kr} e^{-ikr} \sin\phi S_1(\theta). \quad (1.2.13)$$

Thus,

$$E_r^s = -E_\phi^s, \quad (1.2.14)$$

$$E_t^s = E_\theta^s \quad (1.2.15)$$

[¶]Scattering amplitude can be defined as the outgoing spherical-wave amplitude relative to the incoming plane-wave [27].

But the perpendicular (E_r) and the parallel (E_l) electric field are:

$$E_r^i = e^{-ikz} \sin\phi, \quad (1.2.16)$$

$$E_l^i = e^{-ikz} \cos\phi. \quad (1.2.17)$$

So, the complete matrix which describes the electric field at a far distance from the scattering particles is:

$$\begin{pmatrix} E_l^s \\ E_r^s \end{pmatrix} = \frac{e^{-ikr+ikz}}{ikr} \begin{pmatrix} S_2(\theta) & 0 \\ 0 & S_1(\theta) \end{pmatrix} \begin{pmatrix} E_l^i \\ E_r^i \end{pmatrix}. \quad (1.2.18)$$

So, the scattering intensity components I^s in the far-field can be written as follows :

Let's define $i_1(\theta)$ & $i_2(\theta)$ to simplified the calculations as,

$$i_1(\theta) = |S_1(\theta)|^2,$$

$$i_2(\theta) = |S_2(\theta)|^2.$$

so,

$$I_l^s = I_l^i \frac{i_2}{k^2 r^2}, \quad (1.2.19)$$

$$I_r^s = I_r^i \frac{i_1}{k^2 r^2}. \quad (1.2.20)$$

where, l indicates the parrallel direction and r indicates to the radial perpendicular direction.

$$(1.2.21)$$

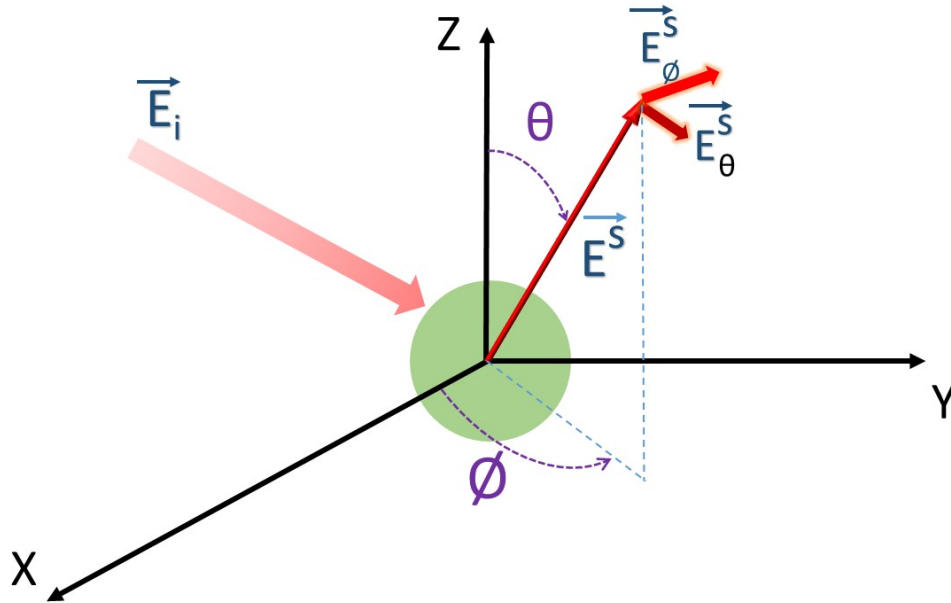


Figure 1.3: The geometry of the two electric field vectors (\vec{E}_θ^S & \vec{E}_ϕ^S) which are produced after the light of electric field \vec{E}_i incident on a spherical particle.

If the source of the light is partially linearly polarized, the scattered intensity will have this form:

$$I = I_0 \frac{i_1 + i_2}{2k^2 r^2}, \quad (1.2.22)$$

and the degree of polarization will be:

$$P = I_0 \frac{i_1 - i_2}{i_1 + i_2}. \quad (1.2.23)$$

The total losses of energy from the incident beam due to both scattering absorption processes (extinction cross section) [28] and the scattering cross section can be

defined as :

$$\begin{aligned}\sigma_{ext} &= \frac{4\pi}{k^2} \text{Re}[S(0)], \\ \sigma_{sca} &= \frac{\pi}{k^2} \int_0^\pi [i_1(\theta) + i_2(\theta)] \sin(\theta) d\theta.\end{aligned}\tag{1.2.24}$$

At the same time, the extinction efficiency for a sphere of radius a can be defined as,

$$Q_{ext} = \frac{\sigma_{ext}}{\pi a^2} = \frac{2}{x^2} \sum_{n=1}^{\infty} (2n+1) \text{Re}(a_n + b_n).\tag{1.2.25}$$

Also, the scattering efficiency for a sphere of radius a can take the form ,

$$Q_{sca} = \frac{2}{x^2} \cdot \sum_{n=1}^{\infty} (2n+1) (|a_n|^2 + |b_n|^2)\tag{1.2.26}$$

And the absorption cross-section and efficiency can be written as,

$$\sigma_{abs} = \sigma_{ext} - \sigma_{sca},\tag{1.2.27}$$

$$Q_{abs} = Q_{ext} - Q_{sca}.\tag{1.2.28}$$

The electromagnetic field scattered by a sphere is mostly polarized elliptically. So, \mathbf{E} from Eq.(1.2.18) can take the form :

$$E = \text{Re}(E_l \hat{l} + E_r \hat{r}),\tag{1.2.29}$$

where r and l are the circular bases.

The **Stokes'** parameters (I , Q , U and V) and **the phase** matrix [29] are quantities always involve in electromagnetic polarization^{||} which are caused by intensity interactions with matter [30]. These parameters can be described in these mathematical forms:

$$I = |\mathbf{E}_l|^2 + |\mathbf{E}_r|^2, \quad (1.2.30)$$

$$Q = 2\text{Re}(E_l^* E_r), \quad (1.2.31)$$

$$U = -2\text{Im}(E_l^* E_r), \quad (1.2.32)$$

$$V = |\mathbf{E}_l|^2 - |\mathbf{E}_r|^2. \quad (1.2.33)$$

The Stokes parameters [31] of theses quantities which due to the scattered wave from spherical particles can be represented as follows:

$$\begin{bmatrix} I \\ Q \\ U \\ V \end{bmatrix} = M \begin{bmatrix} I_0 \\ Q_0 \\ U_0 \\ V_0 \end{bmatrix} \quad (1.2.34)$$

^{||}These parameters are great tools for light scattering computational work.

where,

$$M = \begin{bmatrix} M_{11} & M_{12} & 0 & 0 \\ M_{12} & M_{11} & 0 & 0 \\ 0 & 0 & M_{33} & -M_{34} \\ 0 & 0 & M_{34} & M_{33} \end{bmatrix} \quad (1.2.35)$$

Thus,

$$(1.2.36)$$

$$M_{11} = \frac{1}{2k^2r^2}[S_1(\theta)S_1^*(\theta) + S_2(\theta)S_2^*(\theta)], \quad (1.2.37)$$

$$M_{12} = \frac{1}{2k^2r^2}[S_2(\theta)S_2^*(\theta) - S_1(\theta)S_1^*(\theta)], \quad (1.2.38)$$

$$M_{33} = \frac{1}{2k^2r^2}[S_2(\theta)S_1^*(\theta) + S_1(\theta)S_2^*(\theta)], \quad (1.2.39)$$

$$-M_{34} = \frac{i}{2k^2r^2}[S_1(\theta)S_2^*(\theta) + S_2(\theta)S_1^*(\theta)]. \quad (1.2.40)$$

The matrix M is the transformation matrix for a single sphere. Also the phase matrix can be represented as follows:

$$P(\theta) = \frac{1}{C}M(\theta), \quad (1.2.41)$$

$$\text{where, } C = \frac{\sigma_{sca}}{4\pi r^2}.$$

1.2.1 Static Light Scattering (SLS)

If a scattered wave E_r was emitted by an oscillation dipole. See Fig.(1.1). The intensity of this wave can be described by this equation:

$$I_r = E_r E_r^*, \quad (1.2.42)$$

where,

$$\mathbf{E}_r = \frac{-4\pi^2\nu\alpha E_0}{rc^2} \exp[i(2\pi\nu t - \vec{k} \cdot \vec{r})], \quad (1.2.43)$$

where, ν is the frequency of the scattered light, and α is the polarizability. So, scattering from small particles ($2R \leq \frac{\lambda}{20}$) is independent of the scattering angle θ . This range is known as the **Rayleigh** region.

The intensity of such scattering (from unpolarized source) is inversely proportional to the power four of the wave length of the light, $I \propto \lambda^{-4}$ and it can be calculated as :

$$I = I_0 \frac{8\pi N \alpha^2}{\lambda^4 r^2} (1 + \cos^2(\theta)). \quad (1.2.44)$$

While, the polarizability approximation can be written as :

$$\alpha \simeq \frac{1}{4\pi N} (n^2 - 1), \quad (1.2.45)$$

where, N is the number of the scatterers, I_0 is the toluene intensity, and r is the distance from the scatterers.

So, the cross section for Rayleigh becomes much easier than the more general form in Eq.(1.2.26), which can be shown in analytic form as:

$$\sigma_{Ray} = \frac{8\pi}{3} \left(\frac{2\pi n_m}{\lambda} \right)^4 a^6 \left(\frac{m^2 - 1}{m^2 + 2} \right)^2. \quad (1.2.46)$$

where n_m is the ratio of the particle's refractive index with respect to the surrounding media, and a is the radius of the particle.

Also, the optical density, D_{opt} can be measured experimentally as :

$$D_{opt} = \log\left(\frac{I_0}{I(L)}\right), \quad (1.2.47)$$

where, L is the laser path length. So the experimental cross section becomes,

$$\sigma = \frac{D_{opt} \ln(10)}{\rho L}. \quad (1.2.48)$$

where, ρ is the number density.

On the other hand if large particles of diameters greater than 100 nm** were in a dilute solution, the system would be considered to be in the **Mie** regime ††. The differences between Rayleigh and Mie can be shown in Figs.(1.4) and (1.5) [32]. For small particles where the parameter $x \ll 1$, Eq.(1.1.1), Mie's produces the same scattering cross sections as Rayleigh. [8]

The scattered intensity of the Mie case is dependent on the scattering angle θ . This angle is combined with other parameters in one useful quantity called the scattering

**If particles' sizes are greater than the wavelength of the light, the Mie phenomena will be more obvious.

††Mie is the general solution , so it works fine for all sizes but is a more complicated analysis.

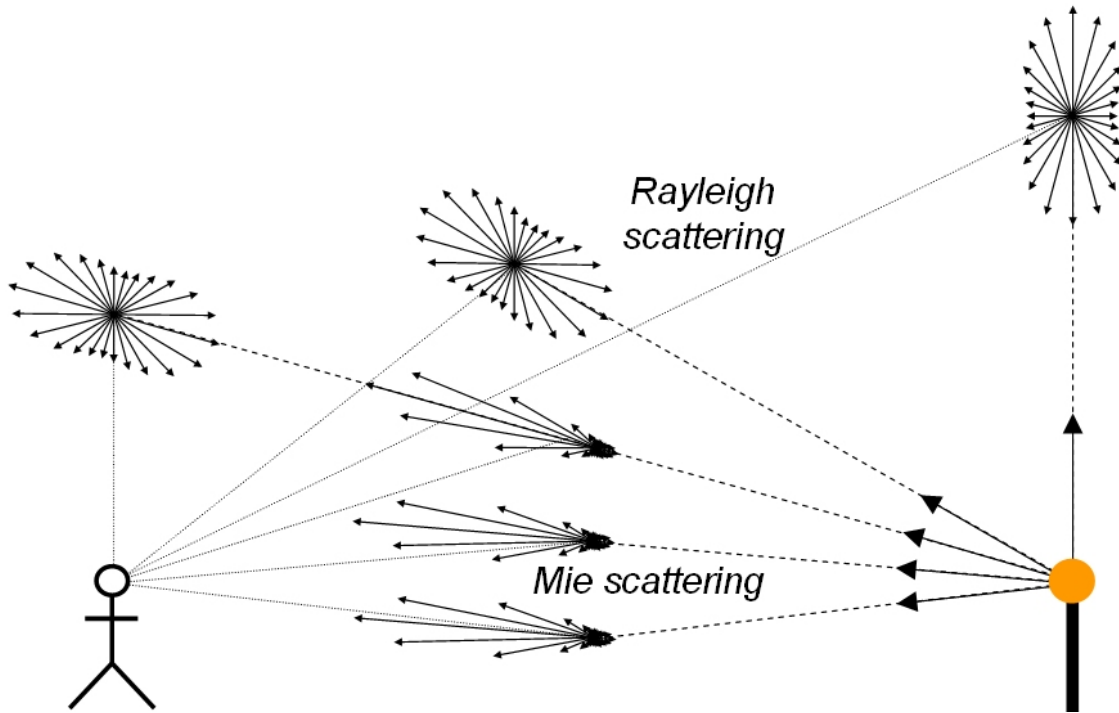


Figure 1.4: This figure shows the difference between Rayleigh scattering and Mie scattering. Where it can be seen that Rayleigh scattering mostly propagates homogeneously in all directions, while Mie scattering mostly propagates directionally. [32]

vector \mathbf{q} in [cm^{-1}] Fig.(1.7), which is independent of the contributions of the rotational and internal motion of the particles, moreover this quantity fortunately can be measured in the lab directly.

So, suppose an incident light of wave-vector \vec{k} scattered by a sphere particle of radius a . See Fig.(1.6). The scattering vector \mathbf{q} can thus be calculated as follows:

$$|\vec{q}| = q = \frac{4\pi n_d \sin(\frac{\theta}{2})}{\lambda}. \quad (1.2.49)$$

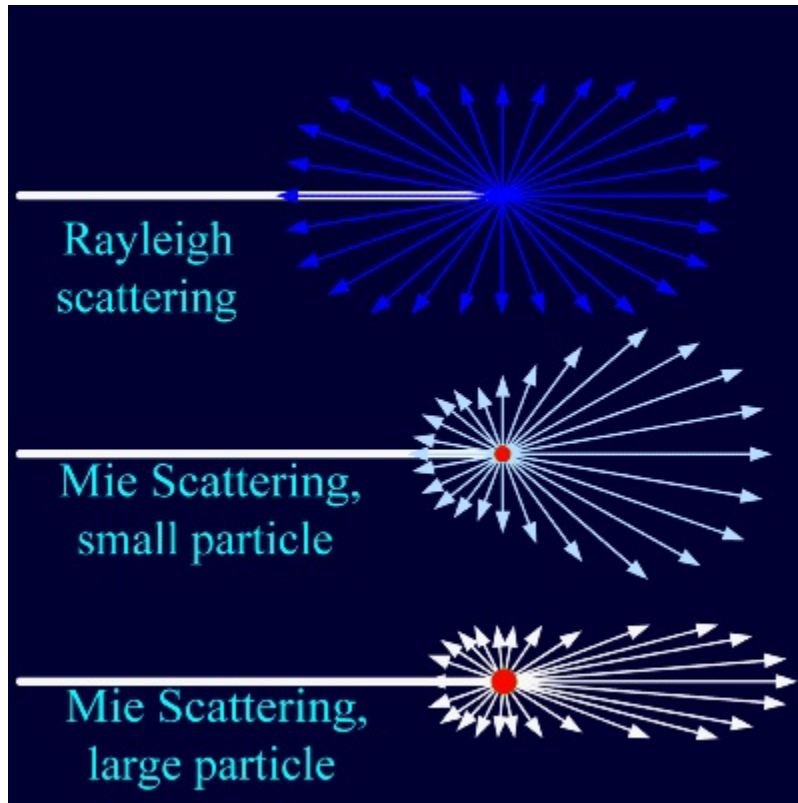


Figure 1.5: *The difference between Rayleigh scattering and Mie scattering for different particles sizes, where small particles scatter the light in wider angle more than large particles. [32]*

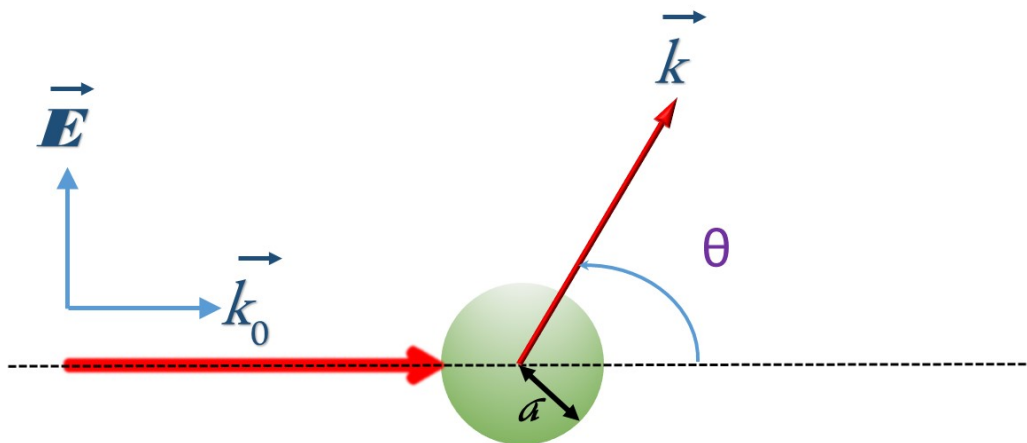


Figure 1.6: *The Scattering of an incident beam by a spherical particle of radius a , where \vec{k}_0 is the wave number for the incident beam and \vec{k} is the wave number for the scattered one. Also, it can be seen the scattered angle θ in this figure.*

where, \vec{q} is nothing but $\vec{k} - \vec{k}_0$ and \vec{k} is the wave vector as shown in Fig.(1.7), and n_d is the refractive index of the solution.

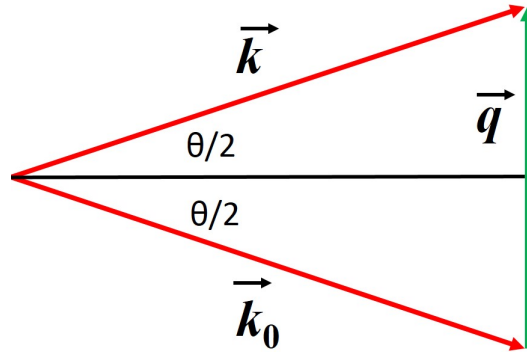


Figure 1.7: The geometry concept of \vec{q} which is correlated to the wave number \vec{k}_0 as an incident wave and \vec{k} as a scattered wave. Also, this figure shows the meaning of $\frac{\theta}{2}$ angle.

1.2.2 Dynamic Light Scattering (DLS)

While the fluctuation in the scattered intensity at different angles is the method of using SLS, on the other hand in dynamic light scattering, time is an issue in the experiment setup and in the analysis.

The random location in which the particles move in the media is known as the Brownian motion. To understand this concept, knowledge of the probability density

function is essential. This function can be represented mathematically as:

$$P = (4\pi Dt)^{-3/2} \exp\left(\frac{-r^2}{4Dt}\right), \quad (1.2.50)$$

where D is the diffusion coefficient [33], which can be calculated from the Stoke-Einstein equation given by:

$$D = \frac{k_B T}{6\pi\eta a}, \quad (1.2.51)$$

where, η is the viscosity, a is the particle radius, and T is the temperature in Kelvin.

From Eq.(1.2.51), if the diffusion constant is known, the particle size, called the hydrodynamic radius $R_H = a$, can be determined [34].

1.2.2.1 Time-dependent Correlation Function

The autocorrelation function is one of the powerful techniques that have used to study the dynamics light scattering for decades. According to Bruce J. Berne and Robert Pecora in their book "Dynamic Light Scattering With Applications to Chemistry, Biology and Physics" [35], the correlation function can be defined as: "Correlation function provide a concise method for expressing the degree of which two dynamical properties are correlated over a period of time."

So, the correlation process is nothing but the averaging of events (interactions between particles) over time. In the light scattering process, there is a fluctuation in intensity which is caused by the interaction between the light source (laser in this

work) and the surrounding environment will be logical mathematically when the time interval of this event is much larger than the period of this event [36]. So, in other words, correlation function studies the fluctuation of laser between two intervals of time (shorter intervals of time will mean more accurate depending on the dynamic for this event). So the time-dependent correlation function for this event is :

$$\langle A \rangle = \lim_{T \rightarrow \infty} \frac{1}{T} \int_0^T dt A(t). \quad (1.2.52)$$

For the small interval of time $\tau < t$, The auto correlation function takes the form:

$$\langle A(t)I(\tau) \rangle = \lim_{T \rightarrow \infty} \frac{1}{T} \int_0^T dt A(t) A(t + \tau).$$

And the special density $I_A(\omega)$ of the T-dependent correlation function $\langle A^*(0)A(t) \rangle$ is [35] :

$$I_A(\omega) = \frac{1}{2\pi} \int_{-\infty}^{\infty} dt e^{-i\omega t} \langle A^*(0)A(t) \rangle . \quad (1.2.53)$$

So, the dynamic light scattering correlation function is :

$$\begin{aligned} G(\tau) &= \int_0^T dt I(t) I(t + \tau) \\ &= B + A e^{-2q^2 D \tau}, \end{aligned} \quad (1.2.54)$$

where q is the scattering wavevector, see Eq.(1.2.49), A and B are constants. So D the diffusion coefficient can take the form :

$$D = \frac{C k_B T}{2\pi\eta R_H}, \quad (1.2.55)$$

where, C is a constant that depends on particle size and shape. [37]

The hydrodynamic radius is one of the characteristics that DLS can determine with precision if the diffusion coefficient D can be calculated as it can be seen in Eq.(1.2.55). So, if N particles of each has a radius R were dispersed in solution of a viscosity η , so, for the Brownian motion [38] to change the position of each particle by traveling a distance equal to its radius R , where, a time t_{cr} is needed for this trip a cross the distance R .

1.2.3 How to Measure Scattering Light

After discussing some background information about the light scattering phenomena, the next step will be about the practical techniques that were mostly used to extract the physics properties of samples that were exposed to the light scattering phenomena.

Light scattering is a very powerful tool to study particles properties, and when the experiment arrangement is correctly set, results will be exceptional , even with minimum corrections and calibrations. [39]

1. **Static Light Scattering** By placing a sample in the path of a high intensity

monochromatic light source (usually lasers), measuring the intensity of the scattered rays at different angles to obtain some static physical properties, like radius of gyration R_g as an example, also, by measuring the intensity vs different concentrations, the average molecular weight M and the second virial coefficient A_2 [40] can be calculated, as an other example, that what is titled as (SLS). [41,42]

All samples in this work were made of diluted solutions so as to have a single scattering process.

- **Guinier Plot** Guinier law [43] is one of the simplest method to use when calculating one of the static properties of particles that dispersed in solution, such as the radius of gyration R_g , under the constrain($q \times R_g \leq 1$) as follows : Any scattered wave has an amplitude $f(q)$ that can be represented mathematically in this form:

$$f(q) = \int_V dV \cdot \rho(\mathbf{r}) e^{-i\mathbf{q} \cdot \mathbf{r}} \quad (1.2.56)$$

If the distance between two points is \mathbf{r} where each point has a slight difference in density from the other, the scattering intensity caused by these two points can be expressed as :

$$I(q) = V \int_0^\infty 4\pi r^2 \gamma(r) \frac{\sin(qr)}{qr} dr,$$

where, $\gamma(r)$ is the correlation function, and V is the scattering volume.

So, if there is no interaction between particles, so the intensity of scattering can be written as follows:

$$I(q) = I(0)e^{(-1/3 q^2 R_g^2)}. \quad (1.2.57)$$

This last equation is known as Guinier's law or Guinier's function. [44,45].

- **Debye Plot.** where the Particle Form Factor is defined as:

$$P(q) = 1 + \frac{s^2 q^2}{3} + \dots \quad (1.2.58)$$

where, q is the scattering wavevector look at Eq.(1.2.49), and s is the distance between any two points on the scatterers, where the two points can be exposed to the incident wave and the scattering is occurs.

This particle form factor $P(q)$ can be written in a more simple way without concerning of the rest terms of the series expansion. So for a special cases of large spherical particles, this function can be written as follows: [46]

$$P(q) = \frac{9}{(qR)^2} (\sin(qR) - qR \cos(qR))^2, \quad (1.2.59)$$

where R is the radius of particle.

This equation is embedded in a very useful equation called the Zimm equation which can be used as a simple technique to analyze small par-

ticles between 10 and 50 nm [46] as follows :

$$\frac{K c}{R} = \frac{1}{M(1 + \frac{s^2 q^2}{3})} + 2A_2 c, \quad (1.2.60)$$

where A_2 is the second Virial coefficient, c is the mass concentration, M is the particle molar mass, and K is the construct factor as follows:

$$K = \frac{4\pi^2 n^2 (dn/dc)^2}{N_A \lambda^4},$$

where n is the refractive index for the solution, N_A is Avogadro's number, λ is the wave length of the laser, and dn/dc the change in refractive index of the solution with change in concentration. Also, R in Zimm equation can be written in this form :

$$R = \frac{d^2}{\sin^2(\theta)} \frac{I_s}{I_0}, \quad (1.2.61)$$

where θ is the scattering angle, d is the distance from sample to the detector such that $d = |r|$. I_s is the scattering light intensity, and I_0 is the intensity of the toluene. [47]

It must be kept in mind that to apply the previous Eq.(1.2.60), it has to be assumed first, that the particles are identical in shape and size. If this is not so, then it will be needed to apply the averages to some of its quantities depending upon those which are identical and those which are

not. Also for a small angle where $p(q) = 0$ this equation can take the simpler form:

$$\frac{K c}{R} = \frac{1}{M} + 2A_2c. \quad (1.2.62)$$

- **Fractal Dimension.**

For any particle of radius R and mass of M there is a useful relation [46] as follows:

$$M(R) \sim R^d \quad (1.2.63)$$

where, d is called Fractal Dimension, which is symbolized sometimes as d_f , where this fractal dimension differs based on the shape of objects [48]. If light scattering were to occur, then the relation between the intensity I and the scattering wavevector can be written as:

$$\log[I(q)] = -d \cdot \log(q) \quad (1.2.64)$$

So, Eq.(1.2.64) can be used as a tool to determine the topology of the particles by plotting $\log_{10}(I)$ vs $\log_{10}(q)$ at the zone where $q \times R \approx 1$, the slope is nothing but the Fractal Dimension d or d_f [46].

- **Structure Factor.**

The Generic demonstration of scattering with a fractal dimension d_f for particles of radius of gyration R_g is shown in Fig(1.8), where the Porod

regime is applied in the case of that the structure factor function($S(q)$)^{††} is proportional to $((q \times a)^{-4})$ and a is the monomer radius. So based on the quantity $q \times R_g$ (regime), the structure factor takes these forms:

$$S(q) = e^{-(qR_g)^{2/3}}, \quad (1.2.65)$$

where $q \times R_g$ is small and obeys Guinier law. Also, for large $q \times R_g$, the structure factor takes this form;

$$S(q) = C (qR_g)^{-d_f}, \quad (1.2.66)$$

where C is the boundary between small and large $q \times R_g$. Moreover, R_g^{-1} in Fig(1.8) is equivalent to $q \times R_g = 1$, as well as a^{-1} is equivalent to $q \times a = 1$ [50].

2. Dynamic Light Scattering (DLS)

This is also referred to as Quasi-Elastic Light Scattering (QELS) caused by the Brownian motion phenomenon. For example, if spherical particles were dispersed in some solvent, these particles will keep moving randomly in the solvent. Consequently, when light scatters from the moving particles, this random motion causes a randomness to the scattered light phase. As the scattered rays from the different particles are added together, they will lead to destructive or constructive interferences, which will then lead to time dependence in the intensity fluctuations of the scattered light. Moreover, fluctuation of the laser is due to the behavior of the small particles in solutions which are under

^{††}The structure factor is the normalized of the total scattered intensity over the number of scatterers [49].

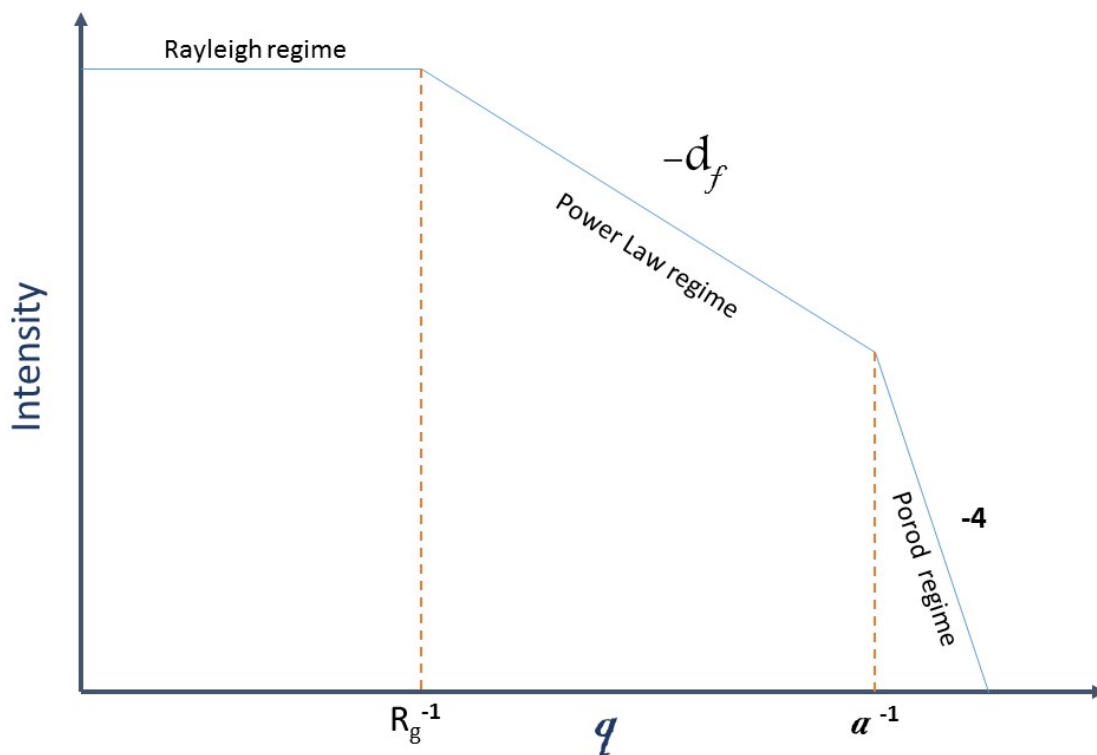


Figure 1.8: *The generic scheme for light scattering including the fractal dimension d_f for point particles (Rayleigh regime), spherical particles of radius of gyration R_g (Power law regime), and spherical particles under Porod regime.*

the influence of the Brownian motion [51]. This implies that the scatterers' distances in the solution are changing with time. In other words, scattered light by the surrounding particles establishes the interference phenomena (constructive and destructive).

DLS is a very popular technique because it is effective down to 1 nm of the diameter size of particles. Also, it can be applied effectively in different samples' environments, like, polymers, emulsions, micelles, or proteins.

How to use these two techniques (LSL and DLS) will be covered with necessary equations in the experiment chapter.

1.2.4 Historical Review of LS

SLS and DLS studies have been covered in depth, especially after the works of Kerker and Mie were published.

The first experiments in Dynamic Light Scattering were initiated by Prof. Leipertz at the Ruhr-University Bochum in 1989. The instrumentation was continuously improved since of that time. [52]

After the emergence of the laser in the late 1950' [53], it became the dominant source of light in the scattering experiments specially when dealing with small particles [54].

Mostly, when the term "light scattering" is mentioned, the source of light is laser. So, what does make a laser different from other light sources?. Lasers have unique characteristics that make it a perfect source for light scattering experiments [55]. First, laser is a monochromatic source^{§§}, so the wave length of the laser beam is mono-wavelength [56]. The second interesting characteristic of laser is that laser is a coherence light, and its divergence angle is very small compared to the other sources. This means that the laser has a small cross section when it impacts with objects [57,58]. From another angle, having coherent light gives more probability of light interference which means high contrast which is good for light scattering work. The third property of laser is the directionality, where laser is very directional light, i.e, ordinary light emits in all direction, but laser emits in one direction [59]. These three major properties make the laser the best tool in light scattering field.

Light scattering experiment setup is based on the general schematic shows in Fig.(1.9),

^{§§}In general ordinary light is not a monochromatic source.

where the source can be any kind of EM radiation^{¶¶}, while, the sample can be solid, liquid or gas. Moreover, the detector is the most effective and changeable factor in this kind of experiment.

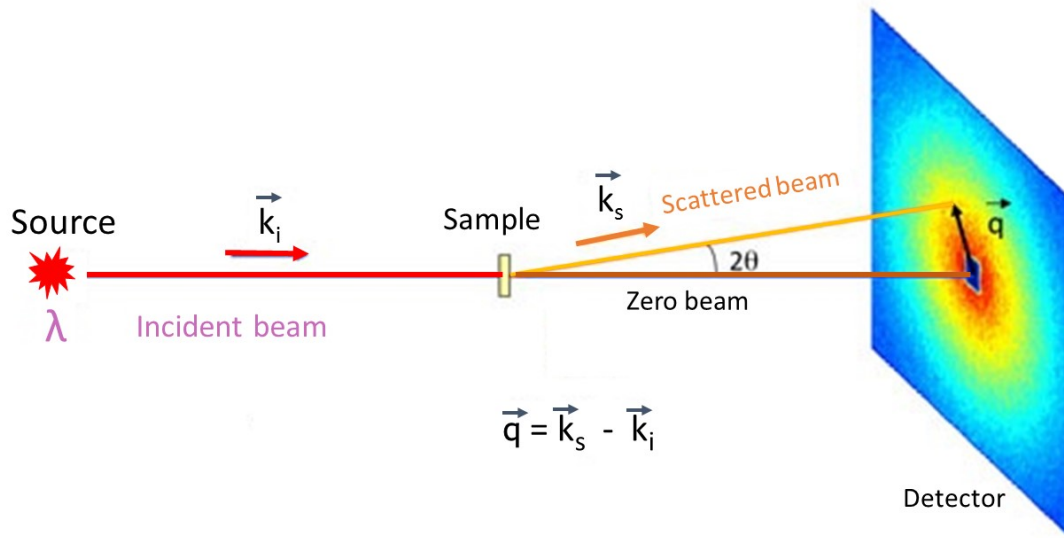


Figure 1.9: This figure represents the general light scattering experiment setup, where q represents the scattering wave vector and the detector can be any device, such as CCD camera or photomultiplier. [60]

Researchers have used different methods to deal with light scattering in matter. Most of the works based on Mie solution for a far-field approximation. So, there are many experimental setups which were established to study either light scattering phenomena or to study the applications of this phenomena. These different techniques are based on many parameters, such as the availability of equipment, the type of applications (biology, chemistry, ...), or ways of analyzing the data. All of technique depends on the intensity of the scattering waves (mostly visible light).

Using photomultiplier tube to capture the intensity was one of the popular technique. The photomultiplier **PMT** measuring the scattered light is mounted on a goniometer

^{¶¶}Mostly light.

which can be controlled from the angle θ that the scattered light is recorded, then the intensity of the scattered light is measured as a function of the scattering angle θ . See Fig.(1.10).

This is a typical application which can determine the average molecular weight M_W of materials such as proteins or polymers [61]. It can also measure the scattering intensity at different angles, which allows for calculation of the radius of gyration R_g , which also, measuring the scattering intensity for materials at different concentrations, which leads to finding the second virial coefficient A_2 .

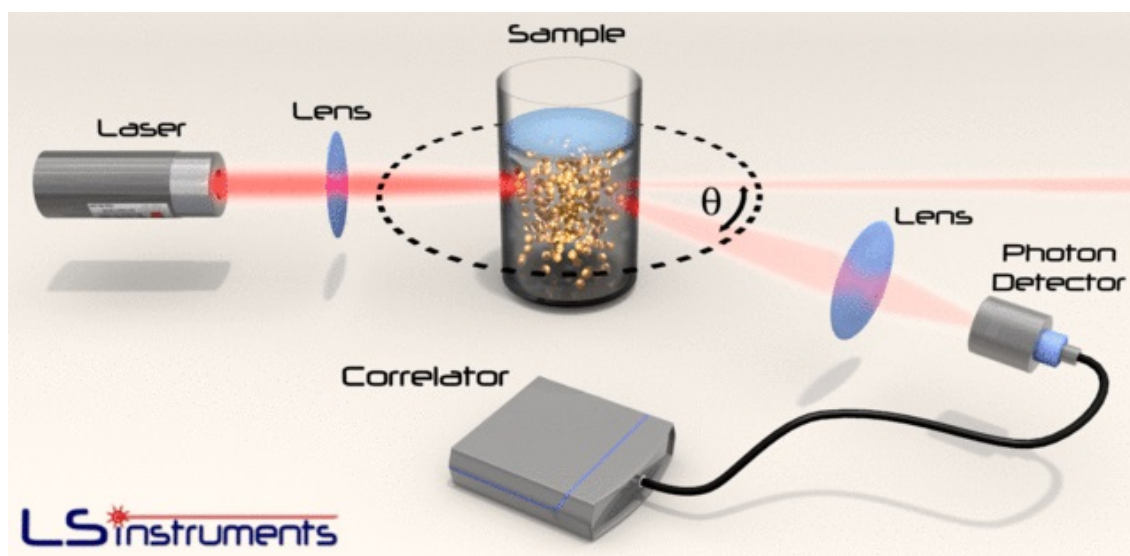


Figure 1.10: *PMT measuring the scattered light is mounted on a goniometer which makes it possible to control from what angle θ the scattered light is recorded. By measuring the intensity of the scattered light as a function of the scattering angle θ . [62]*

A more advanced technique, based on the previous one is by placing the photomultipliers on a portion of the circumference at a circle where the sample is placed in the center of this circle. See Fig.(1.11). In this setup the scattered rays are measured at the same time by each photomultiplier. The advantage of this technique is to have many angles at the same time, on the other hand, this technique needs an accurate

calibration among all photo-multipliers to let them talk to each other simultaneously because each of them has different photomultiplier quantum efficiency [63].

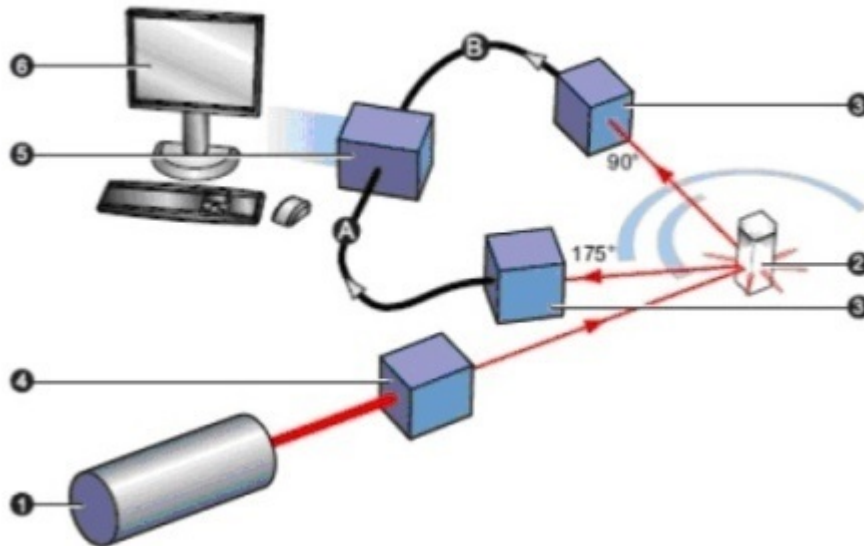


Figure 1.11: The general sketch of multi-Photo-multipliers where #1 indicates to the source of light, which laser in this figure, #2 indicates to the sample, while #3's indicate to the photo-multipliers devices, #4 is an attenuator, #5 is the correlator, and #6 is the computer. [64]

Another technique of light scattering is based on using a CCD chip instead of using photo multipliers. In this technique the CCD chip is exposed to the light that scattered by the sample itself. See Fig.(1.12). Most of the time, only a portion of image is captured for each run of experiment and this portion of image relies on the size of the CCD chip and on the pixels density of the CCD too. This CCD camera is usually connected to fast computers for the purpose of analysis, either for statical measurements or dynamics ones.

Most of light scattering experiments are base on these three techniques or a composition of them.

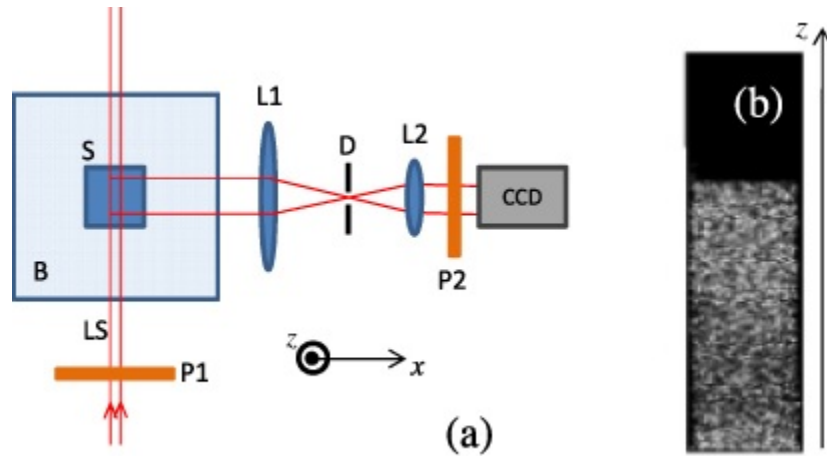


Figure 1.12: Panel (a) is a top view of light scattering experiment setup by using a CCD camera. Panel (b) represents the image of the sample. $L1$, and $L2$ are convex lenses, while $P1$ and $P2$ are crossed polarizers. [65]

1.2.5 Development and Application of an Area Recorded Generalization Optical Scattering Technique

This technique which is abbreviated as **ARGOS**, is a new technique which is developed in Order-Disorder Laboratory of WPI. This technique was based on two factors. First one is that the detector has been chosen to be a flat semi translucent screen. This screen was illuminated by the scattered light to form speckles. The second factor for this experimental setup is the beam filter, which is made of multiple layers of neutral filters ND. See Fig.(1.13). This filter has played an important effective factor during the experiment, where by using this beam filter it was possible to measure different data for different analysis.

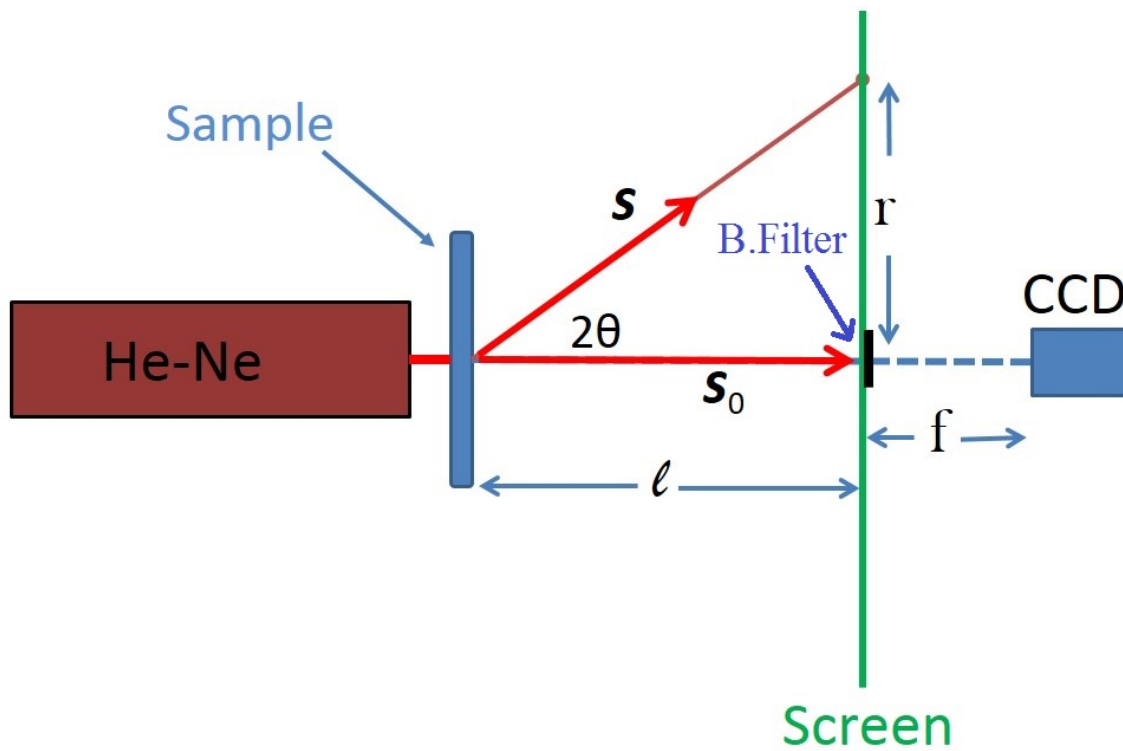


Figure 1.13: ARGOS technique, where it can be seen the Beam Filter while the screen works as a detector. Also, behind this screen, there is a CCD camera to take shoots to the screen.

Chapter 2

Methodology

2.1 Hardware and Software

2.1.1 Devices and Tools

2.1.1.1 LASER

A laser was the source of light which was used in this work, see Fig.(2.1) [66]. This laser is the JDSU He-Ne laser purchased from **Edmund Optics** Model(1125), 5 mW at 632.8 nm, with random polarization. This laser stabilizes after 10 minutes of operation as mentioned by the manufacturer's work-



Figure 2.1: *The He-Ne laser which was chosen to be used in this work, this laser has a non polarized laser, so it was possible to chose whether unpolarized source or a polarized one by using a polarizer.*

sheets.

2.1.1.2 CCD Monochrome USB Camera

The CCD camera which was used in this work, see Fig.(2.2) [67], was purchased from **Edmund Optics** model (EO-0813M 1/3). This camera is an 8 bit monochromatic CCD, which gives a resolution of (1024 x 670 pixels), and shutter speed of 1/30 sec. The type of camera's sensor was from Sony[®] with a pixel size of 4.65 x 4.65 μm .

2.1.1.3 Fixed Focal Length Lens

These lenses were purchased from **Edmund Optics** Fig.(2.3), which is a 16 mm focal length, C-Mount, and working distance is 100 mm to ∞ .



Figure 2.2: *The MONO camera CCD whic was used in this work, was the model EO-0813M , which was used to take photos snaps during this work.*



Figure 2.3: *The 16 mm focal lens*
The 16 mm fixed lens which was used to focuses the images on the CCD camera was purchased from Edmund Optics, and this lens model is 16MM EO MEGAPIXEL FIXED FL.

2.1.1.4 Anti-vibration Table

During this work a RS4000 Series tuned damped top performance optical table made by the Newport Corporation, which was boosted over four damping cylinders as shown in Fig.(2.4). This table model RS4000 Series, can damp most of vibrations around the table that can be caused by any vibrations in the lab or in the other labs around.

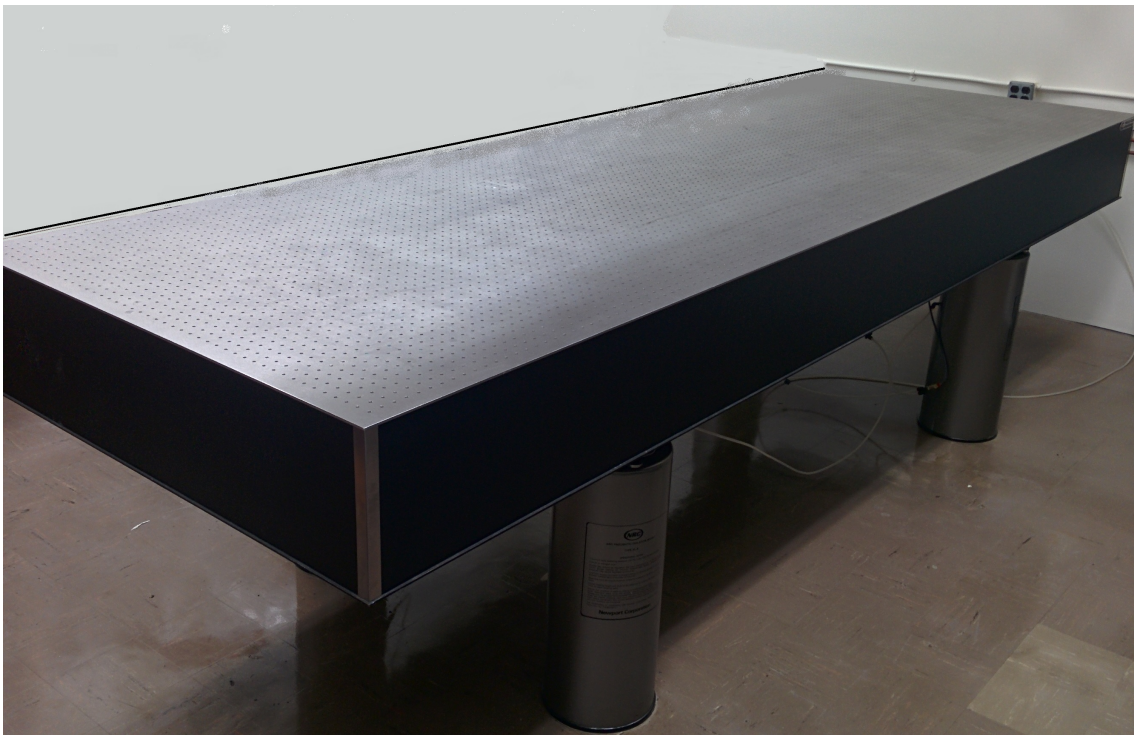


Figure 2.4: *This table is tuned damped top performance optical tables made by Newport Corporation.*

2.1.1.5 Screen and Beam Attenuator

- **Screen** During this work, different types and different sizes of screens were used, a 250 x 250 mm, model 220 **Grit Ground Glass Diffuser** from Edmund

Optics Inc. A letter size **translucent vellum**, shown in Fig.(2.5) from WORLDWIN[®], model (WGP0098U).

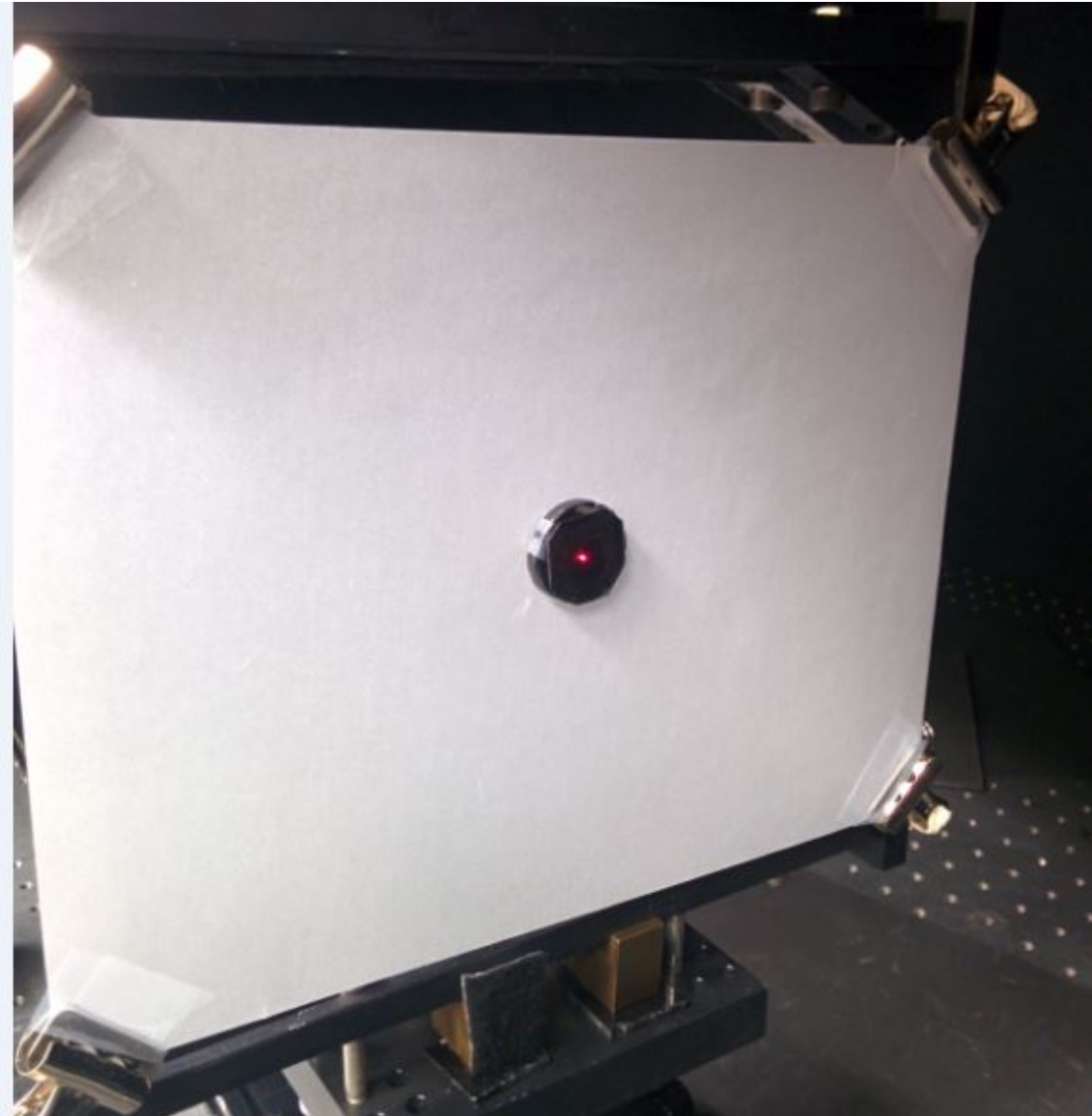


Figure 2.5: *Semi translucent paper screen. The Multi-Layers beam attenuator attached into the middle of the screen*

- **Beam Attenuator**

This beam attenuator filter has played an important role in this work. The filter acted as a beam center indicator, where it was designed to allow the zero-beam ray to go through it, which also blocking the rest of the unwanted portion of the beam that came around the zero-beam. This portion of the beam is responsible for the high distortion in scattering experiments. Also the amount of intensity which was allowed through this beam was not high enough to saturate the CCD. So this beam attenuator was able to determine the zero-beam's exact position, which was a requirement for the analysis process. The other purpose of this beam attenuator was to use the beam which was allowed to pass through as a reference beam to detect any changes in the laser fluctuation during the experiment. In this way, the changing of the speckle intensity during the run of the experiment could be determined to be from either the dynamic sample or as being related to the changes of the background.

The beam attenuator was made of multiple layers of ND filters. See Fig.(2.6). The number of the layers were chosen based on the strength of the central beam's intensity that was heading the beam attenuator, please check Appendix (B.1) for more photos and for more details.

The different filter sizes in diameter were used for the different distances of the sample from the screen; e.g., in case of close distance and low scattered intensity, the smaller filter is better and vice versa.

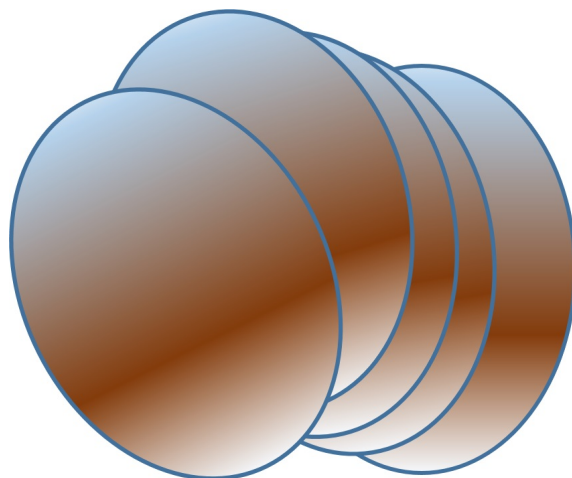


Figure 2.6: *Multi-layers Beam Attenuator*

2.1.1.6 Sample Holder

Two plates of aluminum were machined to hold two halves of microscope slides. Between these two slides the solution (the specimen) was spread, while the thickness of the sample width was controlled by placing a spacer made of Teflon PFA film (DU Pont, Wilmington , DE, USA) as shown in Fig.(2.7). For the actual photo of this holder, check Appendix (B.3).

2.1.1.7 Slides Wafer

This wafer was made from a chunk of Teflon material for cleaning purposes, as it will be shown in the cleaning section. The microscope slides were cleaned in an aggressive acid during this process. So, the Teflon was the best choice for its resistance to acids as well as its great resistance to high temperature. This may correlate with the cleaning process.

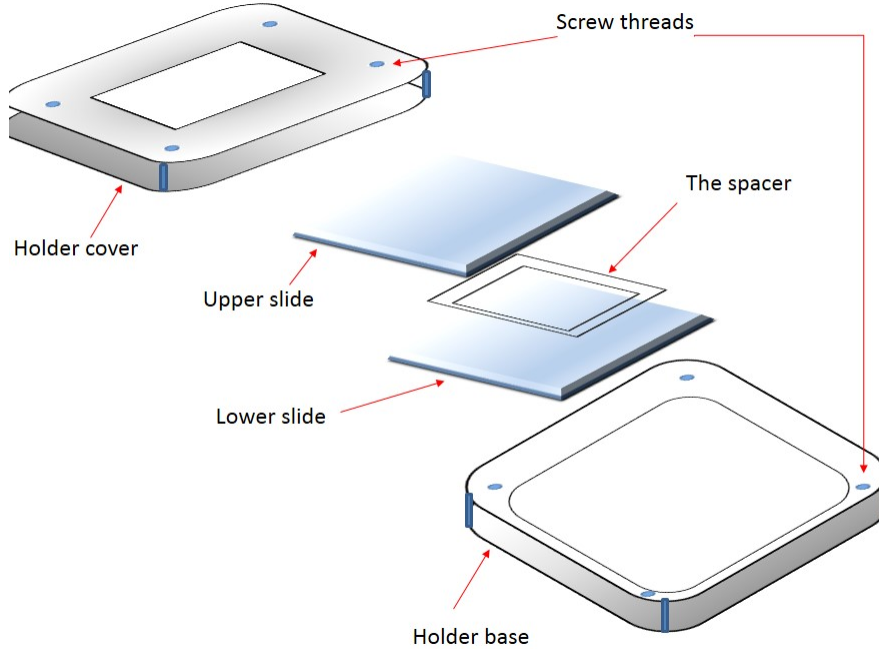


Figure 2.7: *The specimen holder*

This wafer was built in the physics workshop in a circular shape* of diameter 11.5 cm , and thickness of 1.5 cm. Slits were cut along the surface of the wafer that were 2 mm in depth and 1.5 mm width, where the slits were tilted by 30°. Also, holes of 4 mm diameter were drilled through the wafer from the top to bottom over the slits to create good circulation for the cleaning solution in the Pyrex sink. Also, bigger slits of 10 mm wide and 5 mm deep were made along the bottom of the wafer to also create good circulation. Moreover, this wafer was supplied with a long hand of the same material to handle the wafer easily through the cleaning process. Please, look at Fig.(2.8). For extra photos, see Appendix (B.2).

*Circular shape, because it was easy for machining.

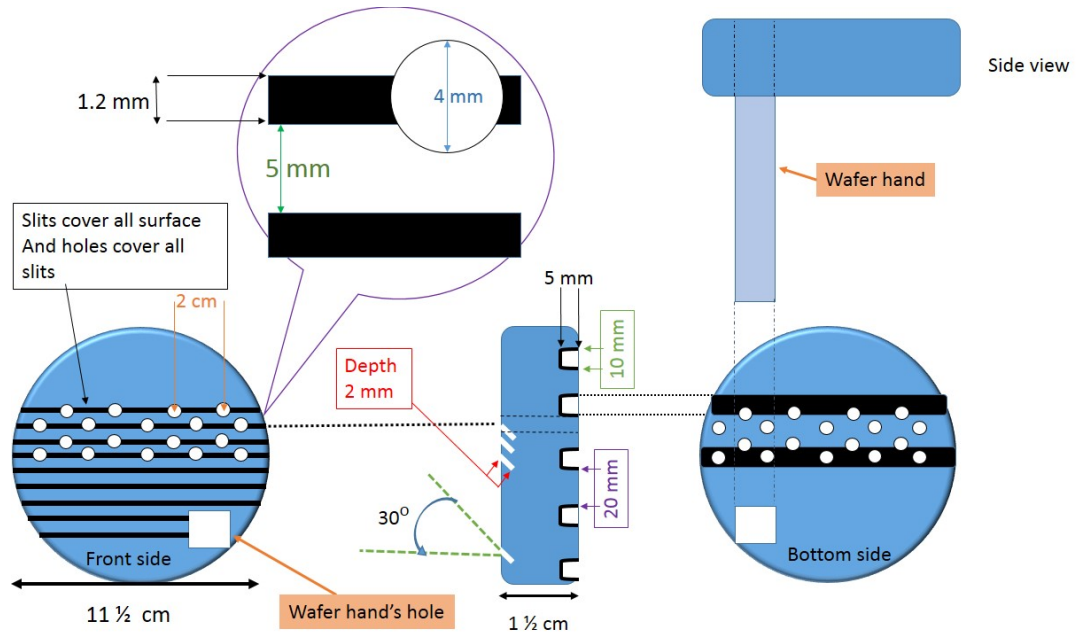


Figure 2.8: This is a photo of the Slides Wafer, made of Teflon chunk in a circular shape, of $11\frac{1}{2}$ cm diameter and $1\frac{1}{2}$ cm thick.

2.1.2 Sample Materials

- Water

Three grades of water were used in this work based on these purities:

- (i) **Grade C**, distilled water from the chemistry building at WPI, which has a resistivity of $14 \text{ M}\Omega$. This grade of water was used for the pre-cleaning process for the microscope slides before starting the main cleaning process which will be discussed in the next section. Also, this grade of water was used to rinse the slides after the main cleaning process which used chemical process.
- (ii) **Grade B**, high highly purified distilled water which was supplied from

professor Stroe's lab[†] of resistivity 18 M Ω . This water was used to do the last rinse of the slides under the laminar hood. Also this water was used to clean the tubes before they can be used to contain the mixture of water and the scatterers.

- (iii) **Grade A**, water LC-MS CHROMASOLV[®] from SIGMA-ALDRICH. This water is very high pure water which was filtered through 0.2 μ m and it was used as a solvent for the samples.

- **Spheres**

Variety of FluoSpheres[®] Size Kit#1, Carboxylate-modified Microspheres, red fluorescent(580/605), 2% solids of sizes (2, 1, 0.5 , 0.2, and 0.1 μ m). This kit was purchased from **life technology** with code number (F8887).

- **Microscope slides**

CORNING[®], microscope slides model(2947-75x25) Pre-Cleaned 75 x 25 mm of thickness 0.96 to 1.06 mm were purchased from **Corning Incorporated**.

- **Spacer**

During this work a Teflon PFA film of 100 μ m thickness from **DuPont** company was used to be a spacer between the two microscope slides which hold the specimen.

- **Acid**

Sulfuric Acid Suprapur[™] ACS 96% 0.3(49g/L, H_2O) H_2SO_4 F.W.: 98.8g/cm³

[†]Stroe, Izabela, Assistance Professor, physics, WPI, Worcester, MA, USA.

from **EMD Millipore**.

2.1.3 Software

Programming and all codes that were used through this work are based on Lab-View 2009 64bit, Assistance Vision program (AVP) version(9). Below is a lists of codes(programs), where each program was built for a specific purpose.

2.1.3.1 Laser Interaction with Particle Volume Program

This code, which is abbreviated as **LPV** was built in order to show the correlation in between the concentrations and different sizes of particles, check Fig.(2.9). For example, if 10 particles of size $2\mu\text{m}$ were dispersed in a solvent of 1 ml of water, this correlation would be used to determine the concentration of $1\mu\text{m}$ of particles in the same amount of solvent. This is based upon the concept of what is referred to as the foot-print cross section, which states that the total area of the surface of the particles that faces the cross section of the laser beam is the same for different sizes.

For example, if a $2\mu\text{m}$ particle facing a laser beam, 4 particles of $1\mu\text{m}$ size are needed to cover the same area of laser, based on the simple mathematic equation $n_s = R_L^2/R_s^2$, where n_s is the number of small particles of radius R_s and R_L is the radius of the large particle.

This code also gives the concentration of particle in the normal way, i.e, n/V where n is the number of particles and V is the volume in ml as shown in the field labeled

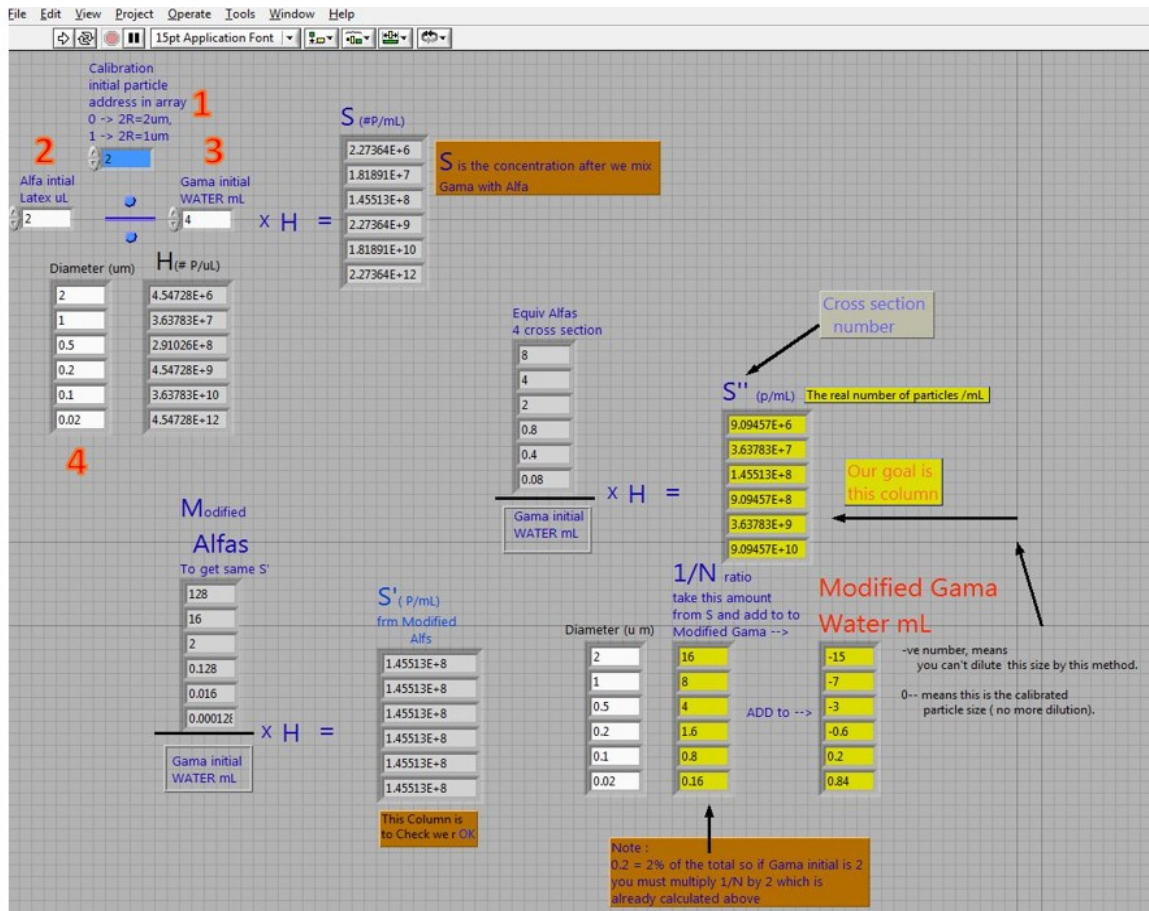


Figure 2.9: The front panel of the LPV program, where the keys(fields) which are indicated by numbers from 1 to 5 are the fields need to be chosen.

with S, look at the interface of this program in Fig.(2.9).

This tool was programmed to calculate the concentration of each sample in the unit of [Particle numbers] per [volume] "p/mL". This tool also, calculates the "LPV" which is shown in table (2.1). Where LPV is a method to find the correlation between particle concentration and the sizes of particles look at Appendix (A.1) for the code of this program.

Table 2.1: *Dummy table which shows the information that were supplied to "Taking Photos Program" as it will be seen next.*

Date	12-12-2013
Time	5:24 PM
Purpose of measurement	This experiment run is set to measure
Particle type	Latex
Particle shape	Sphere
Particle diameter	2 μm
# of particles / mL	...
# of particles / LPV	...
Sample preparation	bla bla bla ..
Screen distance	...
Screen resolution	...
.....
Note:

2.1.3.2 Taking Photos Program

This program which is referred as **TPP** was built to control the CCD camera, to allow for photo capturing and for the experiment's parameters to be held at the same time Fig.(2.10). This includes sample's information (concentration, the sample holder, the particle size, etc.) as well as the date and time of the experiment, the number of photos, time intervals, sample preparing method, screen distance, the camera distance, and other notes that may have needed to be included. See table (2.1) for the dummy model. **All of this data was supplied to the program before any photos were taken.** See Appendix (A.2) for the interference of the TPP program and for the program's code.

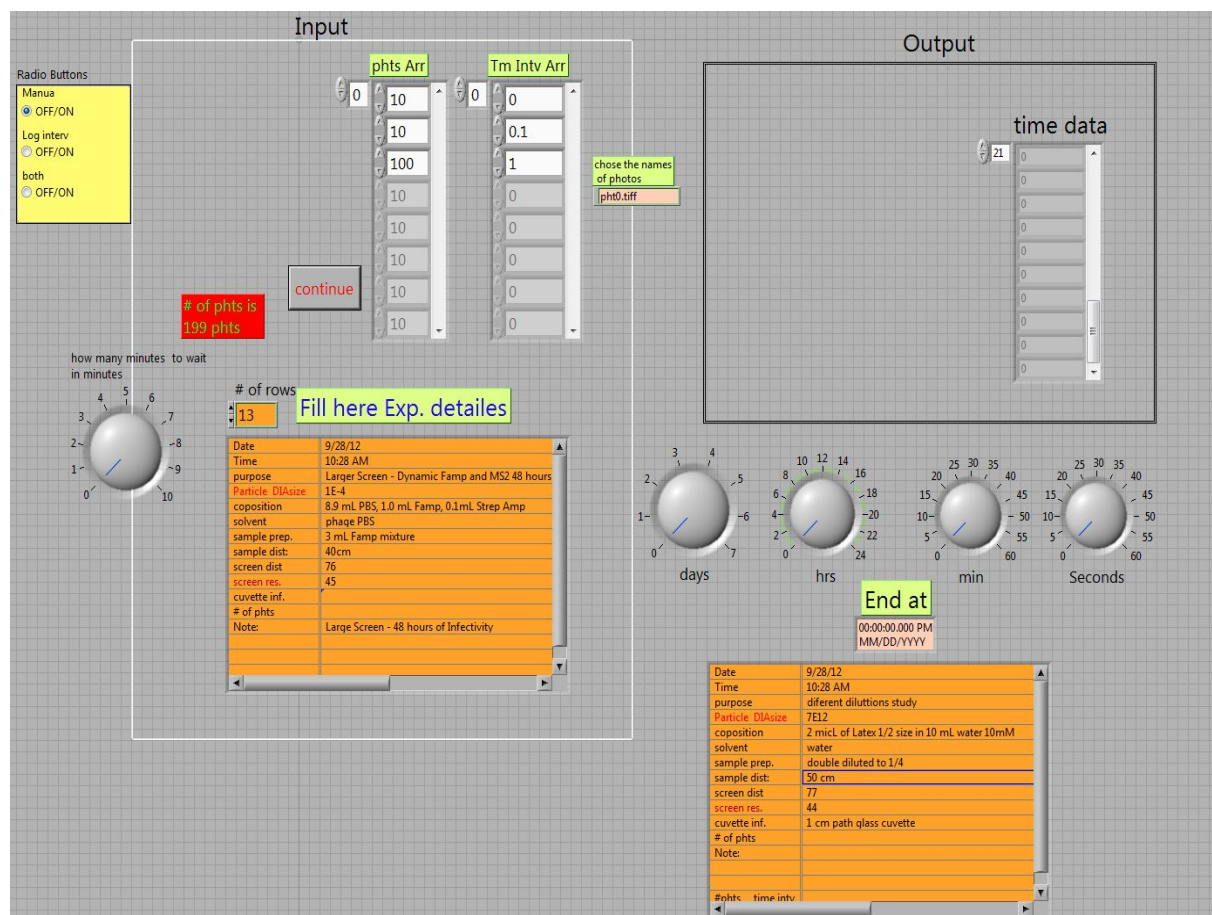


Figure 2.10: The interface of the TPP program. It can be seen that the two columns in the input section, where the first column represents the number of images, while the second column represents the intervals between the images. Zero in the second column means the camera operates with its fastest speed.

2.1.3.3 Total Photo Average Program

The concept of the Total Photo Average Program **TPA** is to extract the intensity of each pixel, then calculate the average intensity for each image. The front panel is shown in Fig.(2.11).

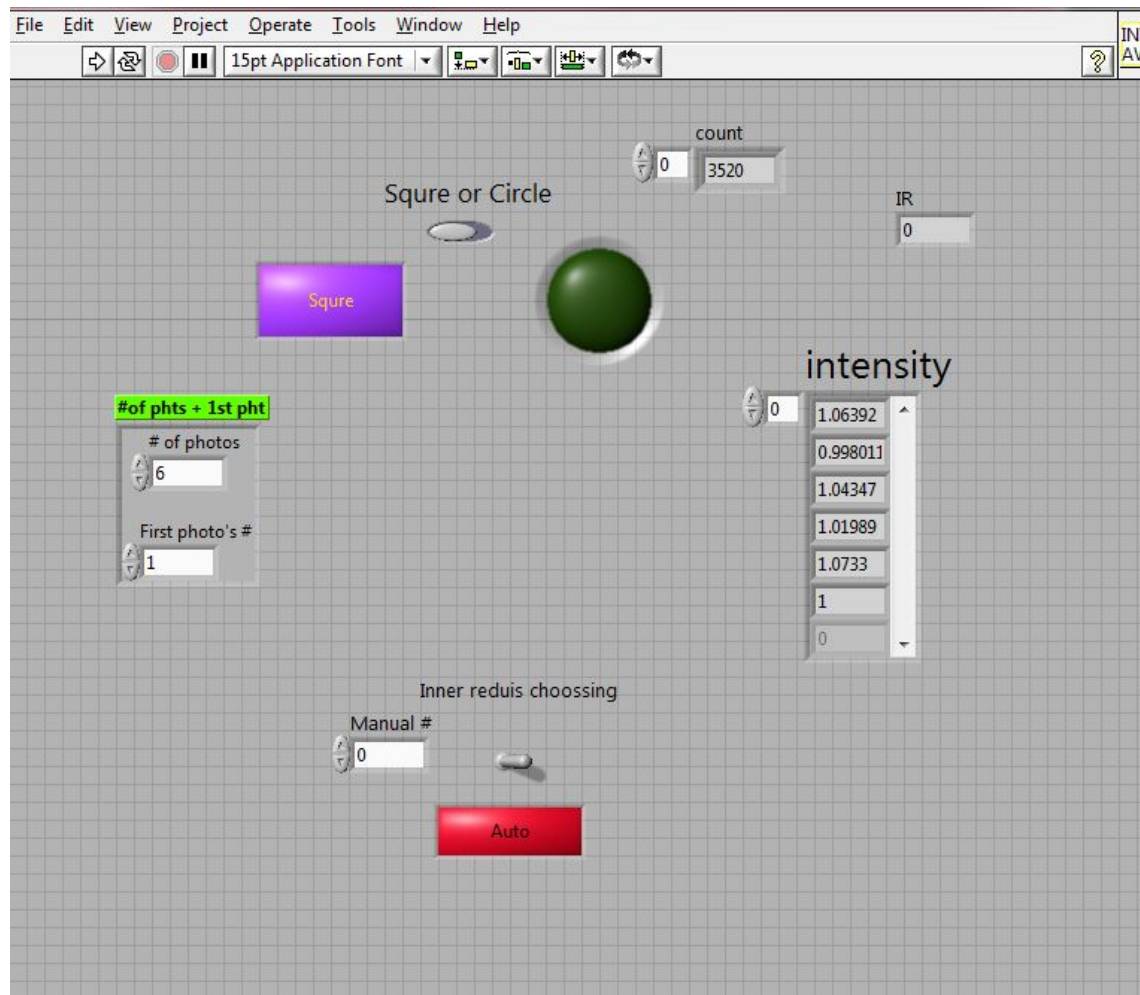


Figure 2.11: The panel of the TPA program, where in this cod the number of required analysis photos can be decided, also the mode of analysis either circle mode or squire mode can be chosen. Also, in circle mode, the radius of the circle can be determined precisely.

2.1.3.4 Main Analysis Program

This program which is abbreviated as **MAP** was made to do the main analysis of the images by extracting the intensity[‡] of each pixel. The TPA then correlates this intensity with its position on the image which is represented as q-vector. In Chapter (2) there are details about using this program for data analysis.

[‡]In fact, it is not the usual intensity in Optics, but it is the shade level number (0-255 in case of an 8-bit CCD).

2.2 Cell and Sample Procedure

Since light scattering is very sensitive to many parameters (dust, humidity, temperature, etc...), some procedures and environmental controls have been implemented into this work. For example, a laminar hood was used for storing the samples as well as storing the tools that were used to prepare the samples. Also, using special clean particles-free gloves, masks and sterile pipette tips was essential in this work.

2.2.1 Slides Cleaning Process

The microscope slides were cleaned prior to their usage to contain the samples. Since the Corning company product was used in this work, it was preferable to use the company's technique for cleaning the slides, as follows:

• **Procedure:**

1. Clean the slides, the wafer Fig.(2.8), and the dishes using tap water and Alconox[®] detergent powder.
2. Rinse the slides and the dishes with tap water and then with grade **C** distilled water.
3. Place the slides' wafer holder in the bottom of the dish. Then place the slides in the grooves of the wafer vertically as shown in Fig.(2.12)
4. Fill the dish until it covers all of the slides with the acetic acid and leave them for ten minutes (under fume hood).

5. Discharge the acid into a safe container and close it tightly. Then keep it in a safe place.
6. Rinse the samples with grade **C** water several times until the ph tester shows there is no more acid in the dish.
7. Discharge water from the dish. Then rinse the slides with grade **B** water.
8. Discharge all water from the dish, then fill it with grade **B** water until all of the slides are covered with water.
9. Cover all sets (the dish and the slides) with another clean dish and then transfer the set to the laminar hood.
10. Place the group on the laminar's desk and ensure that nothing lies between the laminar hood's air mesh flow (LAMF) and the set.
11. Remove the upper dish and place it out of the laminar, and then discharge the water.
12. Boost wafer up over some supports to expose the slides to the air flow of the LAMF. Keep them overnight to be dried. See Fig.(2.12)



Figure 2.12: *The slides placed in the groves next to each other on the wafer. The wafer was boosted over three supporters inside a square glass plate to give a good ventilation for the slides.*

2.2.2 Sample Preparation

This part of section will talk about two stages for preparing the sample. The first one will be about how to prepare the mixture of the solution, and the second one will be about how to make the film between two slides sandwich.

- **Solution Preparation**

1. Different sizes of vials containers were used to prepare the solutions (3.5 mL and 6 mL). These vials needed to be cleaned carefully with a pure distilled water and methanol inside an ultra sonic sink under the fume hood for an hour or so.
2. These vials should be transferred in a closed box to the laminar hood.
3. The last stage for vials' cleaning is to flash these tubes with a high purity water and to be left to dry under the laminar hood before they can be used to contain my sample's mixture.
4. A half of the solvent was taken to the container vial by using a sterile pipette tip .
5. A required amount of latex solution was taken to the vial by using an accurate sterile pipette tip (2-4 μL) .
6. The second half amount of solvent was added to the vial.[§]
7. After the previous steps, the vial was sealed carefully then It was taken back to the ultra sonic sink and mixed for 5 to 8 minutes.
8. After the mixing process cycle is completed, the vial was removed from the sink, then it was dried with a clean tissue and kept wrapped with the tissue until it reached the laminar hood for the last process of making the sample.

[§]It is preferable to add the solvent in two halves before and after adding the latex solution to prevent the latex from sticking to the vials' walls

- **Film Preparation**

Before talking in detailed about the steps that should be followed to prepare the film sandwich, it may might be useful to mention about some caution during these process.

First, wearing particles-free gloves (sterile gloves at least) and putting on mask(recommended) is very important during this process. **Second**, ensure that your hands were at the farthest point from the laminar hood's air mesh flow (LAMF), so the materials that you are going to deal with will be between the air mesh and your hands,i.e , the air flows from the air mesh passing by the materials toward your hands leaving the laminar hood desk.

All material or tools (high pure distilled water, tweezers, optics bump, ..etc) that may have been needed for use under the laminar hood should be cleaned and stored on the laminar hood's desk.

Now lets talk about the process steps:

1. After you follow the steps in stage one. The sample tube and the sample holder Fig.(2.7), were taken with the other stuff that may have been needed and they were put on a pre-cleaned table next to the laminar hood.
2. The free particles (sterile) gloves and the mask were put on before going to the next step.
3. The sample tube was carefully placed on the laminar hood's desk while hands should be always at the farthest point away from the LAMF.

4. A pre-cleaned microscope slide were taken from the rack, see section (2.2.1) and it was placed on the lower part of the sample holder.[¶]
5. A spacer of 100 μm was placed carefully over the micro scope slide.
6. A small amount of grease was drawn as a circle (around 0.7 mm in diameter) with a special pen over the bottom slide to prevent the solution drops from escaping while placing the cover slide in the next steps.
7. By using pipette, a small amount of sample's solution (about 7 μL) was spread gently inside the grease circle.^{||}
8. An other pre-cleaned slide was brought from the slides rack and it was placed carefully and slowly over the composition solution until it overlapped it completely.
9. The upper part of the sample holder was placed to cover the group, then it was pressed firmly from all sides and then the screws were tighten up in their positions.
10. A punched hole mask were placed in the window of the upper cover of the holder. See Fig.(2.7).
11. The sample was taken after that to the microscope to be checked before it can be used.

[¶]It preferable to blow up the dust from the surface of the slide with an optics pump before applying the solution to the surface of the slide.

^{||}When placing the solution over the slide, it is important not to lift the pipette tip from the surface of the slide until all necessarily amount of solution is completely injected, this will avoid building air bubbles.

2.3 Experiment Set Up

Experiment Configuration Tips

One of the advantage of this technique that was established in this work is that this system is an open architecture Fig.(2.13), so plenty of space was available to install equipment here or there on the table when ever was needed for any purpose that might show. On the other hand, there are some constraints (laser coherence length, size of the table beam profile distortion , ...,etc.), so it is recommended to take these precautions before starting the measurements:

- ▷ **Laser is dangerous.** Even He-Ne lasers are mostly low power lasers, but they are still able to damage eyes, so looking directly to the beam and always use a piece of paper (darker is better) to find the beam or to study the beam's profile.

- ▷ **Enough room.** It is always recommended to leave some spaces between laser and the sample for additional equipment (pin-holes, semi-translucent, mirror, ..., etc.) that might be needed in future, so that there is no need to take the experiment apart to install some extra equipment.

- ▷ **Dealing with optics.** Touching optics equipment with bare hands is not a good idea at all. It is necessary to use gloves or tissues at least.

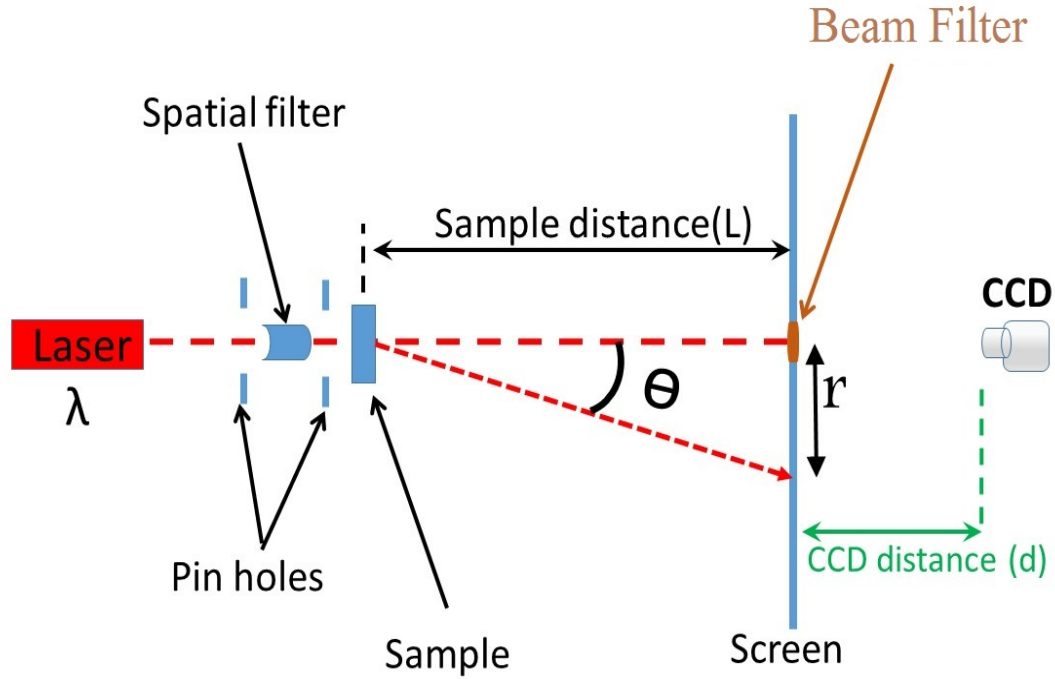


Figure 2.13: Configuration of the experiment that was mostly used during this work. He-Ne laser was the source of the light, the laser beam goes through two pinholes for filtering where between these two filters a spatial filter was placed. The sample holder was placed after the second filter. The scattered beams were received on a flat screen at a distance L , and behind this screen the CCD camera was placed at a distance d .

2.3.1 Configuration

As was mentioned in Section (2.1.1) an anti vibration table was used to embrace the experiment. Also the table was covered with a heavy black clothes to block the background light from interfering with the laser beam, then the following steps were followed to build the experiment setup as shown in Fig.(2.14).



Figure 2.14: *Experiment configuration's photo. The anti-vibration table is boosted over four air cylinders to keep the table vibrationally isolated. Also it can be seen how the equipment stand in the order as described in the text.*

2.3.1.1 Laser Alignment

In this work a long rail was used along the width of the table and all equipment was mounted over this rail to keep the set in an alignment during the changes. Before starting any measurements, the alignment of the laser with the equipment was always checked. The first step was to align the laser by using this method of three-points:

1. First, The laser was placed on a rigid 3D post holder on the first end of the rail then it was fixed there, also rigid rods were attached to the table around the laser to protect it from accidental touches.
2. Two identical pinholes were placed next to each other by the laser beam output, then the closer one was tied to the rail.
3. The laser was turned on and both of the pin holes were aligned to the laser beam.
4. The second pinhole was moved away from the other one and from the laser and then it was placed to the end of the rail (the second end of the table).
5. In this stage, you will notice (mostly) that the laser does not pass through the farthest pinhole, so the laser level had to be adjusted to make the laser beam passes through the two pinholes at the same time.
6. Last stage, the loose pinhole was moved back and forth many times before getting the laser aligned perfectly.

2.3.1.2 Optical Elements Arrangement

1. The equipment was placed on the rail in this order, check Fig.(2.7):
 - (a) **The laser** was boosted on the edge of the rail by using a rigid 3D holder.
 - (b) **A Partial Filter** was used to filter the laser beam to get a uniform gaussian beam.

- (c) **Plano Convex Lens** was used to take back the beam cross section profile to its original diameter.
- (d) **Variable-Iris Pinhole** was placed next to the specimen holder to prevent any background light from hitting the sample. Also it does more filtering to the laser beam before it reach the sample.
- (e) **Sample holder** was placed next the pinhole.
- (f) **Background Isolator** which was made of a 30×30 cm black mat material with a specific square window in the middle (suitable to the sample's size). This blocker keeps the required scattered light from the sample isolated from the laser source and the other possible reflections before this scattered light reaches the screen.
- (g) **The screen** was placed between the background blocker and the CCD cam and. This screen can be slid freely on the trail forth and back along the table.
- (h) **CCD camera** was placed behind the screen and attached to the screen at a specific distance, so that it could slide with the screen freely along the trail.
- (i) **Black Cloth** was made of a double layer cloth works as a tent to isolate the equipment from the background sources.

2.3.2 Calibration

Since the scattering experiment is very sensitive to any minor changes which could happen to the scattered light, and also to any fluctuation in the laser itself or the sensitivity of the CCD camera, some calibrations for these factors were made as follows:

2.3.2.1 Laser Stability

Because most CW lasers needs a time interval after operating to reach their stability condition, when the fluctuation in the intensity reaches the minimum, the following steps were followed to calibrate the laser.

1. The laser was placed at the edge of the rail on the table.
2. A spatial filter was placed on the path of laser, so an expanded homogeneous beam emerged.
3. A variable ND filter was placed next to the spatial filter to minimize the intensity of the beam, where avoiding CCD camera saturation is an essential.
4. In the path of the beam an Opel diffusing glass was placed to get a diffused spot.
5. A CCD was placed behind the Opel diffuser, then the camera was moved as close as possible toward the diffuser to capture most of diffused spot on the Opel diffuser without losing the focus of the camera, then all device were covered up.

6. *Taking-Photos Program (TPP)* , The aim of this program is to take photos of the screen for specific numbers and specific time intervals between images as shown in Fig.(2.10). For the details of the codes see Appendix (A.2). TPP program was started then one photo was taken to represent the zero time's photo.
7. The laser was turned on, then the TPP program started taking photos in the sequence of " one photo every ten seconds" for 30 minuets.
8. The average intensity for each image was calculated , then each value was placed next to the relevant time.
9. A plot of these values is shown in Fig.(2.15)

From this plot in Fig.(2.15), it can be noticed that the laser is quite stable after 10 minutes, and this was the minimum time that was chosen during this work. Moreover, this time (10 minutes) is the recommended time as it is declared in the company's web site.

2.3.2.2 Dust Influence

Dust is around us everywhere. As a result, it is impossible but its effect can be minimized, and that what was done through this simple calibration to monitor the negative impact of the dust.

Here the equipment was covered with the cloth, then lab lights were turned off , then the screen directly exposed to the laser beam, where the beam hit a dark mat beam attenuator witch is located in the center of the screen, then the camera software was

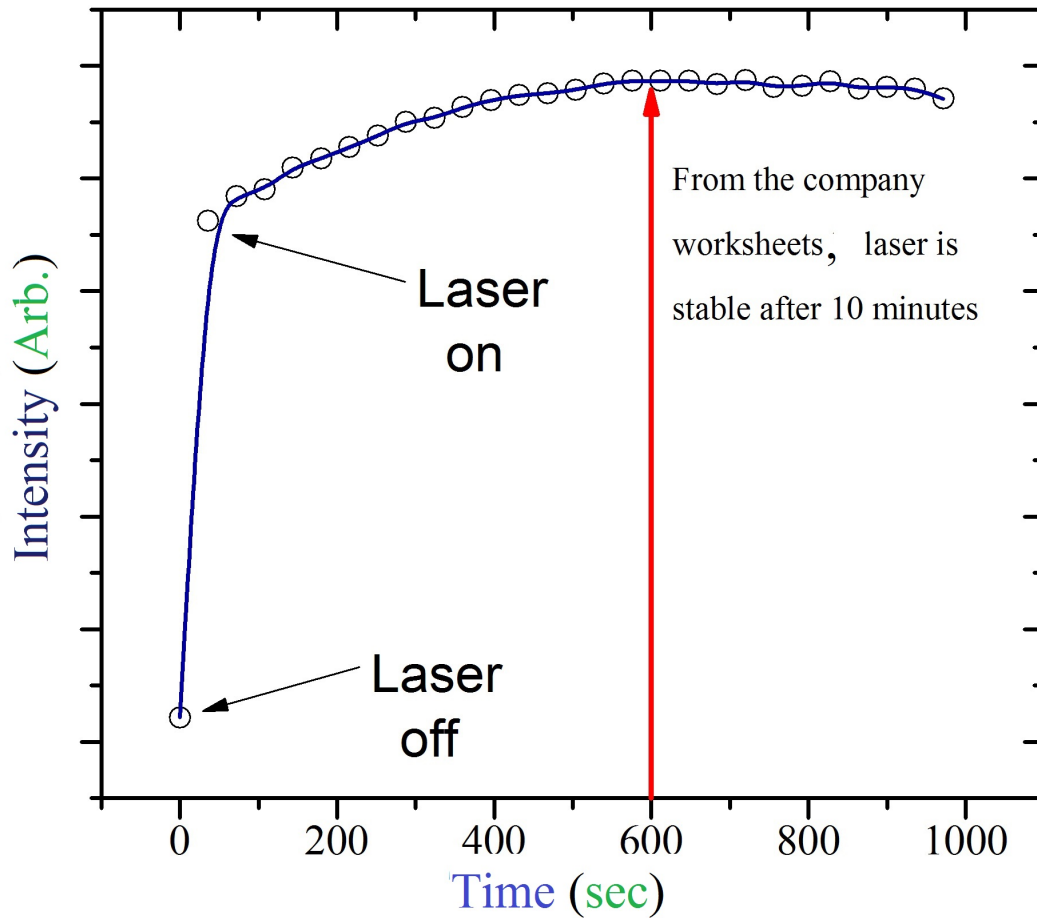


Figure 2.15: *This is the laser stability versus time plot. As it can be seen in this plot that the stability of the laser happened after 10 minutes which agrees with the laser specifications as supplied by Edmund Optics Inc.*

started on the computer while monitoring the monitor.

While the beam attenuator should have prevented the laser beam from hidden the cam, some flares were observed at the beginning of observation, which was caused by the dust. Fortunately, with progress of time, these flares gradually faded, until they disappeared after 10 minutes.

So, for this experiment configuration, ten minutes was the requirement time to avoid the effect of dust scattering during the experiments run.

2.3.2.3 CCD Pixels Defects

Two stages of calibration were made. The darkness and the brightness calibrations.

1. In the *darkness calibration* the experiment was covered by the cloth, then the camera's cap was removed while all lights are off. After that the cam was on then a one photo was taken , then this photo was analyzed to check the intensity of each pixel individually.
2. In the second stage of this calibration which is *brightness calibration*, these steps were applied in series:
 - (a) A tungsten lamp was placed at the the edge of the rail.
 - (b) The screen and the camera were moved to the other end of the rail so more parallel light would come from the lamp, which caused a uniform illumination on the screen with the maximum bright (100 Watt bulb).
 - (c) The next step was taking the CCD's cap, then one photo was taken.
 - (d) The last step was analyzing the photo to check the intensity of each pixel.

From stage (1) and stage (2) It was found that the dead pixels were very rare, almost 4 pixels out of $\sim 800,000$ pixels the resolution of the used CCD in this work.

2.3.2.4 CCD Linearity

As it was mentioned in the materials' section, check section (2.1.1), an 8 bit CCD camera was used, so the range of this camera should be from 0 to 255, where zero indicates no light at all, and 255 means the maximum intensity that can be distinguished by this camera. So from the theoretical aspect, when taking photos gradually from darkness to the maximum brightness, and after these photos were analyzed by calculating the average intensity of each photo, a straight line was expected to start at (0,0) and ends at 255 on Y-coordinate, where the X-axis represents the power which was measured by the PM, while the Y-axis represents intensity in scale from 0-255 as seen by the CCD.

Considering now the practical part. The following setting and procedures were established to study the behavior of the camera .

- **Setting and Measurements**

1. The camera(CCD) was placed at the end to the rail.
2. The power meter(PM) head was placed underneath of the CCD where it could captured the same power as the CCD did.
3. The CCD and the PM head were placed to be as close as possible to the screen so the screen could cover the whole angle of the CCD.**.
4. At the end of the rail, a tungsten lamp (100 watt as an example) was placed and it was attached to a Coil-rotation transformer which varied the voltage on the lamp to get different intensities.

**Be careful not to be out of the camera's focus

5. After that, the devices were covered with the black cloth then all lights were turned off.
6. The next step was turning the CCD , at the same time the lamp switch was in the off position.
7. After everything was settled as mentioned above, the Assistance Vision program (AVP). See Section (2.1.3) was started, then the histogram tool was activated to be sure that it was reading the minimum intensity on the scale from 0-255.
8. Turn on the the PM.^{††}
9. The next step was finding the maximum point. First, the lamp was turned on. Secondly, the current was increasing gradually until the highest intensity on the histogram tool was detected, which indicated to the maximum.
10. The reading from the PM in the previous step which was related to the highest intensity on the histogram, was printed on a piece of paper.
11. After that, the lamp was turned off, and the first photo was taken at the same time the reading showed on the PM was recorded.
12. Photo number two was taken by turning the lamp on, at the same time the lamp luminance was increased by the transformer's knob until some digital was read on the PM monitor.

^{††}It is not necessarily to get zero reading on the screen.

13. The previous step was kept repeated for different luminescences until the maximum point was reached, check step (9) above.

- **Analyzing Photos**

In this analysis the TPA program, check page (47) , was used to analyze this part of work as follow:

The average intensity for each photo was listed with its relevant power which was measured by the PM, then the average intensity (which is nothing but the shade level 0-255 of the 8-bit CCD) versus the power measured by the power mater was plotted in Fig.(2.16).

- **Discussion and Correction**

As it can be seen in Fig.(2.19), the CCD camera is not linear at low and high range, i.e. the CCD is not a sensitive enough to distinguish between intensities near it's lower and higher limits. On the other hand CCD did a good job in the middle range (between 3 and 220 bit value).

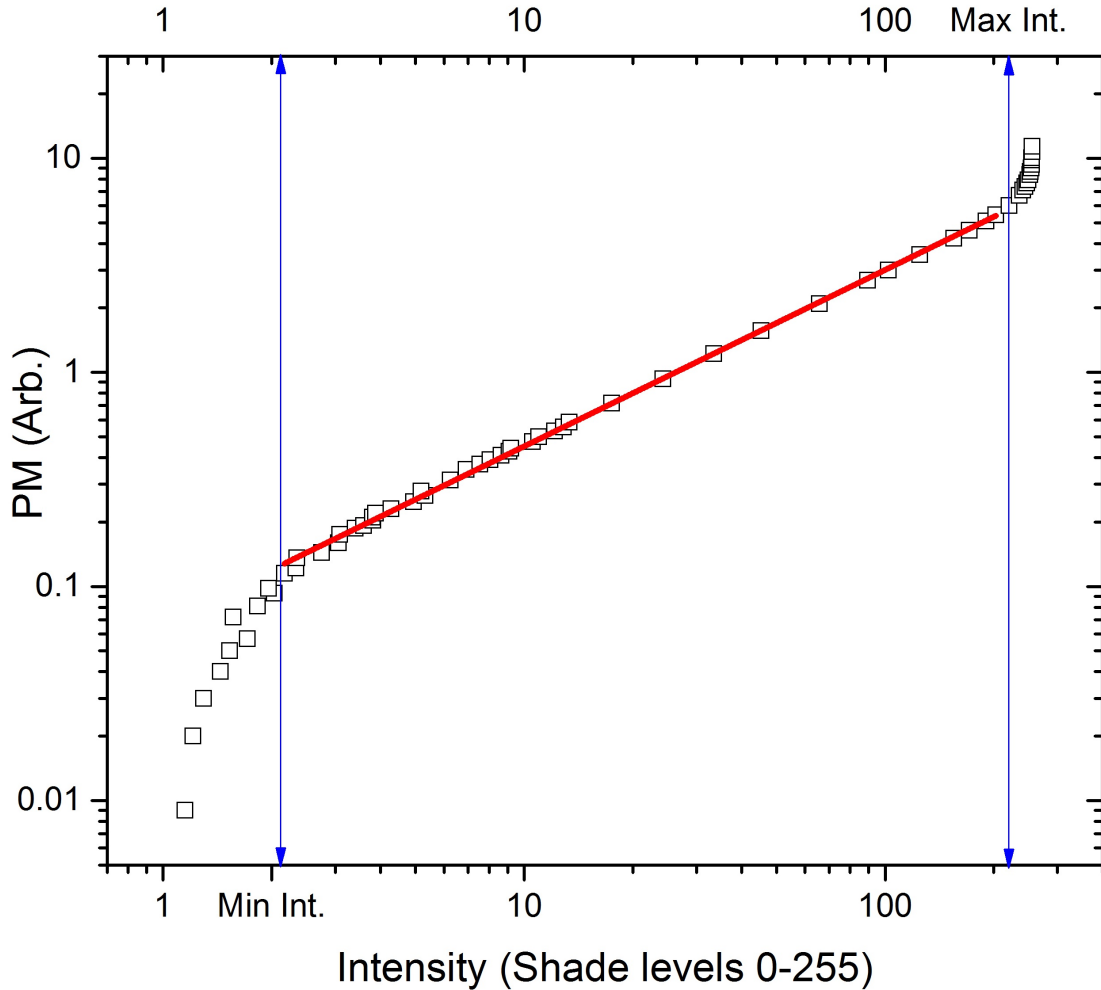


Figure 2.16: This plot shows the camera linearity. A diffuser was placed on the path of the light rays produced by a tungsten lamp while the camera (CCD) and a photomultiplier were placed in the other side of the diffuser. As a CCD camera was an 8-bit camera, so the shade levels on the x-axis is from 0-255, while the linearity of this camera was between the Min Int. $\simeq 3$ to the Max Int. $\simeq 220$.

2.4 Images Capture Procedure

This section is the core of the work, where the photos illustrated the scattering phenomena which formed the speckles on the screen when the laser hit the sample as will be discussed in this section.

Since there were many parameters (e.g. concentration, distance between sample and the screen, sample size , ..., etc.) that could be changed during the experiment, the sample's configurations were illustrated in tables next to each session of the measurements are as follows:

First, The sample was placed on the rail in its location as described in Section (2.3). Also the information of the sample was recorded in a table that similar to this table model. See Table (2.1)

Secondly, LabView Vision program (AVP) was started to check the the scattered laser intensity on the screen, where it shouldn't exceed the maximum response of the CCD which is 255. See Fig.(2.16)^{††}, so an ND filter was used to control the intensity.

Thirdly, after the intensity amount on the sample became satisfied, the AVP was closed.

Finally, the TPP program, see Section (2.3.2), was started, then the photos were taken as shown in Table (2.2).^{§§}

^{††}If the intensity is a quite enough, it may be better to reduce the intensity to the region where CCD acts linear where $\langle intensity \rangle \lesssim 220$.

^{§§}For SLS this table mostly the same, while in DLS the time intervals were modified in log mode.

Table 2.2: *Taking Photos Table Model. Here the first column is the selected number of photos and the second column determines the interval of time between images in seconds.*

Number of Photos	Intervals in sec
10	0.1
20	1
17	5
....	...
....	...
....	...
....	...

2.5 Data Analysis Methodology

For all of this work either in SLS or in DLS, LabView codes (programs) were built specially to analyze these data, where each program or code did a certain job based on the type of analysis that aimed to do.

2.5.1 Main Analysis Program (MAP)

The main purpose of this program MAP is to extract the intensity of each pixel and correlate this intensity to its position $q(\theta)$ for each image. Please check Appendix (A.3) for the front panel of this program, and for the codes which were used to build this program.

- **Images Process Methodology by using MAP**

As was mentioned above, this is the main program in the analysis process. After taking the images by using the program TPP. See Appendix (A.2), all

images that were collected during the same session were stored in one folder with the text file that included all information of the sample, then the following procedures were applied to analyze images:

1. Finding the Center of the Image

Based on the structure of the beam-filter which was used during the experiment, see Appendix (B.1), finding the center of image become pretty easy. In fact, finding the centers of the images were not a simple task before this final model of the beam-filter. For documentary, the process of finding the center of image during this work had passed through many stages or let say different methods; for example, by using some tools in AVP program, see page (44) in Section (2.1.3). These tools worked fairly ok, but they were not that accurate, another way to find the beam center was by writing some codes which gave better results than AVP tools, but they were still not very accurate.

2. Drawing The Rings

The method of analyzing the images in this work was based on taking the average of all pixels intensities along the azimuth angle from 0 to 2π on the surface of the screen as shown in Fig.(2.17). Rings of varying radius' $q's$ and a thickness of $\Delta q's$ were chosen to calculate the intensity of each pixel inside each ring, then the average of intensities inside each ring was calculated.

3. Using Analysis Programs

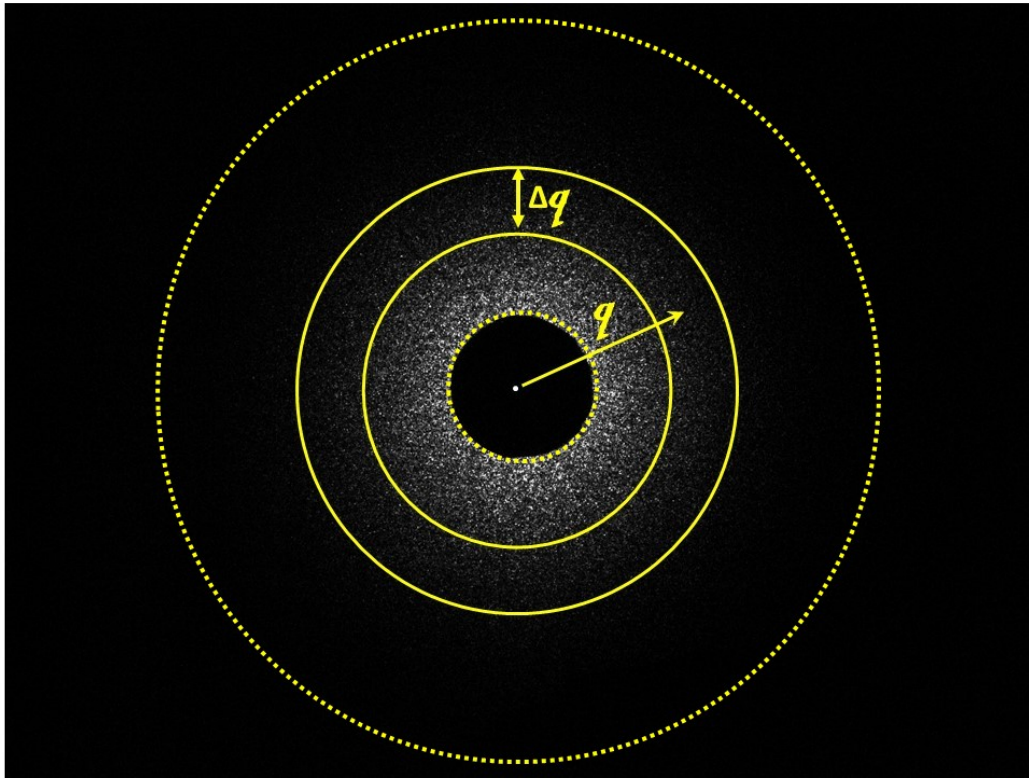


Figure 2.17: *This figure Shows the method of choosing the ring of intensity for a specific q -vector. at a specific point on the image where this point is represented by the vector q . At this q an outer ring $+\Delta q/2$ and an inner ring $-\Delta q/2$ were choosing to be the the area which includes the pixels.*

The previous two steps were the concept of calculating the q 's and the intensity average of each ring. Moreover, MAP program was the main tool to calculate them. The result was stored in a TXT file in this form model in Table (2.3).

- **How does MPA work ?**

Where the front panel of this program was large and has many keys, as to make front panel readable, the panel was split into two figures. See

Table 2.3: Table shows the out put of analysis by using MAP program. Where r is the distance from the center of the photo to point where q -intensity was measured.

r (cm)	Angles in Deg	q (cm^{-1})	Intensity Avg.
0.023	0.087	200.025	1.84
0.045	0.174	400.048	1.703
...
...
...
...

Fig.(2.18). Also, it can be seen that each of these two figures includes printed numbers which were printed on each of the figures. These numbers (groups) start from 1 on the first figure up to 13 on the second figure. The following discussion will explain how this program was used based on these printed numbers.

After the program was started, a table on the upper left corner indicated by number 1, showed the raw of the time file which was built by TPP program while taking the photos. Group (2) and (3), let the operator take action to choose which data should be included in the process. Group (4), shows the time information based on the per-knowledge of the sample you can decide if the process in the right path. In group (5) the information that can be included in the out put of the final analyzed process file. In group (6) the sample's parameters were chosen automatically, mostly by the program. Though these were checked to ensure that the process is on the track. In group (7) the number of of photos were chosen automatically by the program, but this group gives the ability to change it and to change the first photo too. The knob next to number (8) was set on (0) and the

gap (the donut thickness) was chosen to be 2 and at group (9) the "Inner R" represents the inner radius of the donut and two fields represent the start and the end angle.

In the second figure, switch (10) gives the ability to choose from two groups, 11 and 12. When the switch is in the off position which is group 11, the start angle and end angle can be chosen also the center of the image can be entered manually. For group 12 any of these fields can be chosen depending on the calculation. For more details about the codes of this program check Appendix (A.3).

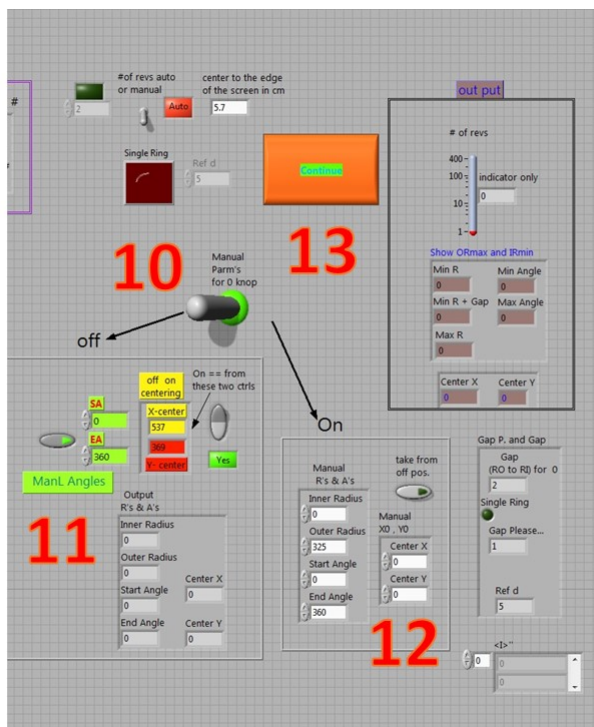
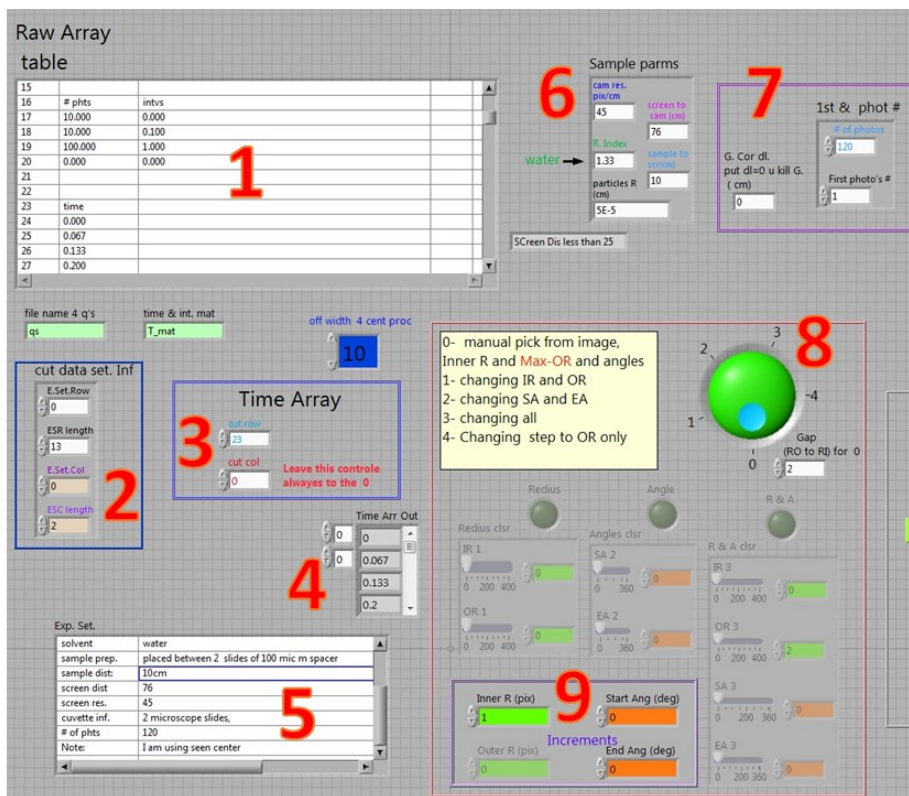


Figure 2.18: The left and right halves of the MAP programs panel. Where it was found to have two screen-shoot to illustrate this program clearly in portrait mode for the purpose of this work.

2.5.2 Box Method Analysis Program (OAP)

The main purpose of this program is to find the intensity anywhere on the image of an area of whatever size that was needed to be calculated, see Appendix (A.4). This method was based on drawing small boxes in pixels dimension. These boxes lay on the circumference of the circle where the q represents its radius check Fig.(2.19).

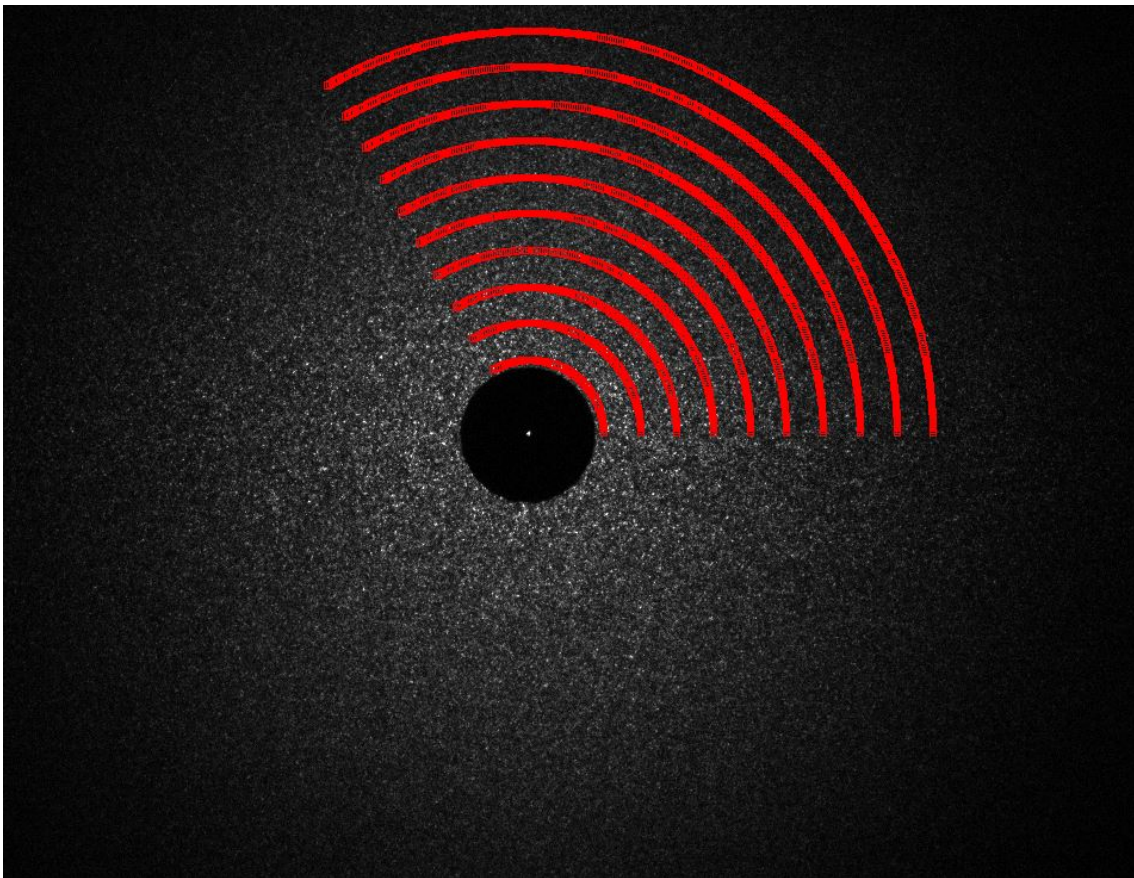


Figure 2.19: *This is a demonstration of the Box Method, where the size of the boxes were 2×2 pixels, while the gap between q and the next one was 10 pixels, and the covered angle by the boxes was 120° .*

- **Why OAP ?**

Although the MAP program, described on page (69), worked pretty good in

the calculations for static process. **MAP** was very fast in calculations. But for dynamic process, it was a necessity to add more calculations and LabView tools which really helped in the calculations as it can be seen in the next discussion of this code.

- **How does OAP program work ?**

As can be seen on the front panel (full panel in Appendix (A.4)), this panel shows different switches and by using different values in these switches. Different ways of analysis can be chosen as follows:

Since the panel of this program is of a size sufficient to fit the paper of this work, a portion of the left side of this program is shown in Fig.(2.20). Thus, includes the input on the left side of the screen and the output on the right side of the screen, as can be seen in Appendix (A.4), as it is displayed, numbers in red fonts were printed on this figure and these numbers are defined as follows:

1. **Play button**, this is the first button to be pressed in order to start the program.
2. **R's Manual Or Tool?**, this switch has two options, "Manual" and "Auto". This switch gives the ability to chose the zones on the image that were needed to be measured. Manual gives more freedom of choice.
3. **Increment**, this program gives different options to analyze the images. The **Div** option gives many options at the same time, which was preferable during this work. By pressing this key, windows (7) will display.
4. **IR Manual and OR=IR+...**, these two keys give the ability to choose

either the inner radius, outer radius, or both manually, in the case that specific radii were needed , see Fig.(2.17).

5. **1st PHT number and number of PHTS**, these two fields were chosen to determine which image to start with, and for how many images.
6. **IR and OR inc**, these two fields are for the thickness of the donut, see Fig.(2.17).
7. **DIV gaps**, here the gaps between qs and angles can be chosen, as well as the start angle and the maximum angle.
8. **cut data set. inf**, this group gives information of the chosen data (this group is important to check when mistakes happen).
9. **Manual Center**, this key gives the ability to chose the center of the image manually.
10. **Number of PHTS Manual**, this key gives the ability to chose the number of images to be analyzed.
11. **Time calculation**, this group is to take the analysis at specific times for different intervals.
12. **CONTINUE**, this key is the last key to be pressed after all settings were chosen.

- **Program Operating**

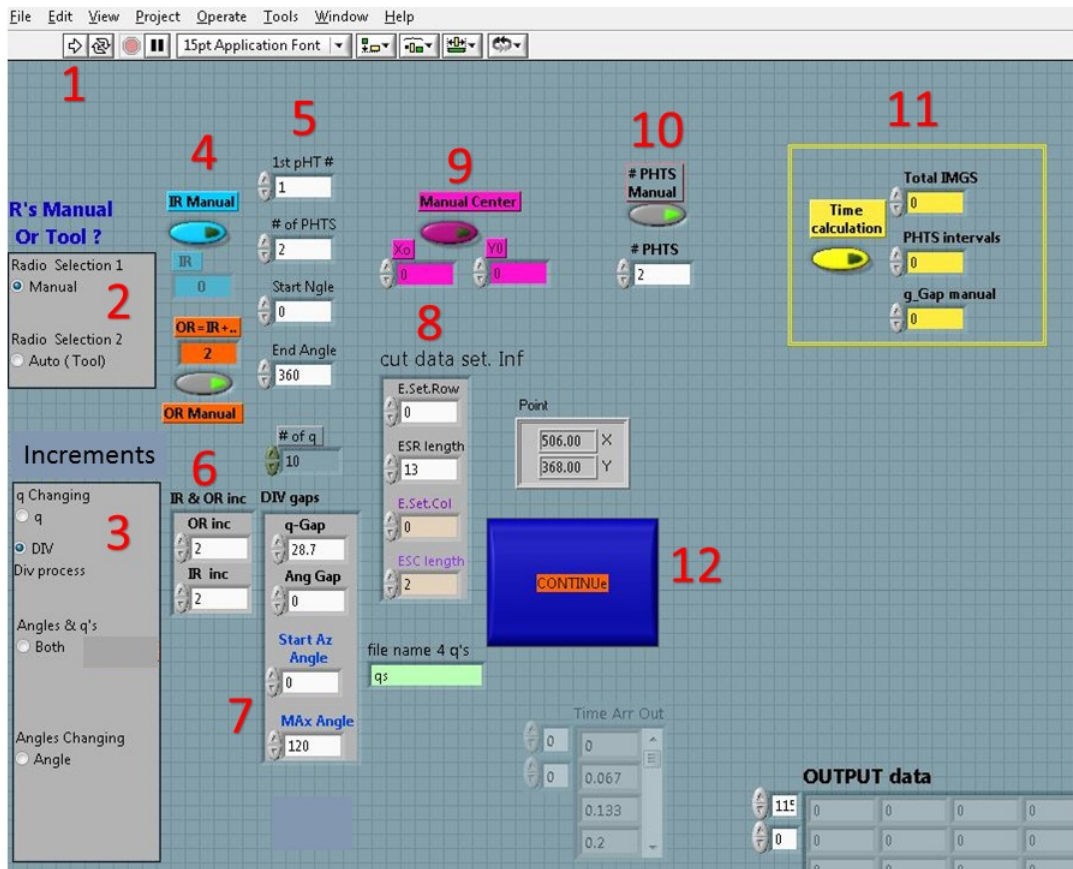


Figure 2.20: Screen shoot for the input portion of the OAP program.

After all of the images were collected in a specific folder that included the time source file, to start using the program the, following steps were taken. See Fig.(2.20) :

Button 1 was pressed to start the program. Then, the manual option was chosen from group 2, see Fig.(2.20), and the DIV section was selected from group 3. After that, the OR Manual key was pressed and the value of 2 was printed to be the width of the donut check Fig.(2.17) . At 5 the first image and the number of images were chosen. Then the value of 2 was printed in the two field of group 6. At group 7 the gap of q and the angle can be chosen. The choice depends on the type of analysis used. Also Start AZ Angle” and

”Max Angle were chosen Fig.(2.19). Based on the information included in the time file in the images folder, group 8 was modified to choose which rows and which columns were to be processed. Key 9 is optional. For key 10 the number of images were chosen to be processed either automatically (by default) or manually when the key is pressed. Key 11 was used to change the analysis which occurred at certain times (or for chosen images). The last key to be pressed was key 12, and after this key had been pressed the analysis started and the output file took the form as shown in Fig.(2.21).^{¶¶}

^{¶¶}The colors and the frames around numbers in the output file were made by using EXCEL for decoration purpose.

Date	10/23/2014									
Time	12:17 PM									
purpose	S. epi Biofilm on PFTS Dynamic									
Particle DIAsize	2.00E-04									
coposition	bacteria, extracellular polysaccharide matrix									
solvent	PBS									
sample prep.	17 h Dynamic in TSB									
sample dist:	50cm									
screen dist	37									
screen res.	91									
cuvette inf.										
# of phts	100									
Note:										
	Distance (cm)	1.47253	1.58132	3.9747					
	Ang Deg:	1.68776	1.81237	4.5475					
	PHYI	2.28021	2.44848	6.1346					
	q (cm-1)	3887.92	4174.953	10473					
# of Images	Time	I tot	I s.d	I t.b	I t.b Sd	Intensity	Intensity St.div.	Sq_R_Diff	Abso. Diff.	
1	0	3.80	3.89	1.80	1.90	6.71443	3.58432	0	0	0
2	0.931	3.78	3.95	1.67	1.86	6.714	3.59111	0.74839	0.25118	0.1059
3	1.931	3.76	3.93	1.66	1.86	6.71696	3.58845	0.77398	0.26226	0.10999
4	2.93	3.80	3.94	1.81	1.98	6.72943	3.59622	0.77985	0.26594	0.11319
.....
100	98.896	3.83	4.01	1.63	1.79	6.79367	3.67871	1.32874	0.39172	0.12471

I tot : Total intensity
 I s.d : Total intensity Standard div.
 I t.b : Through beam intensity
 I t.b.Sd : Through B. Standard div.

Figure 2.21: The OAP output file, where on the left upper corner table is the information that come from TPP program, while the lower part has the processed images data. The left side table has the photos number column, time column, through beam intensity,, etc. Next big table, on the right has four groups, intensity, intensity standard div., R_Sq_Diff, and absolute difference. Each one of these groups has the same references data which shown on the shaded rows over these groups.

2.5.3 Spherical to Plane Wave Front Correction

By either using MAP or OAP to analyze the images, the image wave front is geometrically spherical in its propagation to the flat screen. But unfortunately dealing with curve screen image capturing is not easy, while correcting the captured image because if these two spaces is necessarily specially for wide angles (large q) or close screen as it is shown in the next derivation which was derived by professor Zozulya, Physics department, WPI, Massachusetts. See Fig.(2.22).

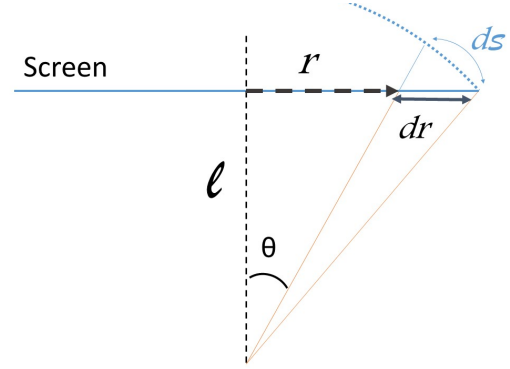


Figure 2.22: This scheme for the correction derivation, where l is the distance from sample to the screen, r is the distance of the speckle from the screen center, and θ is the scattering angle.

$$dI(\theta) = f(\theta) d\Omega,$$

$$r = l \tan(\theta),$$

so,

$$dr = \frac{l}{\cos^2(\theta)} d\theta,$$

where, $I(\theta)$ is the intensity of scattered light at an angle θ .

But,

$$dS = 2\pi r dr = 2\pi \frac{l^2 \sin(\theta)}{\cos^3(\Omega)} d\theta,$$

where,

$$d\Omega = 2\pi \sin(\theta)d\theta,$$

so,

$$dS = \frac{l^2}{\cos^3(\theta)} d\Omega.$$

Thus,

$$\frac{dI}{dS} = \frac{f(\theta)}{l^2} \cos^3(\theta).$$

So,

$$f(\theta) \sim \frac{1}{\cos^3(\theta)} \frac{dI}{dS},$$

where, $\frac{1}{\cos^3(\theta)}$ is the correction factor.

Chapter 3

LATEX SPHERES

Introduction

The last chapter covered the methodology of the experiment. The measurements as well as the core programs that were used to analyze the data were reviewed. This next chapter will show the results during the experiment. It will also will go through all calculations and plots discussion in detail.

3.1 Results

3.1.1 Effect of Concentration

Where single scattering is essential for light scattering experiments [68]. Also, the behavior of light scattering is known which results from the fact that this experiment was done for a long time. So, in this partof work, a $2\mu\text{m}$ size-particle of varied

concentrations was used to estimate the effect of concentration in single scattering regime.

The first measurement was done with a concentration of $D_0 = 3.63783 \times 10^7 p/mL$. This concentration was then diluted to half concentration $D_{1/2}$, then to 1/4 concentration $D_{1/4}$, with the final sample made of water only. These samples were exposed to the laser beam for 101 second and a 120 photos were taken of the screen during this interval of time, where sample was place at a distance of 20 cm from the screen. The plot of average scattered intensity $\langle I \rangle$ versus q is plotted in Fig.(3.1).

From Fig.(3.1), it can be seen that water curve is the only slightly different from the rest of the curves. Moreover, the other three curves is mostly identical in the shape*.

*The intensity of each curve is arbitrary, so it is not significant in the comparison.

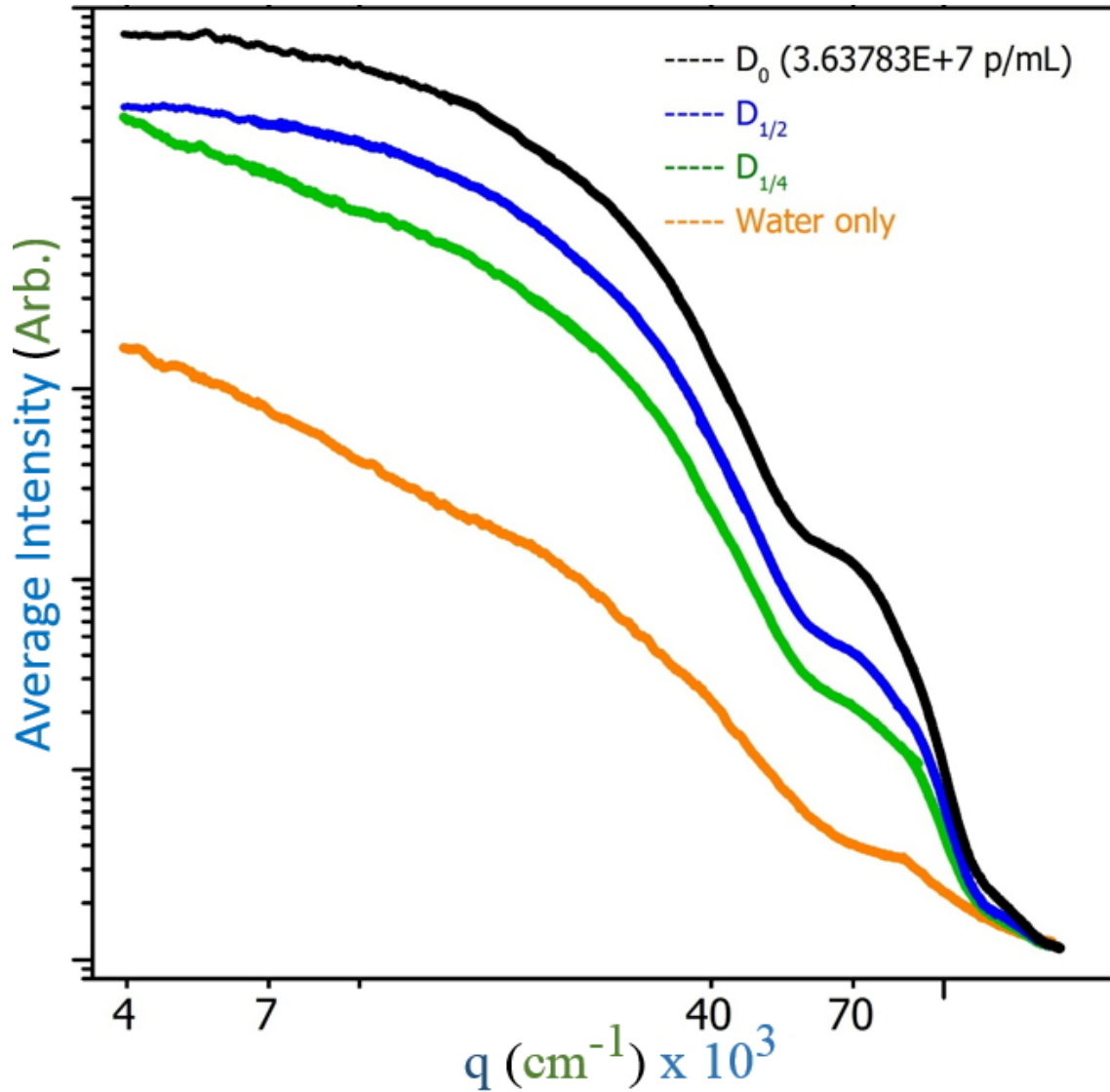


Figure 3.1: The effect of different concentrations on the behavior of scattering curves for $2\mu\text{m}$ size-particle which has varied concentrations, starting by the concentration $D_0 = 3.63783 \times 10^7 \text{ p/mL}$, then, this concentration was diluted to the half $D_{1/2}$, to the fourth $D_{1/4}$, ending with pure water as a zero concentration.

3.1.2 Static Light Measurements

3.1.2.1 Finding Radius of gyration by using Guinier Plot

As it was mentioned in section (1.2.3), *static light scattering* has some useful tools that can be used to calculate some of physical properties of dispersed particles in

solutions, e.g. radius of gyration R_g and the molecular weight M_w .

■ Latex particle of size $2\mu\text{m}$

For the $2\mu\text{m}$ spherical Latex particles' sample, check Section (2.1.2) the distance between the sample and the screen was 15 cm, the data was collected and organized in a table, where the sample concentration was $\phi = 1.818 \times 10^7 p/mL$. This solution was placed between two microscope slides as explained in section (2.2.2). 50 photos were then taken by the CCD camera at a distance of 77 cm from the screen for 20 minutes. The data was analyzed by using the **MAP** program to extract the intensity $\langle I \rangle$ for each q as described in the section (2.5.1).

The average intensity $\langle I \rangle$ versus q^2 was plotted as shown in Fig.(3.2), where Guinier's law was applied, check Eq.(1.2.57). A fitting line was plotted over the straight portion of the natural logarithm of the average intensity $\langle I \rangle$ versus q^2 at a small angle ($q \times R \leq 1$).

■ Latex particle of size $1.0\mu\text{m}$

The same procedure was done for a $1\mu\text{m}$ particle of a concentration $\phi = 5.82052 \times 10^8 p/mL$, with the same rest parameters were used as described for the $2\mu\text{m}$ particle.

Also, by applying the same procedure as same as in $2\mu\text{m}$ particle, a similar plot for the $1\mu\text{m}$ was plotted as shown in Fig.(3.3).

■ Latex particle of size $0.5\mu\text{m}$

For the $0.5\mu\text{m}$ spherical Latex particles' sample, see section (2.1.2), the data was collected and organized in a table as similar as in $2\mu\text{m}$. Where the sample concentration was $\phi = 1.8625 \times 10^{10} p/mL$, and the distance between the sample

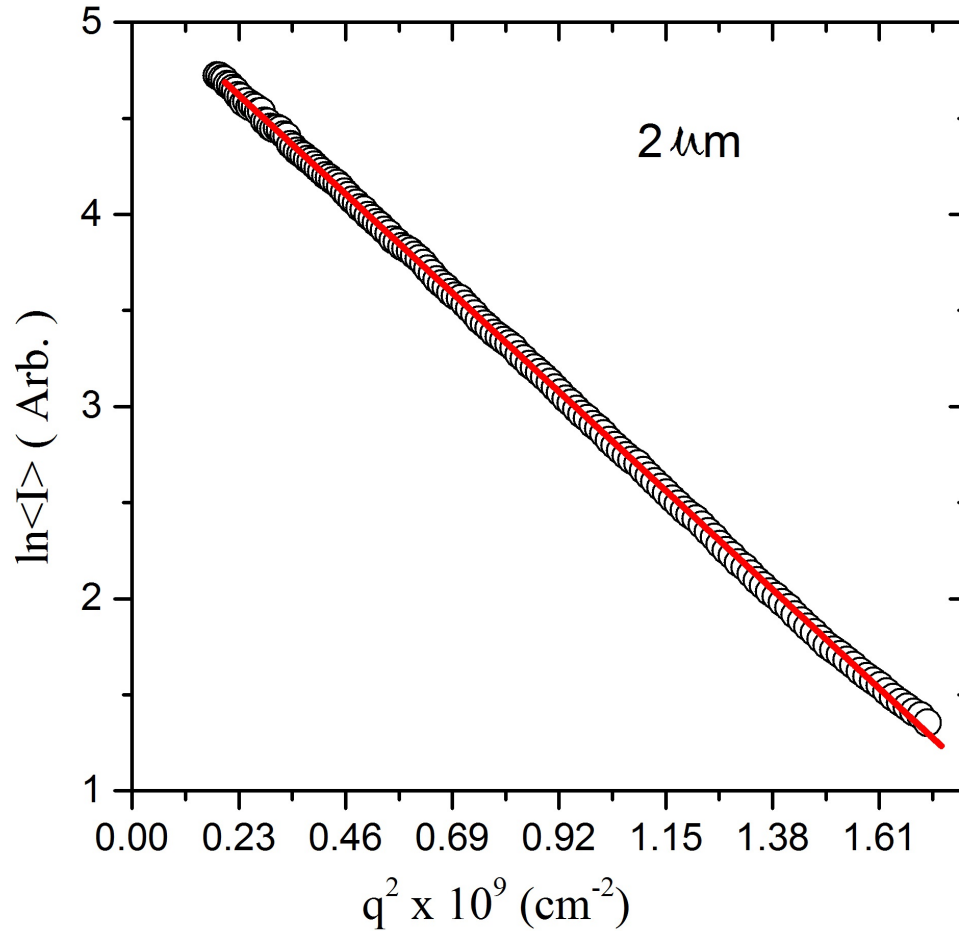


Figure 3.2: A plot of q^2 vs $\ln(I)$, where the sample of $2 \mu\text{m}$ latex sphere particles were dispersed in water to give a concentration of $\phi = 1.818 \times 10^7 \text{p/mL}$. This sample were placed at 15 cm from the screen, and by using the CCD camera 50 photos of the screen were taken during the interval of 20 minutes.

and the screen was 15 cm. This solution was placed between two microscope slides as explained in section (2.2.2), then 50 photos shots were taking by the CCD camera at 77 cm distance from the screen for 20 minutes. These data were analyzed by using the **MAP** program to extract the intensity $\langle I \rangle$ for each q as described in the section (2.5.1).

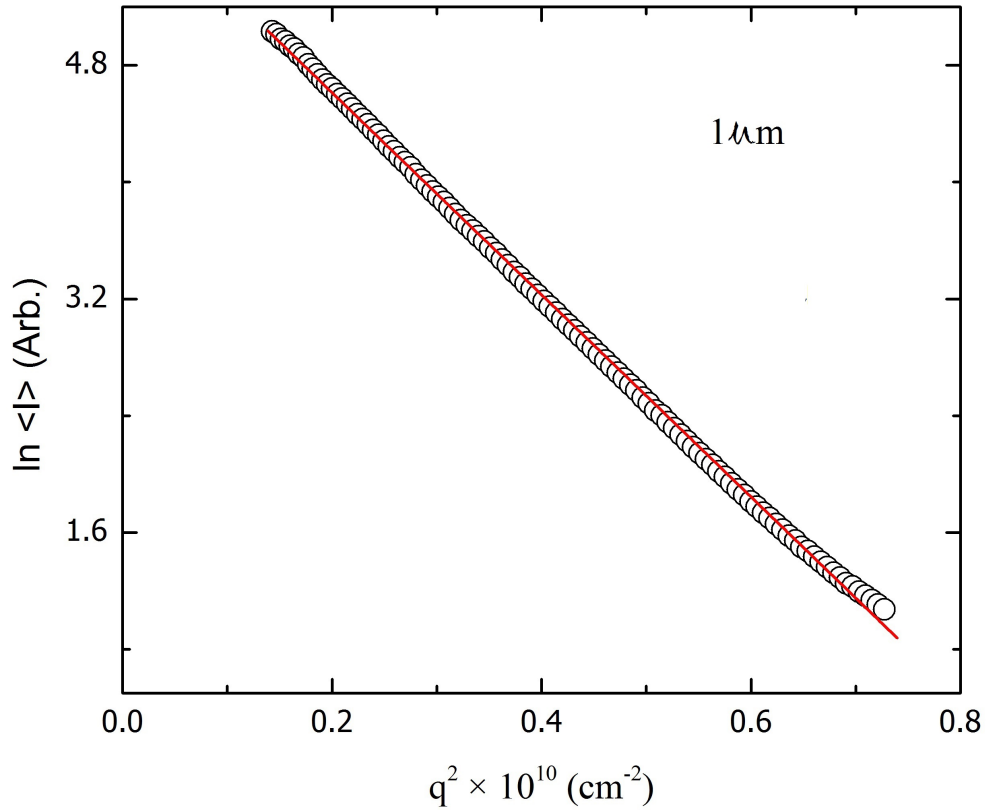


Figure 3.3: A plot of q^2 vs $\ln(I)$, where a sample of $1 \mu\text{m}$ latex sphere particles were dispersed in water to give a concentration of $\phi = 5.82052 \times 10^8 \text{p/mL}$. This sample was placed at 5 cm from the screen and by using the CCD camera, 50 photos of the screen were taken during the interval of 20 minutes.

After the data was analyzed, Guinier's law was applied as the same as done for the $2 \mu\text{m}$ and $1 \mu\text{m}$. See Eq.(1.2.57) Then, a fitting line was plotted over the straight part of the natural logarithm of the average intensity $\langle I \rangle$ versus q^2 at a small angle ($q \times R \leq 1$). The result of the plot is shown in Fig.(3.4).

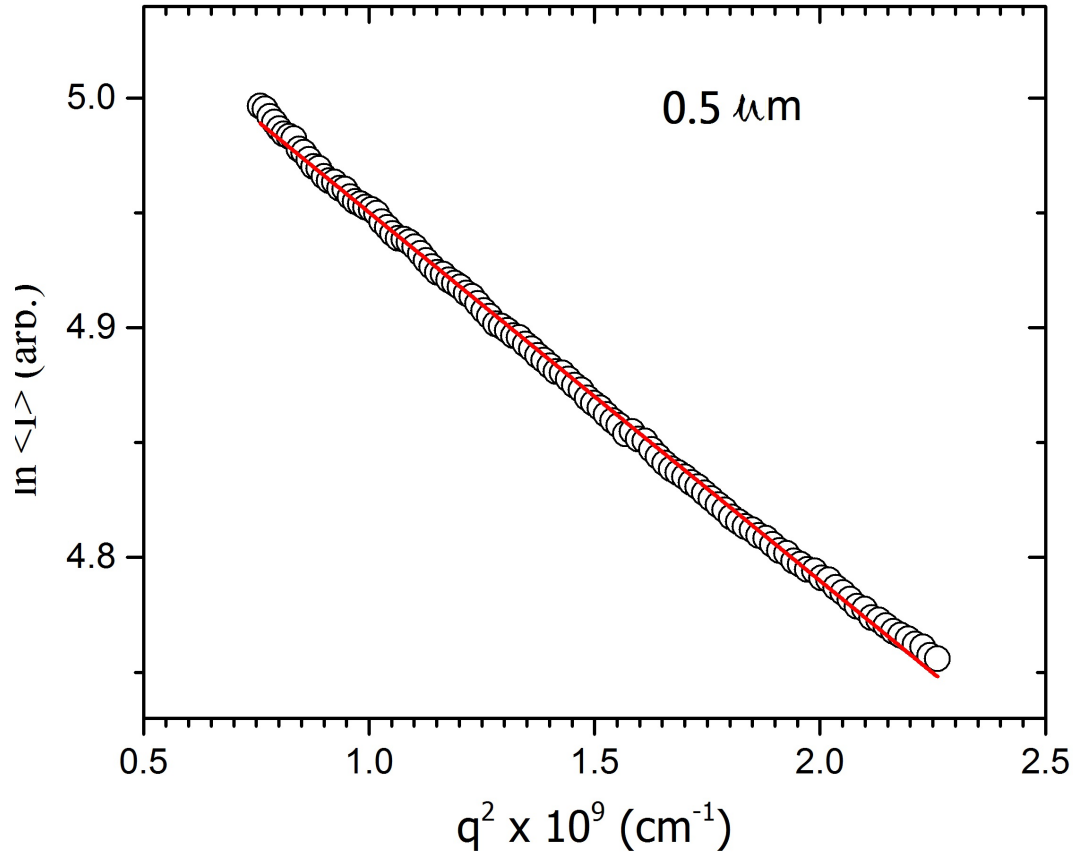


Figure 3.4: A plot of q^2 vs $\ln(I)$, where the sample of $1/2 \mu\text{m}$ latex sphere particles were dispersed in water to give a concentration of $\phi = 1.8625 \times 10^{10} \text{p/mL}$, where this sample placed at 15 cm from the screen and by using the CCD camera 50 photos of the screen were taken during the interval of 20 minutes.

3.1.2.2 Fractal Dimension Test

By using Eq.(1.2.64) in section(1.2.3) it is possible to test the change of the shape of any particles in solutions [69]. For example if $\log_{10}(I)$ vs $\log_{10}(q)$ is plotted for different events (times) and by studying the trends of the produced curves, will be able to see the changes in the shape of particles during the experiment, check Fig.(3.5) for $2.0 \mu\text{m}$, and check Fig.(3.6) for $1.0 \mu\text{m}$, also check Fig.(3.7) for $0.5 \mu\text{m}$

particle.

Based on the different regimes which are constrained with the quantity R_g^{-1} as shown in Fig.(1.8) in Section (1), all of the above figures were combined in one figure as shown in Fig.(3.8) , where it can be seen that the curve of $2\mu\text{m}$ stoops more than $1.0\mu\text{m}$ and $0.5\mu\text{m}$. The three lines of the slopes, -1, -2, and -3 to represent the 1D, 2D, and 3D objects dimensions respectively. The $2\mu\text{m}$ particles' curve was laid with decent accuracy over the -3 slope, on the right side of the $2\mu\text{m}$ constraint $1/R_g$, see the structure factor in Section (1.2.3).

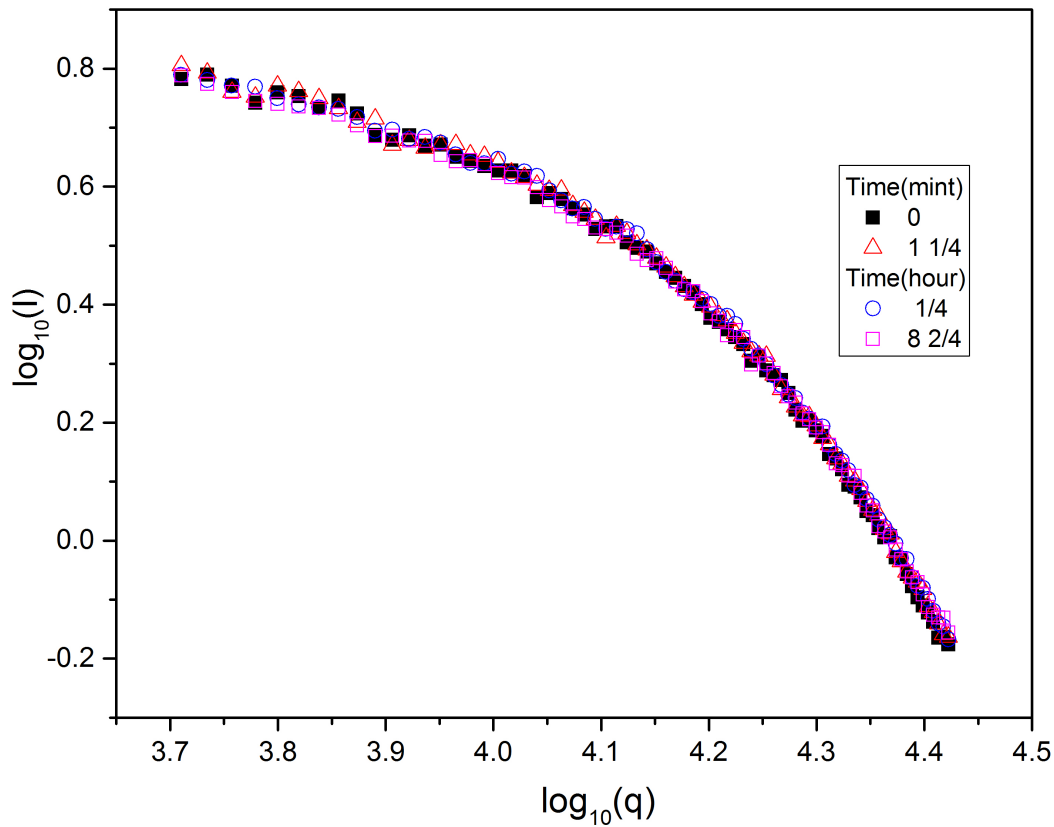


Figure 3.5: *The fractal dimension plot for $2\mu\text{m}$ latex particles at different times, where it can be seen that there is no change of the latex particles during the experiment.*

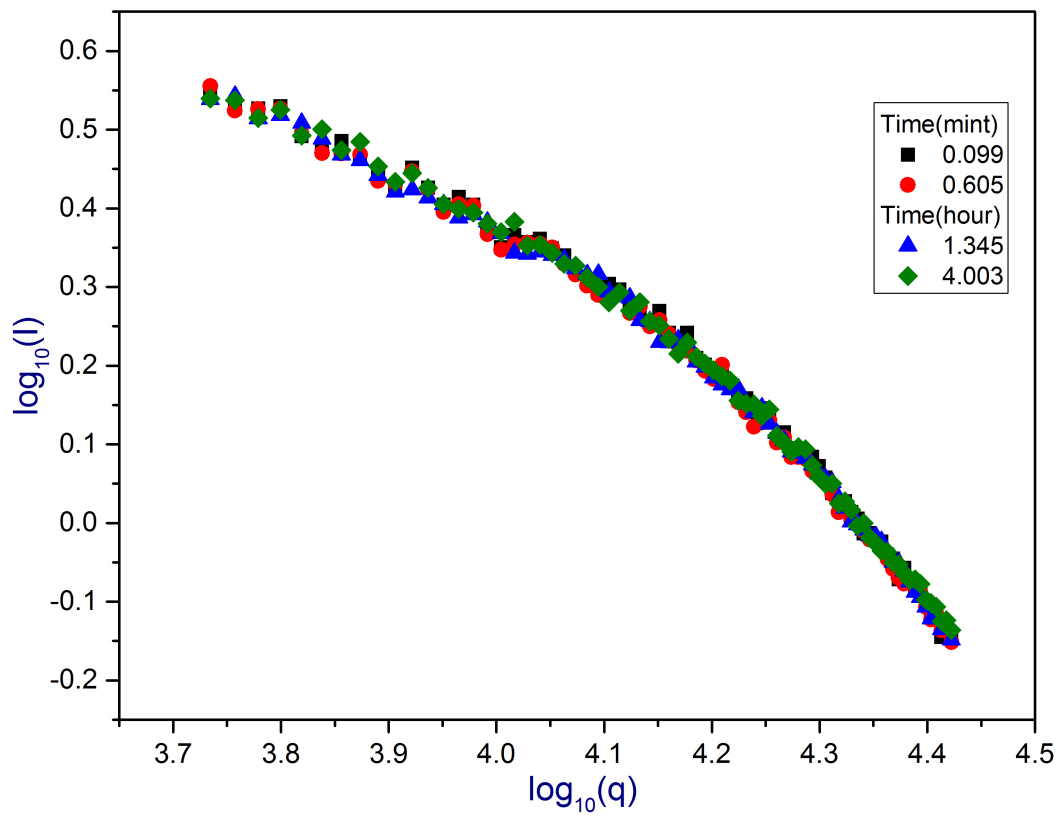


Figure 3.6: *The fractal dimension plot for $1\mu\text{m}$ latex particles at different times, where it can be seen that there is no change of the latex particles during the experiment.*

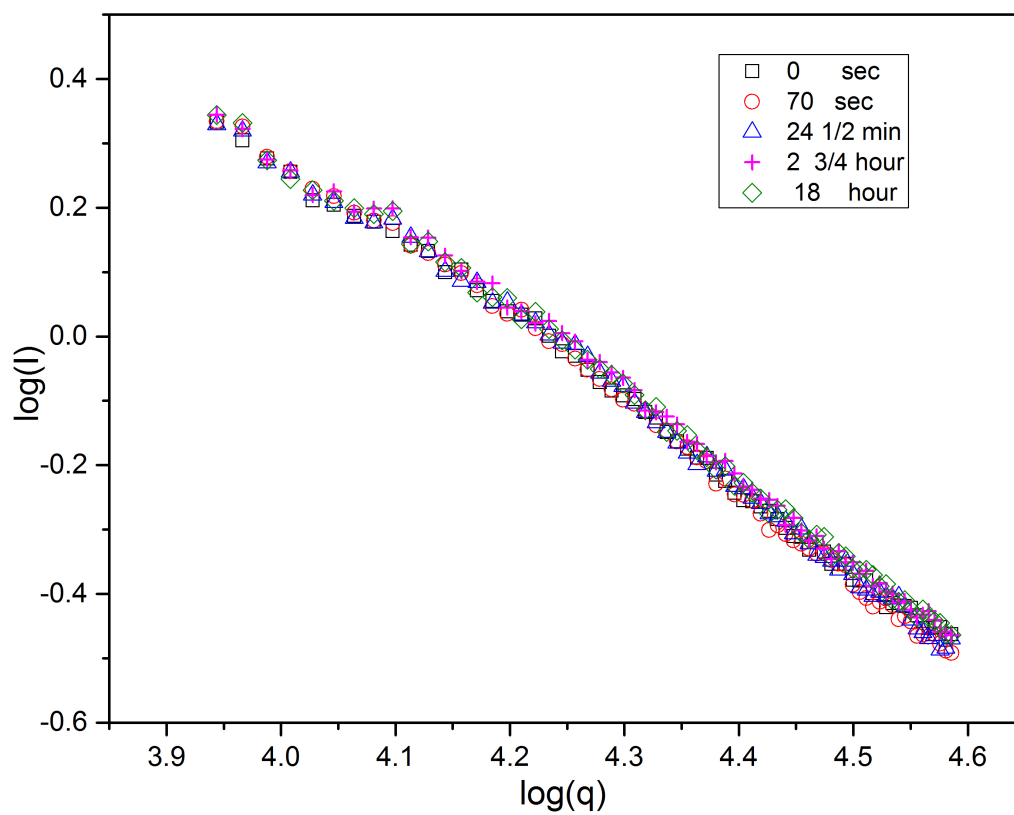


Figure 3.7: *The fractal dimension plot for $0.5 \mu\text{m}$ latex particles at different times, where it can be seen that there is no change of the latex particles during the experiment.*

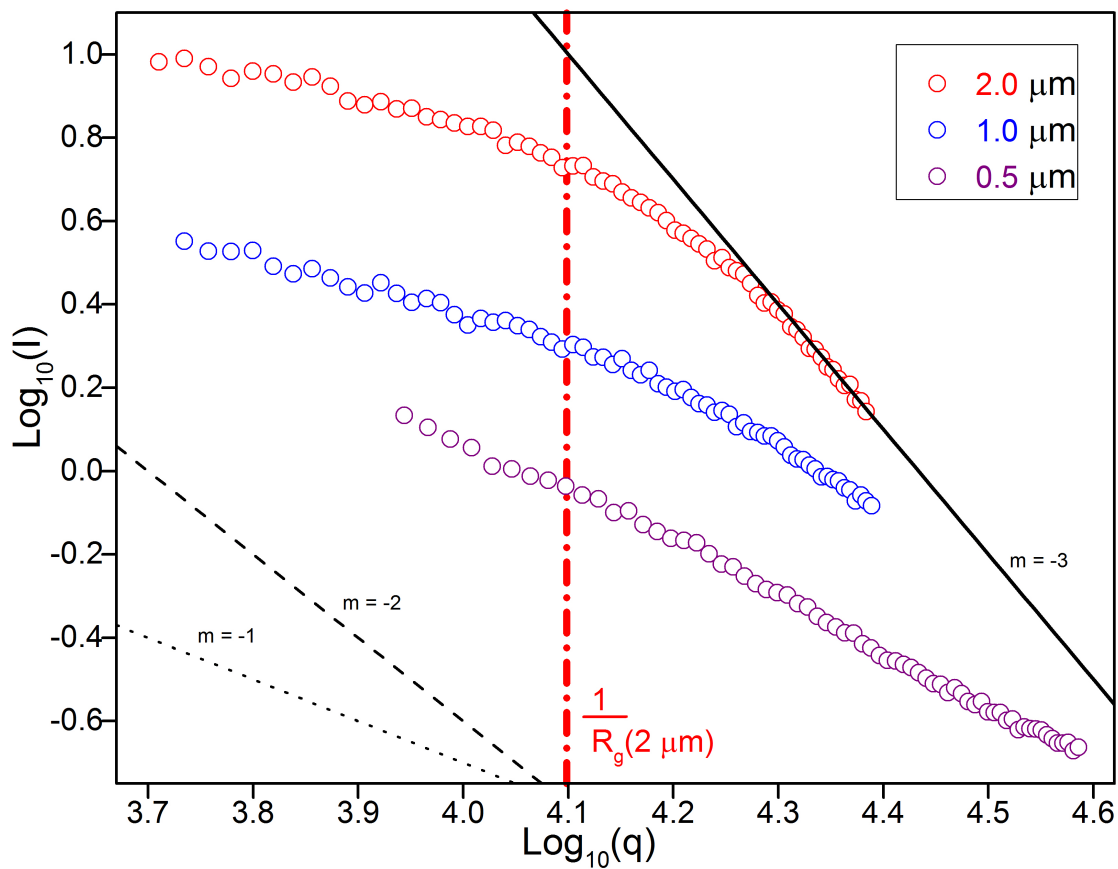


Figure 3.8: a comparison of the 2.0, 1.0, and 0.5 μ latex spheres scattering on a log-log plot. To illustrate the ideal power law of 3D sphere, a solid line of slope -3 is overlaid. for reference the power law for surfaces (slope = -2) and lines (slope = -1) are shown for 2D and 1D, respectively. [70]

3.1.3 Dynamics Light Measurements

3.1.3.1 Defining The Root Square Difference

This technique was achieved by using the OAP program, check Section (2.5.2) "DIV" key. The benefit of this technique was to check the dynamic trend of the samples.

The principle of this code is to subtract the intensity of each image from the start image intensity[†], where the result was represented in two columns, the 1st column was the time of the subtracted image and the second one was the Root-Sure-Difference "R_Sq_Diff" of the intensities.

- R_Sq_Diff for latex particles

The 2 μm latex particles which were dispersed in water such that the mixture had a diluted concentration of $3.63783 \times 10^7 p/mL$. This solution was placed in a cuvette of size 10×10 mm of 3.5 mL capacity. This sample was then exposed to the laser for 48 hours. The sample was placed at a distance of 70.8 cm and the screen was placed at a distance of 100 cm from the camera. The Start image for this run was the image number one[‡]. The result of this run was organized listed in a table.

The plot of R_Sq_Diff versus time is shown in Fig.(3.9) for several q 's. Also $q = 3600 \text{ cm}^{-1}$ was picked to be plotted again in Fig.(3.10), where it can be seen clearly in these figures that the trends of the curves differ as time progressed.

[†]Could be the first image, the tenth one or the 100th based on the way of analysis.

[‡]Some time the image number one is called zero image, where it was taken at time zero.

On the other hand, this behavior of the R_{Sq_Diff} curve is not seen for the $1\mu\text{m}$ particles as shown in Fig.(3.12) nor for the $0.5\mu\text{m}$ as seen in Fig.(3.13) .

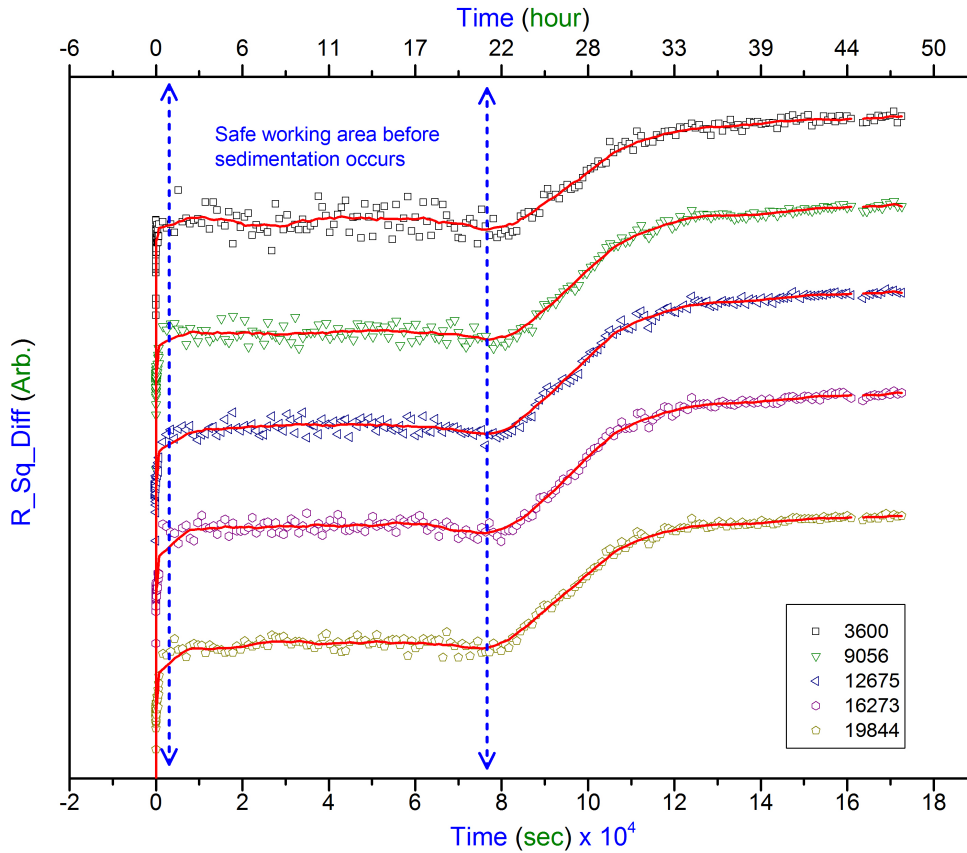


Figure 3.9: Evolution of the R_{Sq_Diff} as a function of time at different q 's for 48 hours for $2\mu\text{m}$ latex particles which were dispersed in water to have a diluted solution of concentration $3.63783 \times 10^7 \text{p/mL}$. This solution was placed in a cuvette of size $10 \times 10 \text{ mm}$ of 3.5 mL capacity

By looking at Fig.(3.9), it can be seen that the initial trend of curves start from zero time until 10 seconds, the second trend starts from the end of the first one and stays as a plateau until 20 hours, which is the start of third stage. The third stage showed a raising in the curve until 33 hours. The last phase starts from the end of the third one and continued as a plateau until the end of the experiment's time.

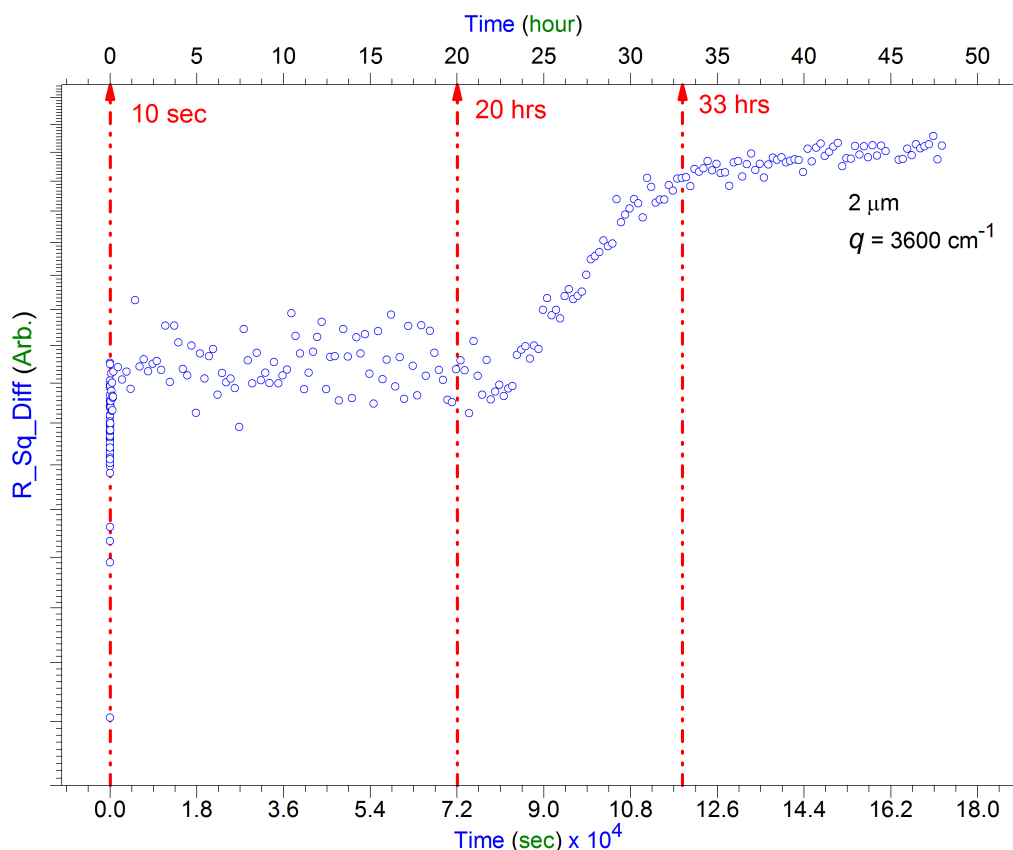


Figure 3.10: Evolution of the R_{Sq_Diff} as a function of time for $2 \mu\text{m}$ particles, where a solution of $3.63783 \times 10^7 \text{ p/mL}$ concentration of these particles placed in a $10 \times 10 \text{ mm}$ cuvette and it exposed to the He-Ne laser for 48 hours. Dashed lines distinguishes between the different trends of intensity during this interval of time.

As it can be seen in Fig.(3.12) and Fig.(3.13) that there is no change in the $1.0 \mu\text{m}$ nor in the $0.5 \mu\text{m}$ regarding the dynamics with time as it has been indicated by **R_Sq_Diff** tool.

- Short Time Zone and Relaxation Time

From Fig.(3.10), note that the data at very short periods exhibits a sharp rise with time, indicating a short time relaxation dynamic which is not connected to the long time evolution as seen at much later times. In Fig.(3.11), the same data is plotted on a logarithm-time scale to better show this behavior. For

2 μm size latex spheres in water, the expected relaxation time for Brownian motion is about 1 ms [71]. Given that the time between images is no shorter than 1/15 sec, this initial sharp rise is likely the tail-end of the Brownian relaxation mode.

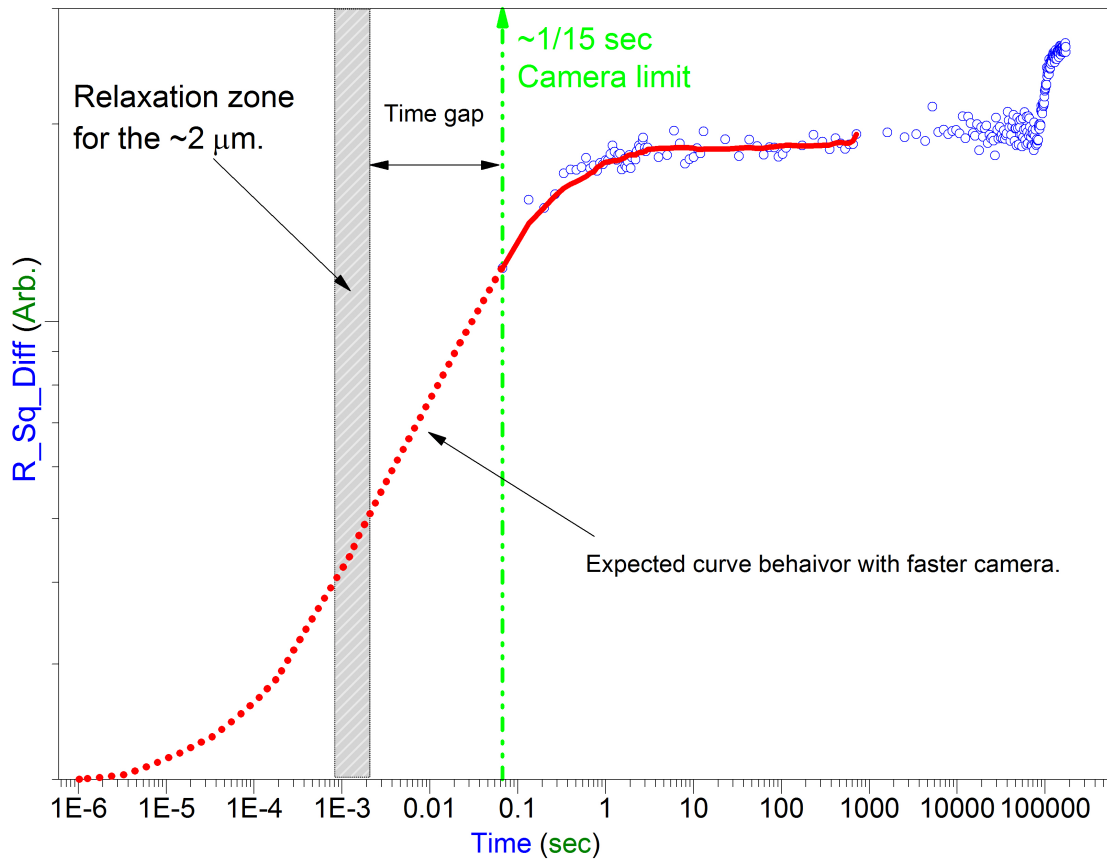


Figure 3.11: Evolution of the R_Sq_Diff as a function of time on logarithmic scale indicating the data trend at much shorter experimental times. The solid red curve depicts the trend of the actual data but below 0.06 sec, the shortest time between images, a dotted red line is used to illustrate the expected behavior. The gray shaded area is the range of relaxation times for 2 μm latex beads in water due to Brownian motion taken from Ref. [71].

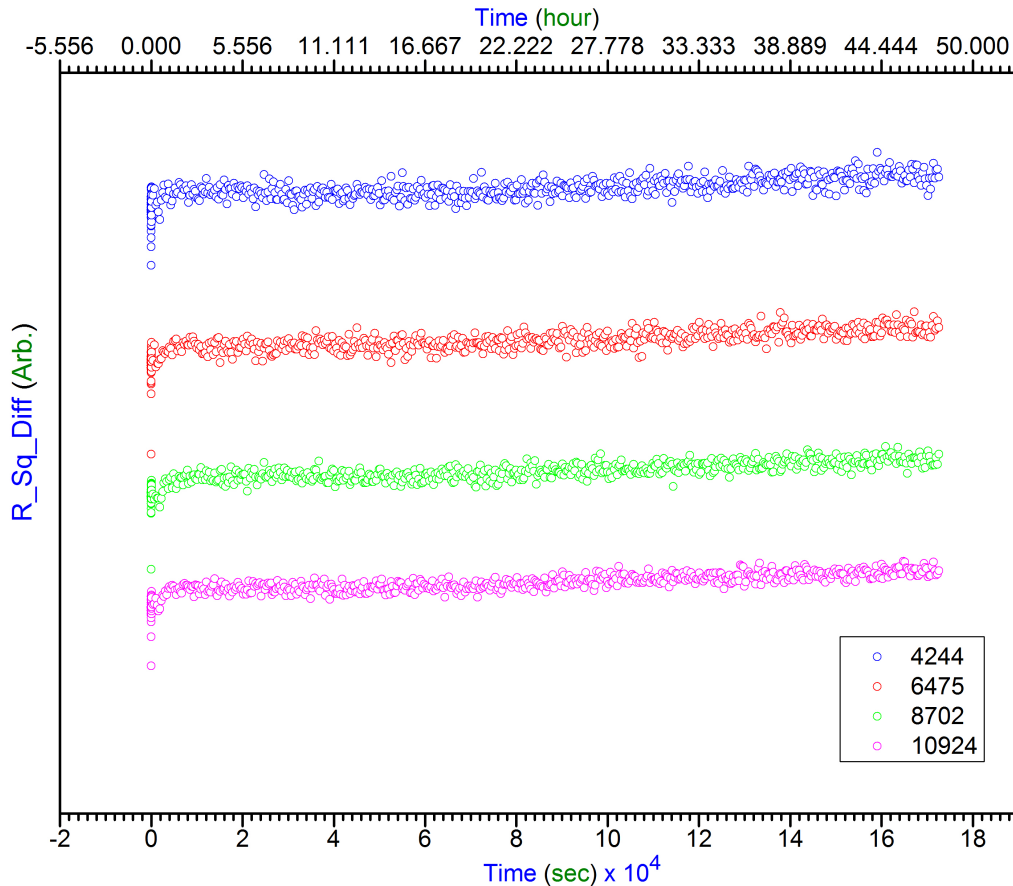


Figure 3.12: Evolution of the R_{Sq_Diff} as a function of time at different q 's for 48 hours for $1.0 \mu\text{m}$ latex particles, which were dispersed in water to have a diluted solution of concentration 4.5×10^8 p/mL. This solution was placed in a cuvette of size 10×10 mm of 3.5 mL capacity.

3.1.3.2 Sedimentation process

Based on the knowledge that was collected from the R_{Sq_Diff} 's analysis, it is very clear that there is a drop of the intensity after 20 hours as shown in Fig.(3.14) for the $2 \mu\text{m}$ latex particles. The high scattering was due to an even dispersion of the particles in the medium. This resulted in a drop in intensity as the particles settled.

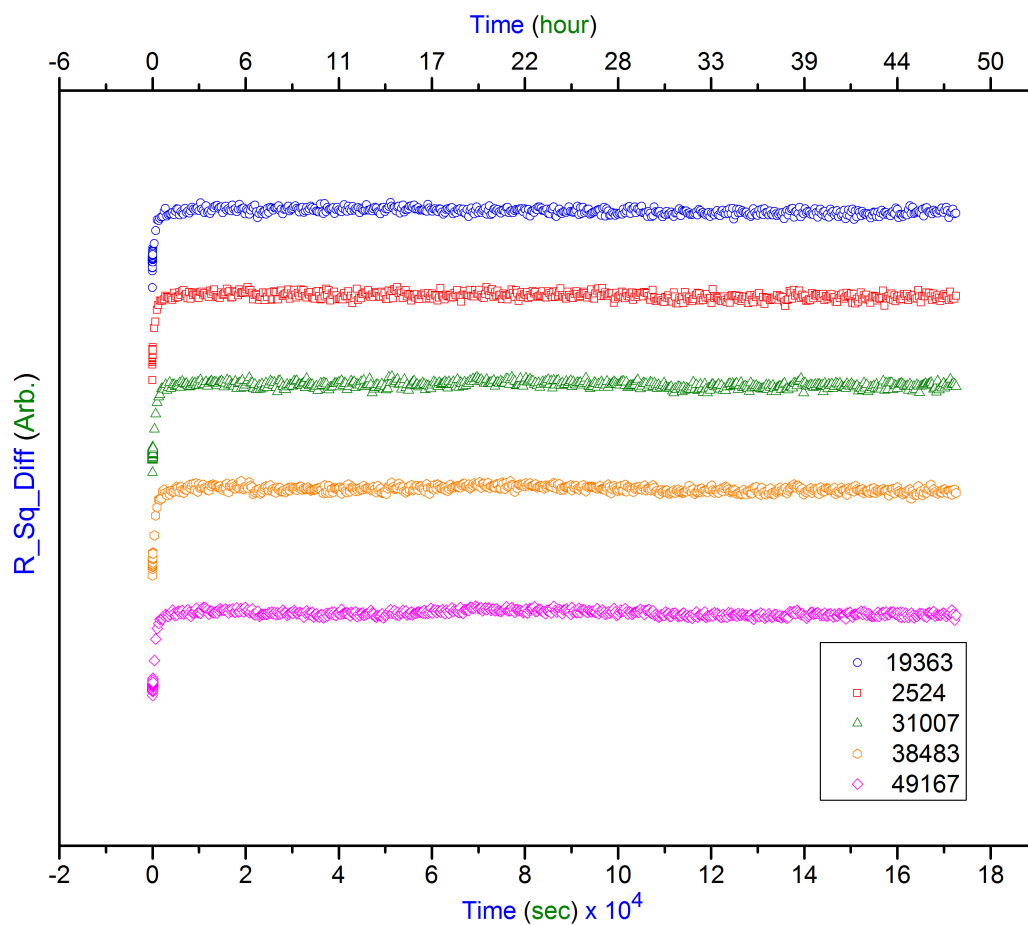


Figure 3.13: Evolution of the R_{Sq_Diff} as a function of time at different q 's for 48 hours for $0.5 \mu\text{m}$ latex particles which were dispersed in water to have a diluted solution of concentration 6×10^{10} p/mL. This solution was placed in a cuvette of size 10×10 mm of 3.5 mL capacity.

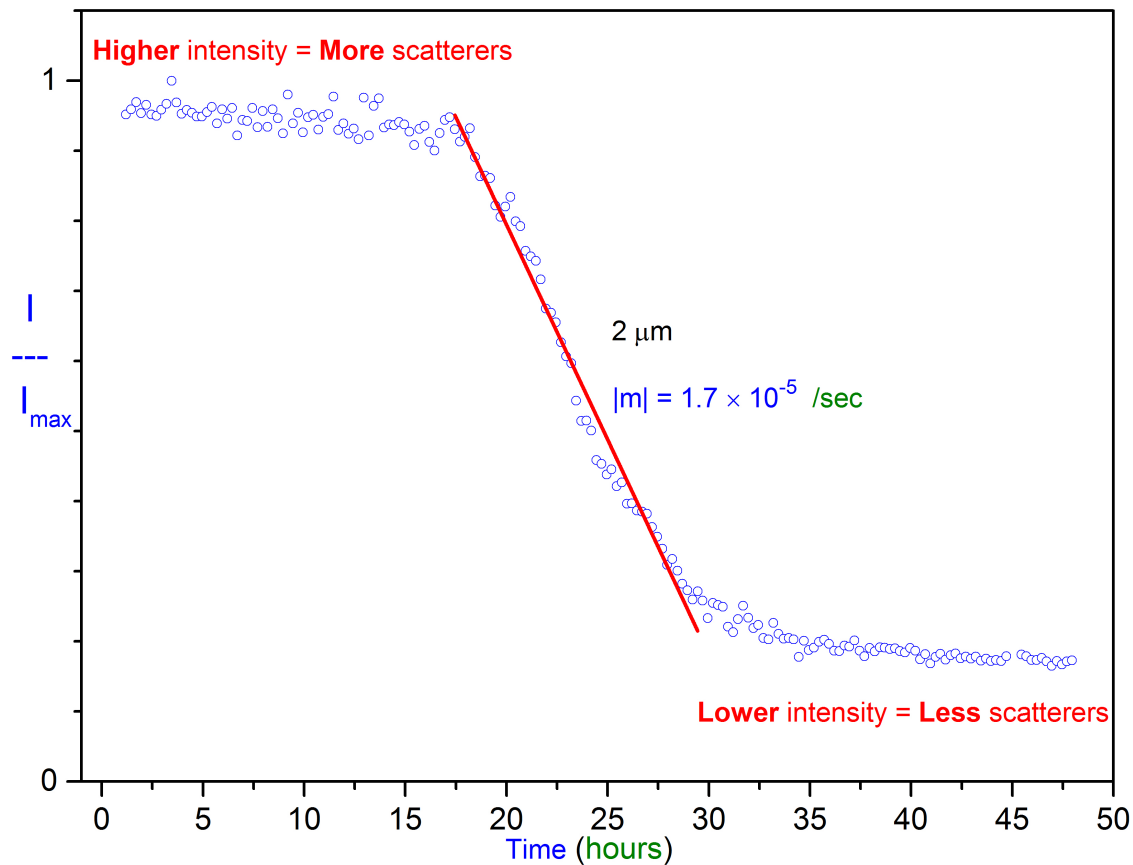


Figure 3.14: The sedimentation of $2\mu\text{m}$ in water is illustrated in this figure where Normal total intensity I/I_{max} versus Time was plotted. A sample of $3.63783 \times 10^7 \text{p/mL}$ concentration was contained in $10 \times 10 \text{ mm}$ cuvette and it was exposed to the laser for 48 hours at room temperature of $25^\circ\text{C} \pm 1$.

3.2 Discussion

3.2.1 Effect of Concentration

From the Fig.(3.1), it can be seen that the behavior of different concentrations for D_0 , $D_{1/2}$, and $D_{1/4}$ are the same. This indicates that this ranges of concentrations is ok for the single scattering regime. While it was seen that for high concentration, more scattered light was detected, which means less effect of the background in the results. In simple words, if possible, having higher concentrations always better if and only if one is avoiding multi-scattering effect and preventing CCD saturation too.

3.2.2 Static Light Scattering Measurements

3.2.2.1 Finding Radius of gyration by using Guinier Plot

■ Latex particle of size $2\mu\text{m}$

Now from the Fig.(3.2), the calculation of Radius of gyration can be made as follows:

$$Slope = \frac{R_g}{3}$$

So,

$$R_g = \sqrt{3 \times Slope}$$

And from the figure we can see that $|Slope| = 2.2 \times 10^{-9} cm^2$, so:

$$\begin{aligned} R_g &= \sqrt{3 \times 2.2 \times 10^{-9}} \\ &= 0.812 \mu m \end{aligned}$$

But the relation between R_g and the actual R (radius of the particle) for a rigid sphere [72] is:

$$\begin{aligned} R &= \sqrt{\frac{5}{3}} \times R_g \\ &= 1.05 \mu m \end{aligned}$$

So, for the whole diameter $2R$,

$$2R = 2.1 \mu m \tag{3.2.1}$$

The result shown in Eq.(3.2.1) indicates that the findings are 95% accurate when compared to the manufacturer's worksheet as displayed in the table (3.1).

■ Latex particle of size $1.0 \mu m$

From this plot in Fig.(3.3), the same calculations which were made for $2.0 \mu m$, were also made for the $1.0 \mu m$ as follows:

$$Slope = \frac{R_g}{3} \tag{3.2.2}$$

So,

$$R_g = \sqrt{3 \times Slope}$$

And from the figure we can see that $|Slope| = 6.9 \times 10^{-10} cm^2$, so:

$$\begin{aligned} R_g &= \sqrt{3 \times 6.9 \times 10^{-10}} \\ &= 0.45 \mu m \end{aligned}$$

So, R is equal :

$$\begin{aligned} R &= \sqrt{\frac{5}{3}} \times R_g \\ &= 0.58 \mu m \end{aligned}$$

So, for the whole diameter $2R$,

$$2R = 1.16 \mu m. \tag{3.2.3}$$

By looking at the result displayed in Eq.(3.2.3), we can see that the findings are 84% accurate in comparison to the manufacturer's worksheet as displayed in the table (3.1), which is logical where Mie's method is more accurate for larger particles.

■ Latex particle of size $0.5 \mu m$

From this plot in Fig.(3.4), the same calculations that were done for $1\&2 \mu m$, were made for the $0.5 \mu m$ as follows:

$$Slope = \frac{R_g}{3}$$

So,

$$R_g = \sqrt{3 \times Slope}$$

And from the figure we can see that, $|Slope| = 1.75 \times 10^{-10} cm^2$, so:

$$\begin{aligned} R_g &= \sqrt{3 \times 1.75 \times 10^{-10}} \\ &= 0.229 \mu m \end{aligned}$$

So, R is equal :

$$\begin{aligned} R &= \sqrt{\frac{5}{3}} \times R_g \\ &= 0.2958 \mu m \end{aligned}$$

So, for the whole diameter $2R$,

$$2R = 0.59 \mu m \tag{3.2.4}$$

For $0.5 \mu m$ particle, which has the result as shown in Eq.(3.2.4), that the findings are 82% accurate in comparison to the manufacturer's worksheet as displayed in the table (3.1).

Table 3.1: Here are the 2, 1, and 0.5 μm latex spheres sizes that were resumed by using Mie's method. As it can be seen that Mie's method is more accurate for large sizes comparing to the smaller ones.

Sample	Nominal Size	Measured Size \pm
1	2 μm	2.1 \pm 5% μm
2	1 μm	1.16 \pm 16% μm
3	0.5 μm	0.59 \pm 18% μm

3.2.2.2 Fractal Dimension Test

From Figs.(3.5,3.6, 3.7), it can be noticed that the curves are overlap with each others for different times of events for each latex particles. Moreover, it can also be noticed that for small particles, such as the 0.5 μm , the shape of the curves of $\log_{10}(I)$ versus $\log_{10}(q)$ are more linear than that of the bigger ones. Thus is an opposite case to that of Mie concept in calculating the radius of gyration [§]. Also, it is easy to notice the curves for different times are overlapped on each other, which implies that the shapes of latex particles do not change with time.

[§]In Mie-calculation, the phenomena is more clear and more accurate in calculations.

3.2.3 Dynamics Light Scattering Measurements

3.2.3.1 Studying The Root Square Difference

This technique was achieved by using the OAP program, check section (2.5.2) "DIV" key. The benefit of this technique was to check the dynamic trend of the samples.

This program was used to subtract the intensity of each image from the start image intensity¶The results were represented in two columns, which the 1st column was the time of the subtracted image and the second one was the Root Square Difference "R_Sq_Diff" of the intensities.

- R_Sq_Diff for latex particles
 - Latex particles of size $2\mu\text{m}$

By looking at Fig.(3.9), it can be seen that the difference in intensity between the first image and the rest of images becomes larger and larger with time for different q's. This means that the correlation between the first events and the later ones are no more present.

It is obviously seen that in Fig.(3.10) is the same as plot in Fig(3.9), but for specific $q = 3600 \text{ cm}^{-1}$, chosen such that it correlates to the size of $2\mu\text{m}$ ¶.

¶Could be the first image, the tenth one or the 100th based on the way of analysis.

¶For accurate calculations for single q's, it is recommended for q to be chosen under the constraint of $q \times R < 1$ where R is the radius of particle.

3.2.3.2 Sedimentation process

Since the scattering intensity of particles in solution is proportional to the concentration of the sample [54], it can be concluded that the drop in intensity for long time periods occur, from a decrease in concentration from settling, since shrinkage of the particles is impossible in this experiment [73]. As a result, it was not difficult to calculate the rate of the sedimentation, which is $2\mu\text{m}$ as shown in Fig.(3.14)

Chapter 4

VIRUS INFECTED BACTERIA

After the successful testing of this technique **ARGOS** with known samples that were either static or dynamics, as well as the samples of the previous sections, the next step was to use this technique in studying biological samples, where ARGOS was very flexible to be adjusted with different ways of measurements and analysis.

All biological samples such as bacteria, viruses, and biofilms have been studied since the invention of the convex lens and microscopes (up to the most advanced microscope). These studies have covered many sides of these kind of samples, such as size, shape, reproduction, environment changes, fate, and a long list.

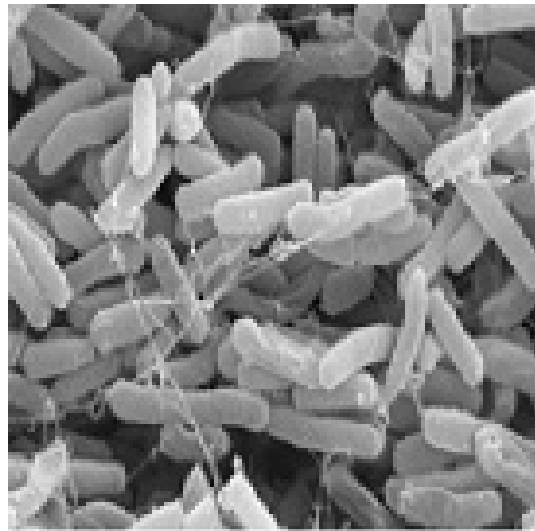
Current studies have been more focused in concentration analysis and fate (life cycle) by using either static or dynamics light scattering. Life cycle of bacteria, for example *E. Coli* can be used as a marker for water quality which is one of the popular studies nowadays either for pure science or public health. This kind of bacteria was the target of this work's study.

4.1 Bacteria and Virus Background

•Escherichia Coli and FAMP

The bacteria *Escherichia coli* (*E. coli*) are coliforms 0.5 to 2.0 μ m in size Fig.(4.1). This bacteria usually live in the healthy intestines of people and animals. The majority of this kind of bacteria are either safe and harmless to humankind, or may cause brief diarrhea. Diarrhea is most probable to *E. Coli* in contaminated water or in the food such as raw vegetables or mild cooked meat.

E. coli, is an easy sample to be tested in labs, and the equipment which is needed for this type of test are available and cheap. Moreover, *E. coli* is quick (life cycle is short relatively to other bacteria), and it is one of the approved tool which US government has been using for water quality check.



FAMP is a genetically engineered *E. Coli* which is only infected by F-specific-coliphages viruses [75, 76].

Figure 4.1: *Escherichia Coli* (*E. coli*) bacteria. [74]

MS2 is a type of F-specific-coliphages, where *E. Coli* is a host for this type of virus.

As it can be seen in Fig.(4.2), the life cycle of bacteria consists of four stages (phases). These phases are listed as follows:

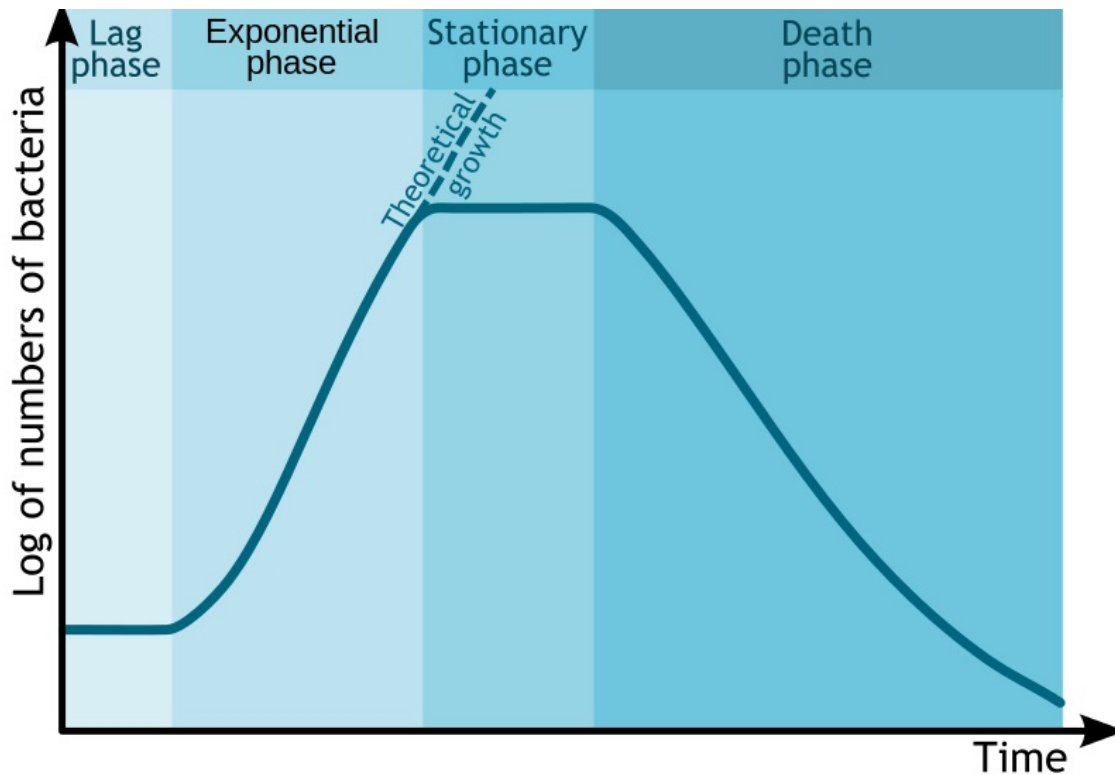


Figure 4.2: *The life cycle of bacteria, where this scheme shows the laboratories observation for the four life-cycle stages, as well as, the theoretical life-cycle which is marked with a dashed line. [77]*

Lag Phase, after the bacteria were introduced to a new environment, the bacteria have to metabolically build up to prepare for the division process.

Exponential Phase, at ideal condition bacteria cells start division process at the highest rate possible based on some parameters, such as, the media environment temperature, and the abundance of food.

Stationary Phase, where bacteria in this phase lose their optimal activity, where the total bacteria number stays about the same.

Death Phase, where the death process in bacteria starts faster and more active than the division process. This is mostly due to lack of food and also because the

new generation becomes weaker in comparison to the parents generations. [77]

The good of *E. coli* biology is the nature of its cell cycle, where *E. coli* is an ideal and simple system because of its ease to grow and manipulate. On the other hand the understanding of this bacteria's regulation is incomplete. [78]

4.2 Results

The sample of the FAMP and the MS2 to be used in this work was prepared as shown in Appendix (B.4)*, where 3 mL of FAMP were prepared for 8.9 mL PBS, 1.0 mL FAMP, and 0.1 mL Strep Amp in phage PBS. This sample was placed in a 10 x 10mm cuvette at a temperature of $30 \pm 1^\circ\text{C}$, and exposed to the laser for 48 hours.

4.2.1 FAMP Characteristics

After the images were analyzed using the same method as the previous section, a graph of the total intensity versus time was plotted as shown in Fig.(4.3). From Fig.(4.3) it can be seen that the growth phase started at almost 0.3 hour. It is also apparent in this figure that the stationary phase has two peaks. One at 1.8 hour and the second at 27 hours, also the curve has a valley at 7 hours.

It can also be seen in Fig.(4.4), where Root Square Difference of $\langle I \rangle$ was plotted versus time for the same FAMP sample for different q 's , that smaller q represents more details of the scatterers behavior.

*This sample was prepared in Civil and Environmental Engineering department by A. Charest.

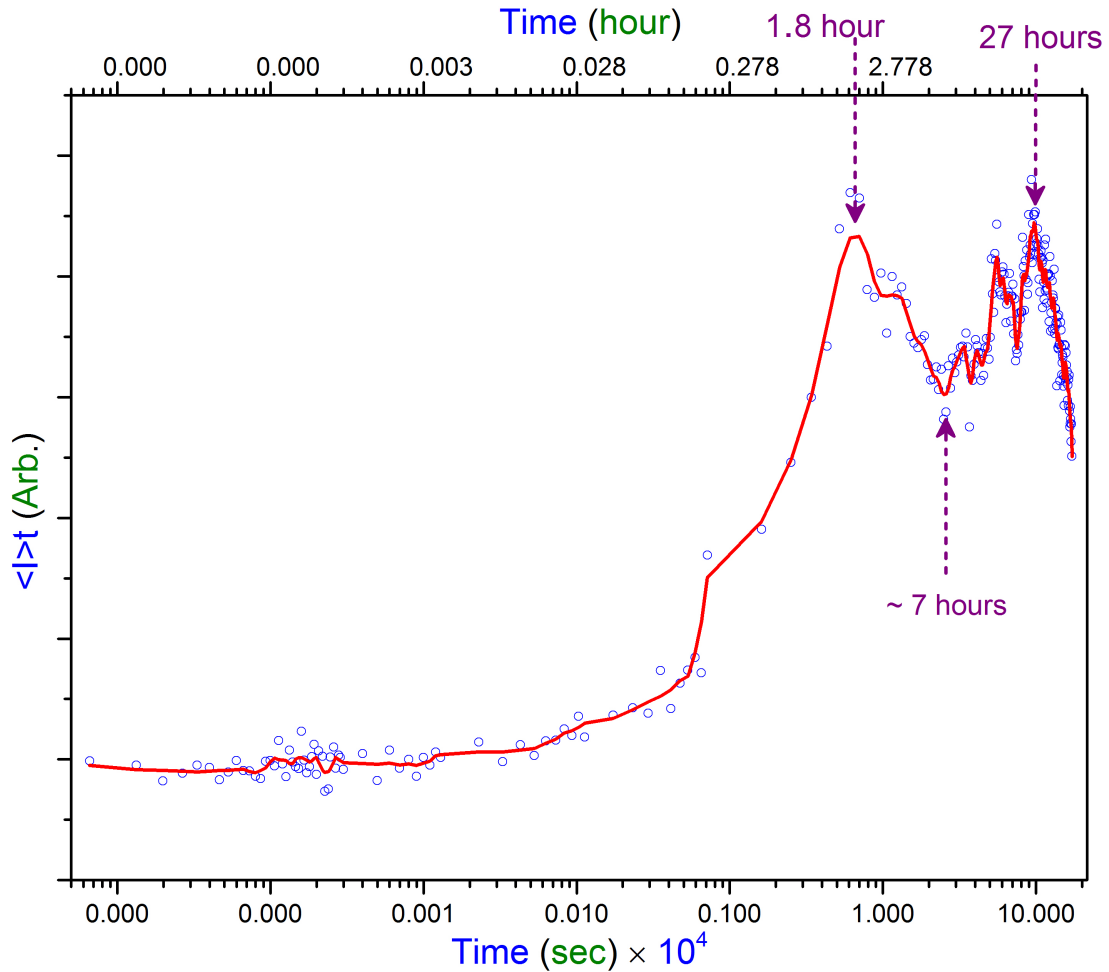


Figure 4.3: *This figure shows the trend of intensity for the FAMP which was prepared of 8.9 mL PBS, 1.0 mL FAMP, 0.1 mL Strep Amp in phage PBS. The sample placed in 10mm x 10mm cuvette and exposed to the laser for 48 hours, where the temperature of the environment was = 30 ± 1 °C.*

To find the behavior of the bacteria at specific region close to the regime of ($qR \leq 1.0$), a single curve at $q = 3772 \text{ cm}^{-1}$ was picked and plotted as shown in Fig.(4.5). This curve has two peaks at the stationary phase, where the first peak at the time 12.3 hours , while the other one at the time 20.8 hours. The stationary phase did not show a plateau in this test.

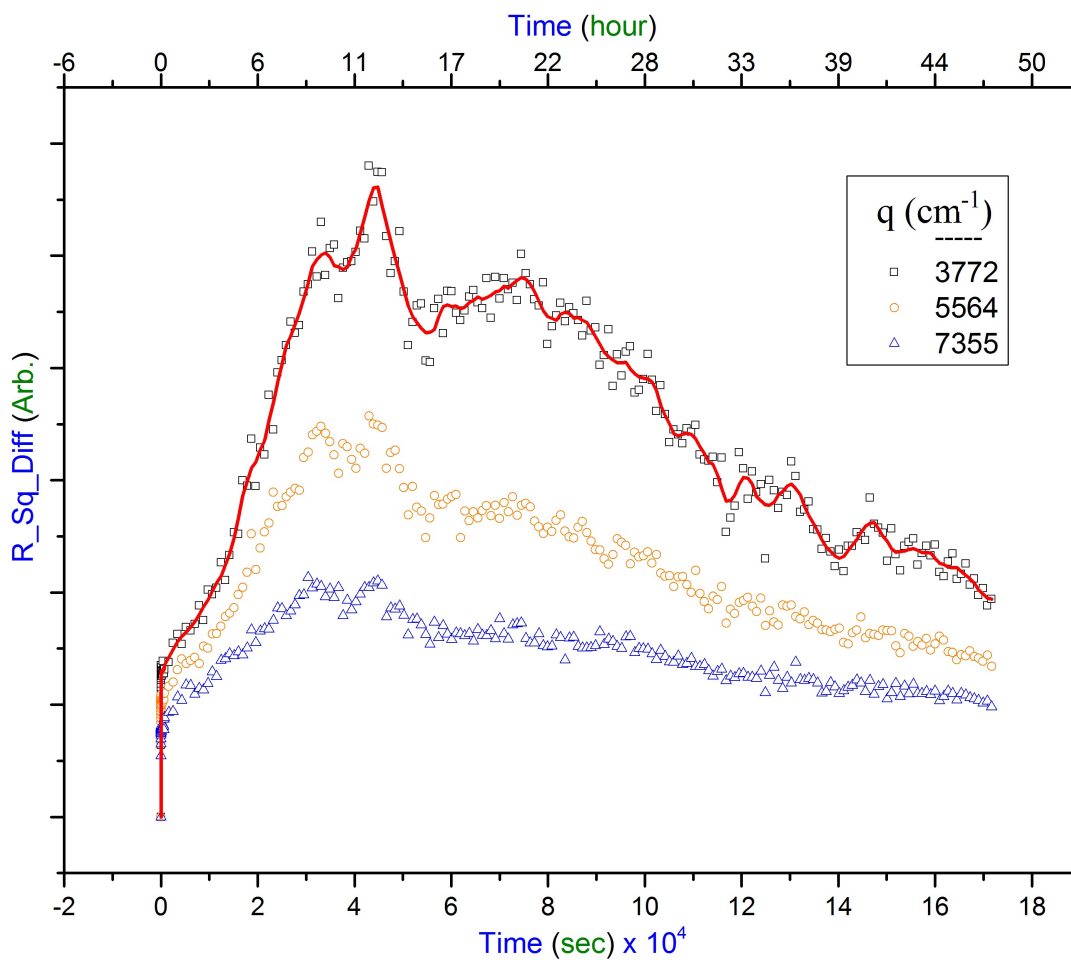


Figure 4.4: This Figure shows the 48 hours life cycle at different q 's for the 3 mL FAMP bacteria at different q 's, where the sample placed in 10 mm x 10 mm cuvette. This sample was prepared of 8.9 mL PBS, 1.0 mL FAMP, 0.1 mL Strep Amp in phage PBS. Environment temperature = 30 ± 1 °C.

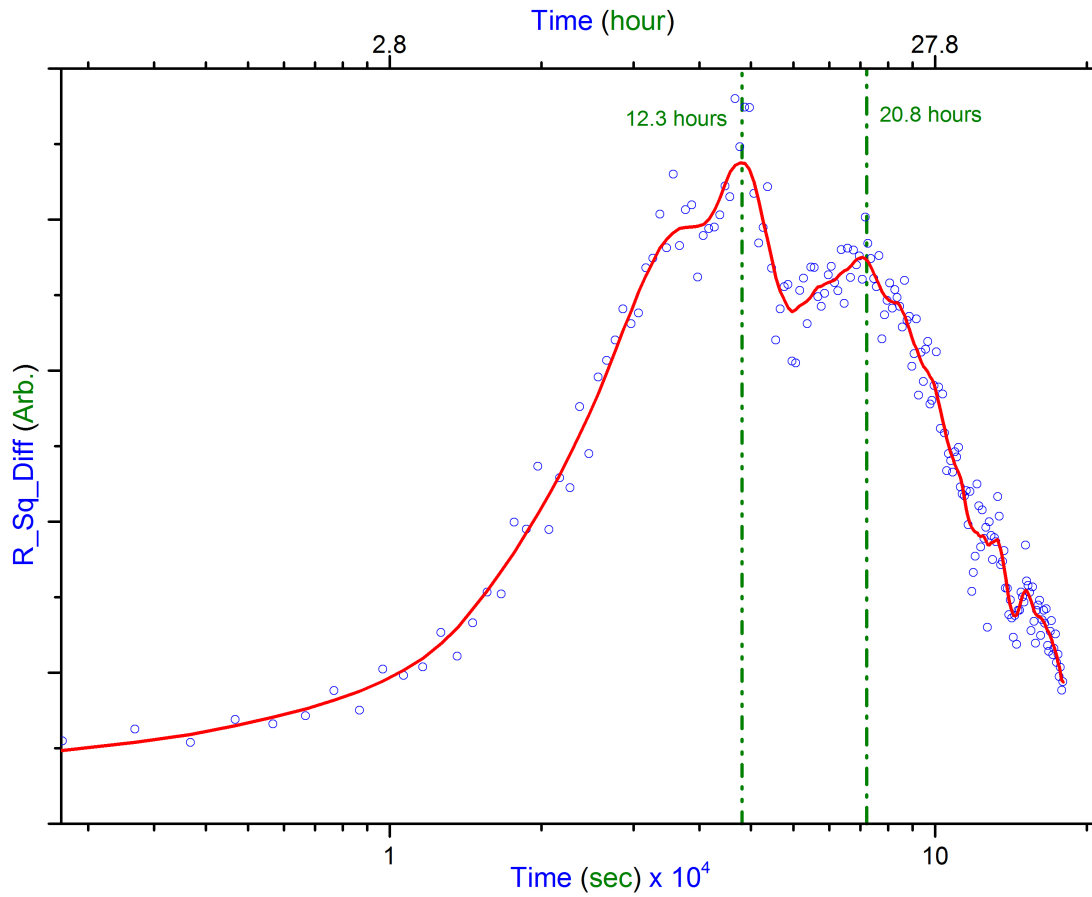


Figure 4.5: This Figure shows the 48 hours life cycle for a 3 mL of FAMP bacteria at $q=3771.9$. The sample was prepared of 8.9 mL PBS, 1.0 mL FAMP, 0.1 mL Strep Amp in phage PBS and placed in 3.5 mL cuvette. Temperature = 30 ± 1 °C. For this q regime $q=3772 \text{ cm}^{-1}$, there are two peaks at 12.3 hours and 20.8 hours, check Fig.(4.2).

4.2.2 Topology of the FAMP

To study the topology of the bacteria during the life cycle, a plot of $\log_{10}(I)$ vs $\log_{10}(q)$ for different times were done in Fig.(4.6) check section (1.2.3). In this figure the curve started with smallest slope value, then it became larger with time until it reached its maximum at $t= 12.75$ hours, then it came back down gradually, close to that of the start of the curve. The vertical dashed line was chosen at $q = 4 \times 10^4$ which correlated to the size of the *E. Coli* $\sim 2\mu\text{m}$ [79, 80].

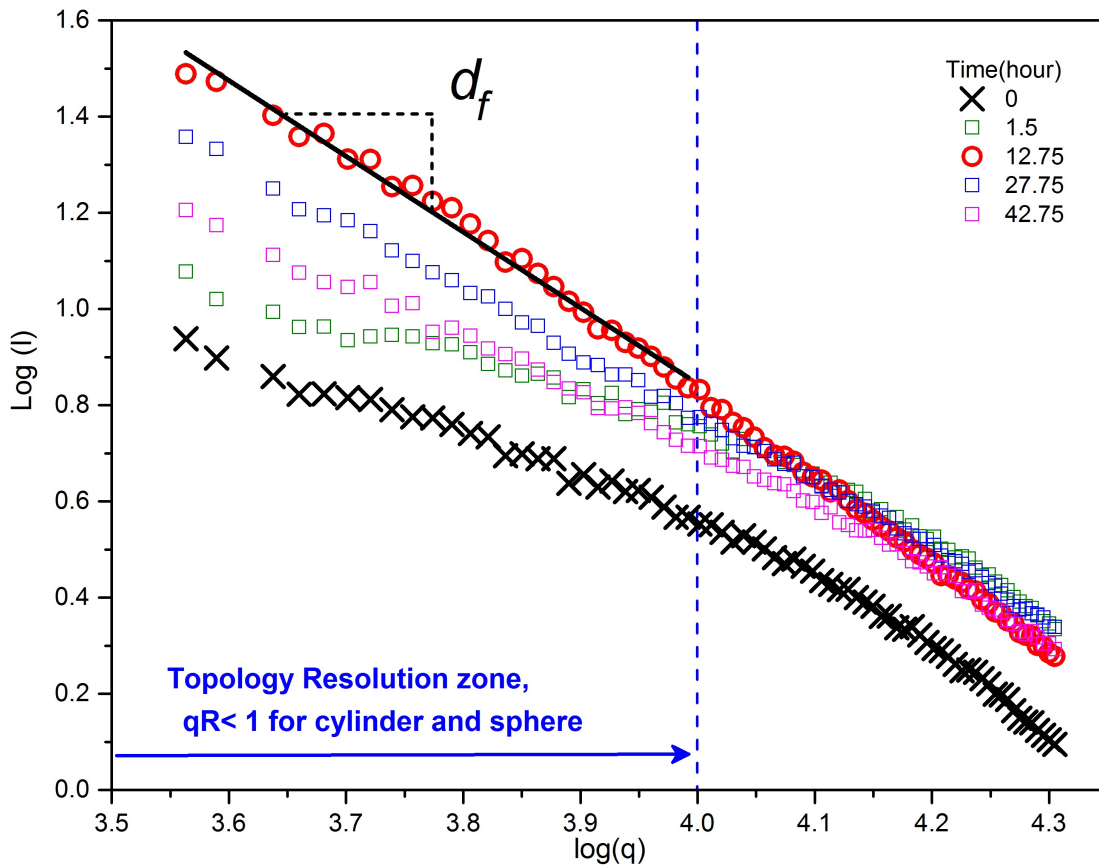


Figure 4.6: The 48 hours life cycle for the FAMP bacteria which are the same bacteria which are the same bacteria in Fig.(4.5), where each curve represents the time of event and it is easy to note that the shape of the bacteria is changing with time during the life cycle.

In Fig(4.6), some of the times' curves were picked to show the actual trend of the

curves at different times, these curves were chosen based on the most beginning time, also the highest slope curved was chosen, moreover, the most last curve with a lower slope was chosen too.

4.2.3 Fractal Dimension of the FAMP

To find the fractal dimension " d_f " for The FAMP, The Eq.(1.2.64) is used for this purpose. The plot of Fractal Dimension versus Time was plotted in Fig.(4.7).

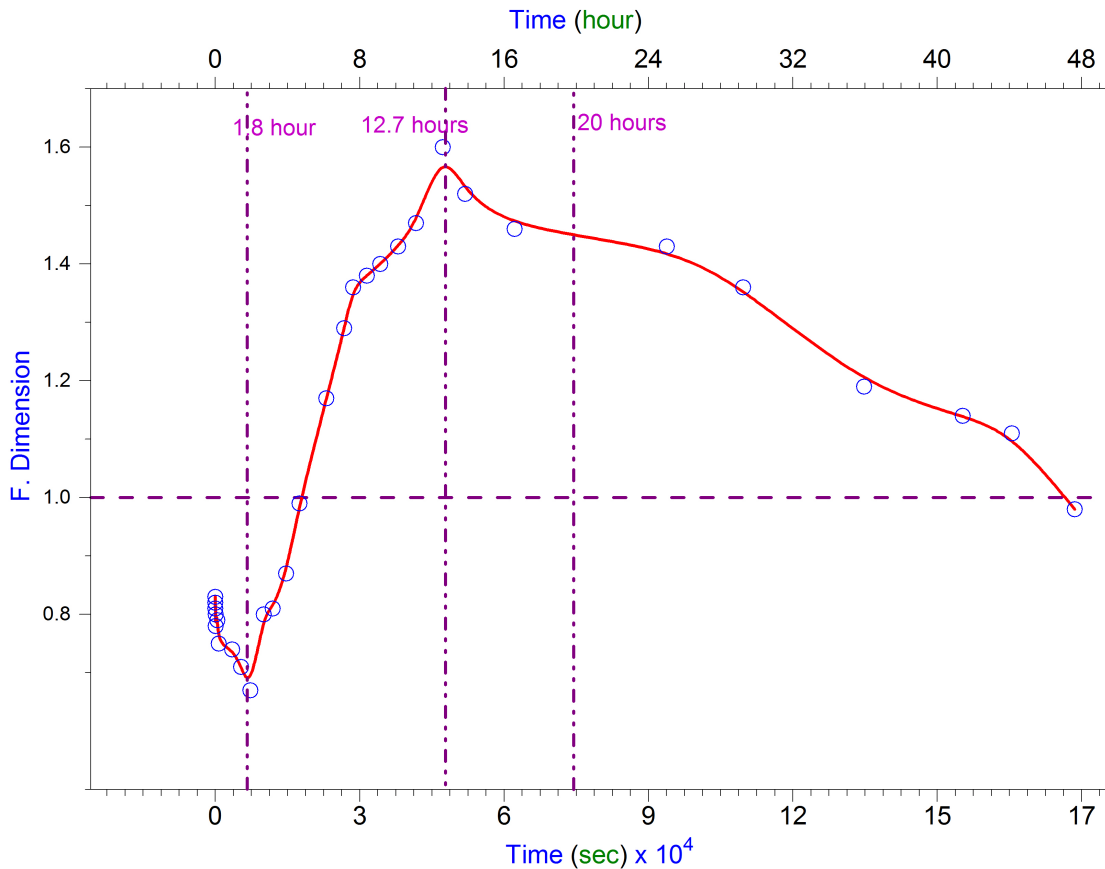


Figure 4.7: This figure is describing the change of Fractal Dimension correlated the time for the FAMP, where the peak of this curve appeared at the time of 12 hours.

Where as the curve shows a decrease in the value of Fractal Dimension at the

beginning, it increases with time until it reaches its maximum at ~ 12 hours, then it decreases gradually until near the end of the experiment run time.

4.2.4 Effective Radius

In this part of experiments analysis, calculations of the size of particles were found based in the usage of the Mie calculation method. So $\ln(I)$ versus q^2 at different times . See Fig.(4.8).

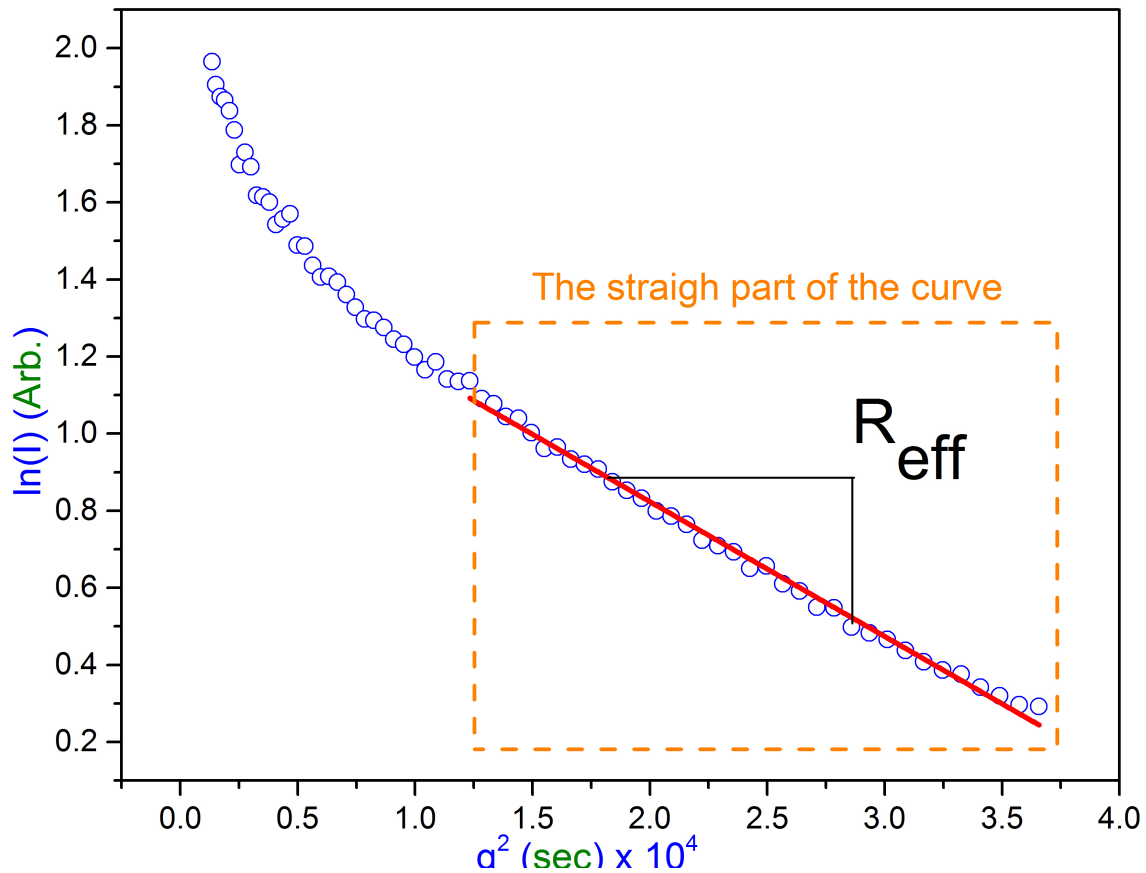


Figure 4.8: This figure shows the method of finding the Effective Radius " R_{eff} " by using Guinir's method. See page (3.1.2.1).

The slope of each line represents the radius of the bacteria, check section (3.1.2.1)

for more details about this calculations. From plotting effective radius " R_{eff} " versus time is shown in Fig.(4.9), it is clear that the curve in this figure went gradually down until it reached low value at a time ~ 2 hours, then the size of the bacteria increased to reach its maximum at 9 hours, finally the curve went back again to the minimum at the end of the experiment's time.

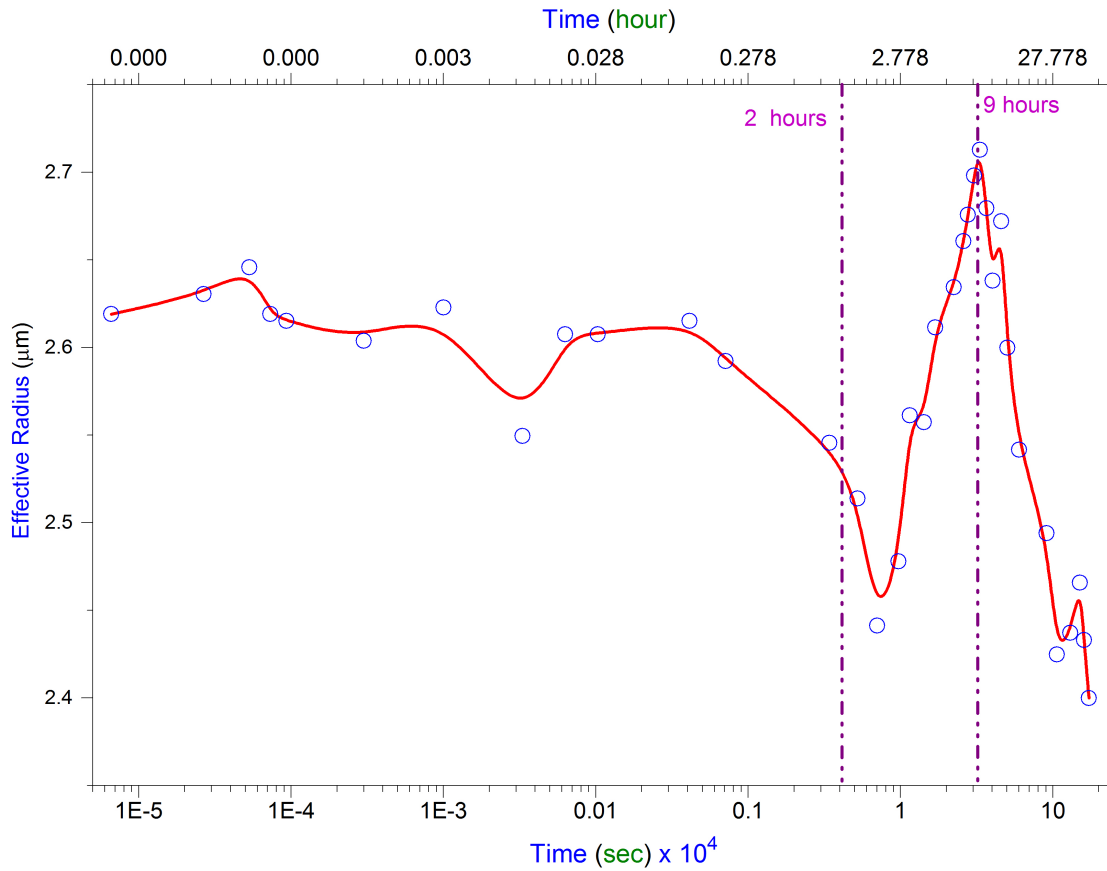


Figure 4.9: This figure is describing the change of FAMP size versus the time, where the peak of this curve appeared at the time of 9 hours. The Famp in this figure is the same bacteria which was used for the whole experiment from the prospect of the concentration and the preparation of the sample. The temperature for this run was 25 ± 1 °C.

4.2.5 Four Panels Chart

In Fig.(4.10) there are four panels, where each of them describes a characteristic that was studied in this work. In panel (a) the total scattered intensity from the FAMP is plotted versus the time. In panel (b), the Root Square Difference versus time is plotted, and in panel (c) the plot of Fractal Dimension versus time is shown. Finally in panel (d) is the plot of Effective Radius versus time is depicted. In this figure the Root Square Difference was chosen to be the reference for the reset of panels, so that the vertical dashed line is passing through the peak of the Root Square Difference.

As seen in Fig.(4.10), the first peak of the growth phase in panel (a) overlapped with the minimum Fractal Dimension in panel (c) as well as the first trough for the R_{eff} in panel (d).

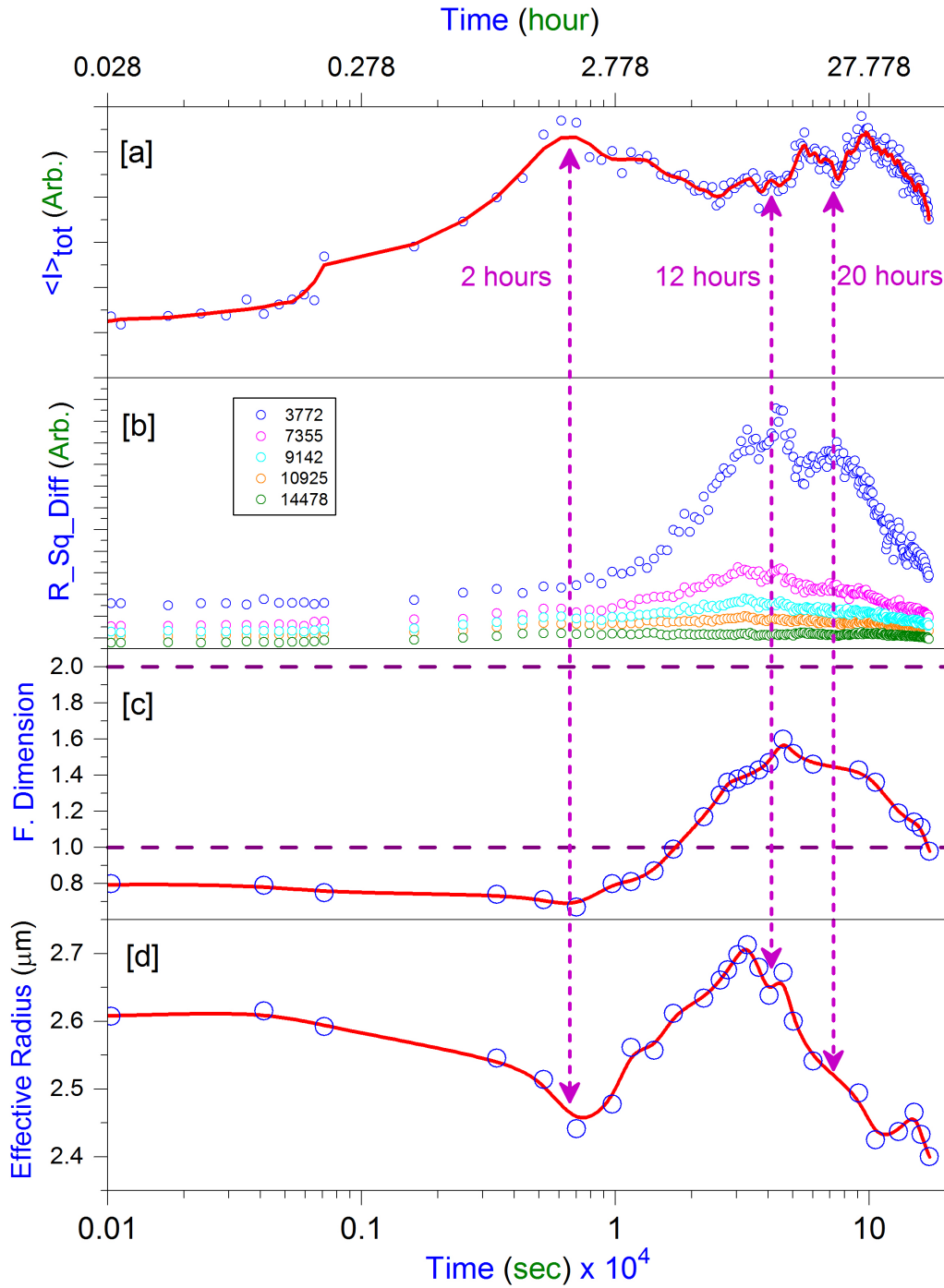


Figure 4.10: This figure summarizes the four characteristics that have been discussed for the FAMP in this work. Panel (a) shows the total scattered intensity from the bacteria during the 48 hours, and panel (b) is an indication tool to the dynamics of the FAMP during the life cycle. Panel (c) describes the trend of the Fractal Dimension. And finally the panel (d) shows the change of the Effective Radius during the life cycle of the FAMP.

4.2.6 Effect of Temperature change on FAMP

In this part, the same procedure was done for the same sample which illustrated in Fig.(4.5), but for different temperatures of around $20\pm 1^\circ\text{C}$, check Fig.(4.11) for X-linear scale and Fig.(4.12) for X-logarithm scale. By comparing these two plots, of the cold sample (upper panel) and the hot sample in the lower panel, one can notice that the growth stage started earlier in the hot sample comparing to the cold one. Also, it can be seen that the end of growth stage for the hot sample occurred after ~ 8 hours, while for the cold sample, the growth stage kept going until ~ 40 hours.

By looking at the cold sample (upper panel), it can be noticed that the trend of the growth phase took the shape of sinusoidal function shape. It can also be noticed from the caption of this figure, that two time-intervals were applied during this experiment's run. The purpose of the lower temperature ($20 \pm 1^\circ\text{C}$) run was to slow the FAMP life-cycle's process. Moreover, images of a 30 second-interval were shot during the period of 7-25 hours, which is denoted on the figure as "Short Intervals zone". In this zone the sinusoidal behavior of the bacteria during the growth phase can be seen.

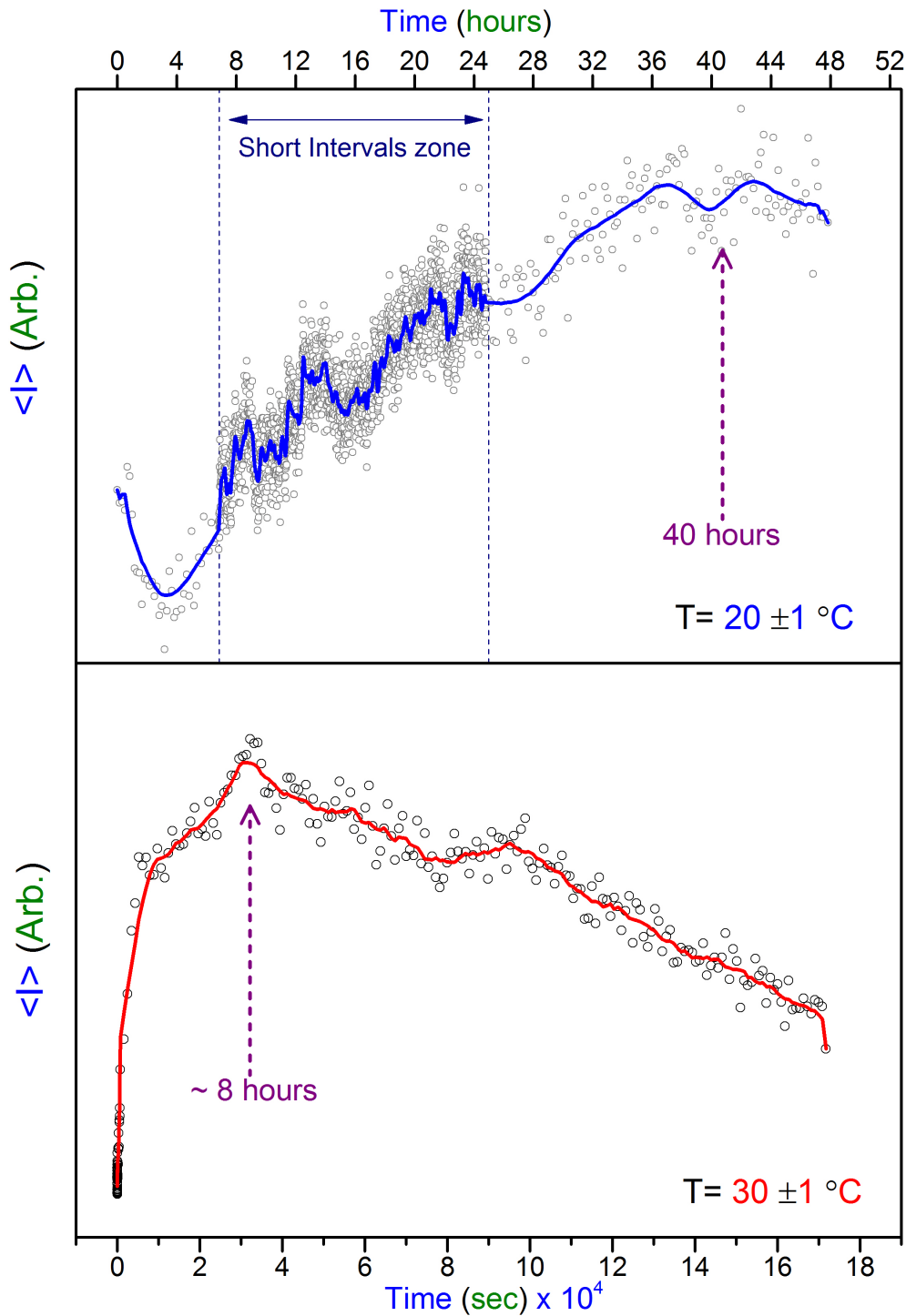


Figure 4.11: This Figure shows the 48 hours life cycle for the 3 mL FAMP bacteria. Sample's temperature was $20 \pm 1 \text{ } ^\circ\text{C}$ for the upper panel while it was $30 \pm 1 \text{ } ^\circ\text{C}$ for the lower panel. For the lower temperature sample (upper panel), two settings of time interval between images were applied, first setting was 10-minuets intervals which are located before the first vertical line and after the second dashed one, while the short interval setting was 30 seconds which is located between the two vertical lines as shown in the plot.

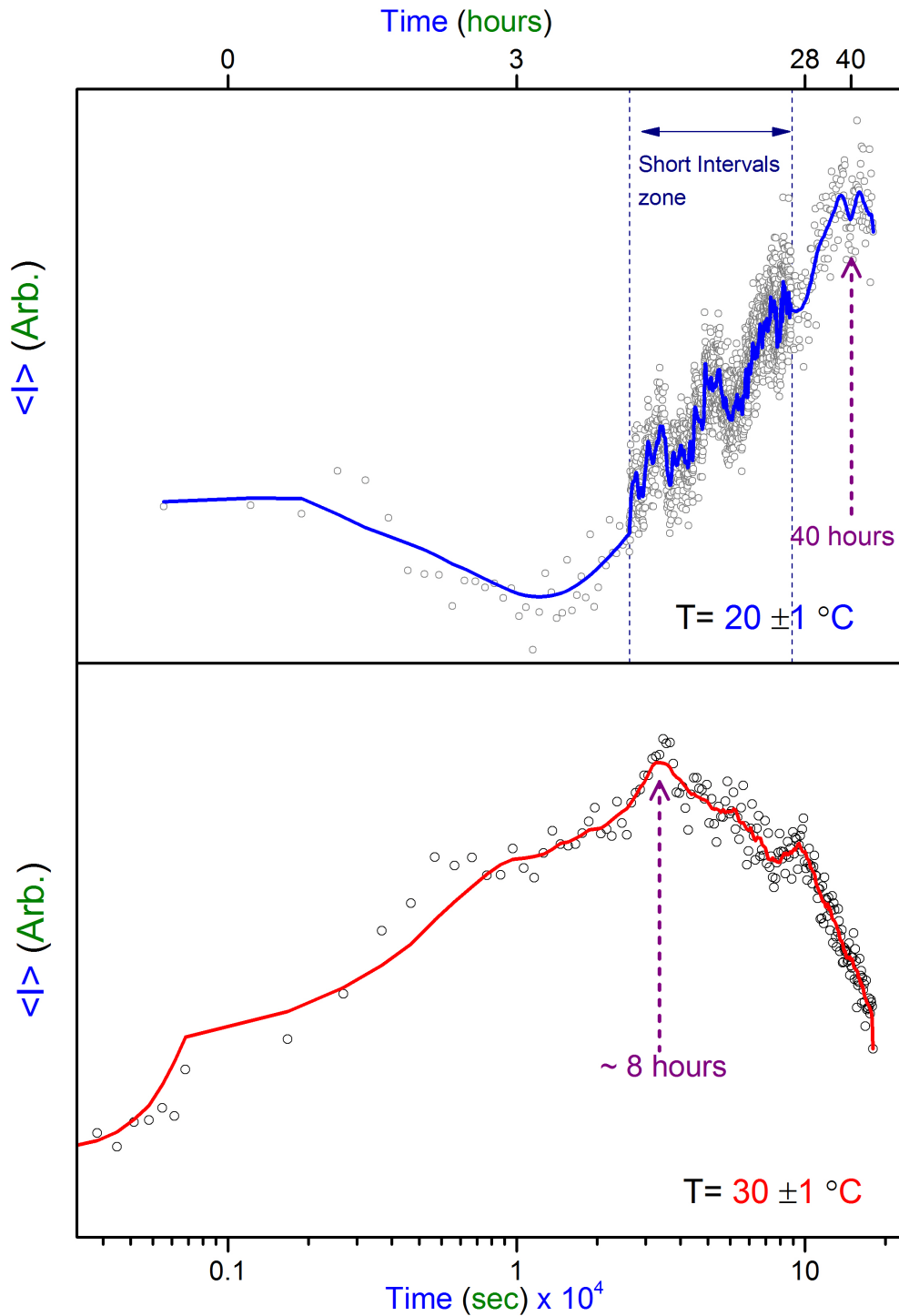


Figure 4.12: This Figure shows the 48 hours life cycle for the 3 mL FAMP bacteria in cuvette which was prepared of 8.9 mL PBS, 1.0 mL Famp, 0.1 mL Strep Amp in phage PBS. Temperature = $20 \pm 1 \text{ } ^\circ\text{C}$, the sample placed at 18 cm from the screen. Two settings of time interval between images, 10-minuets intervals which are located before the first vertical line and after the second dashed line, while the short interval setting was 30 seconds which is located between the two vertical lines as shown in the plot.

4.2.7 FAMP with MS2-Infection Characteristics

The same procedures as done in the FAMP's sample was applied for this part (FAMP-infection) with regards to the collection of data and the analysis. The total intensity versus time was plotted in Fig.(4.13) in two flavors of panel(a) and panel (b). The purpose of these two plots is to show the whole picture of the sample's dynamics before the peak and after the peak of the curve. If the plot was made only on the X-linear scale as in panel (b), one wouldn't have been able to see the fast dynamics which occurred at the very beginning of the experiment's run. On the other hand, if the plot was made only on the X-logarithm scale, as in panel(a), the data on the right side of the peak would have been squeezed together because of the logarithm's characteristics.

As it can be seen in panel(a) of Fig.(4.13), the intensity of the bacteria started constant horizontally until it reached the time ~ 0.3 hour, then it increased gradually until the curve reached its maximum at the time 2 hours. In panel (b), after the curve reached its maximum at 2 hours, it dropped down sharply until the time 12 hours, then the intensity of the curve's decline became less with time.

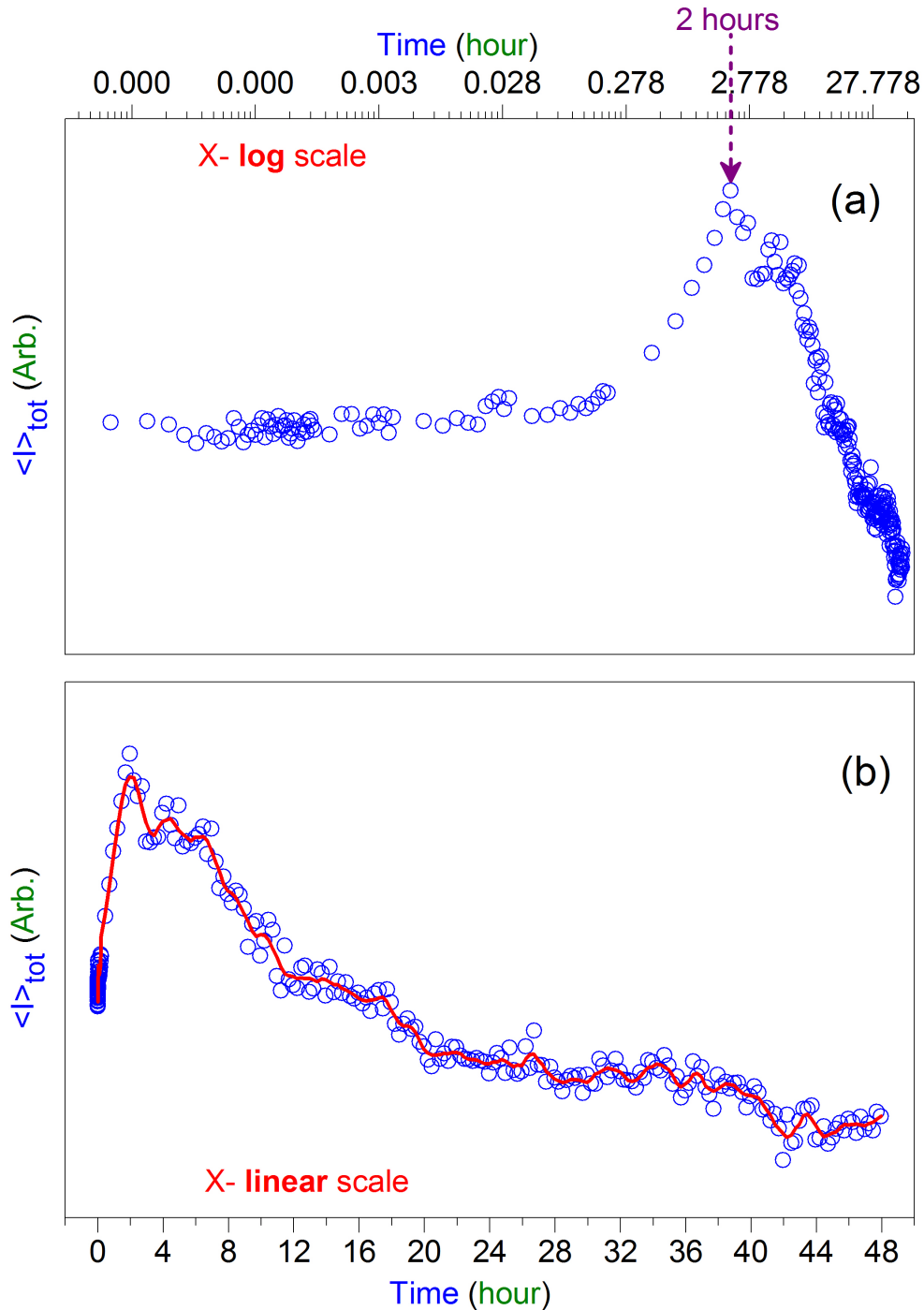


Figure 4.13: This figure shows the relation between the total intensity of FAMP after it has been infected by MS2 virus. The sample characteristics are the same as that used in the FAMP section, where the sample was exposed to the laser for 48 hours. There are two panels in this figure based on X-scale configuration. Panel (a) is X-logarithm scale which shows the dynamics of the FAMP at the beginning short intervals, while panel (b) is X-linear scale which can show clearly the curve trend after the peak which was at 2 hours.

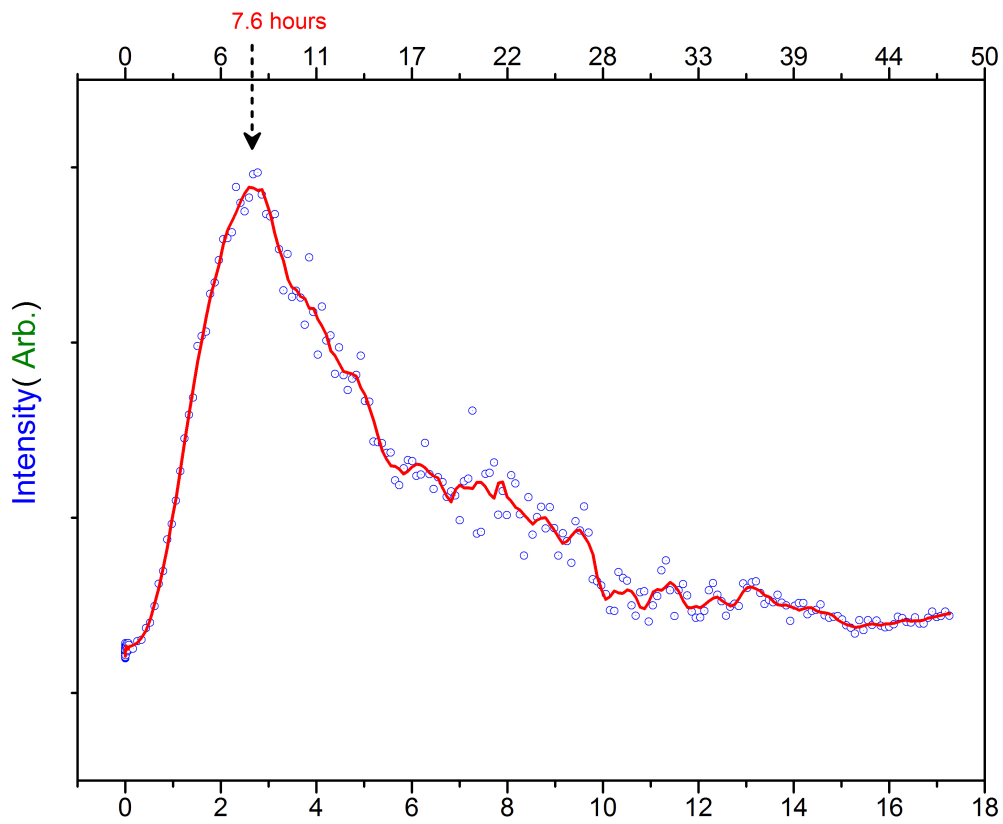


Figure 4.14: This figure shows the plot of average intensity versus time for the FAMP after infected with virus MS2 for $q=3714 \text{ cm}^{-1}$. It can be seen that the peak of the infected bacteria occurred at the time 7.6 hours.

4.2.8 Topology of the FAMP with MS2-Infection

As what was seen in the topology of the FAMP, check page (115), the same procedure is made for the FAMP after it was infected with MS2 virus, hence, the plot $\text{Log}_{10}(I)$ versus $\text{Log}_{10}(q)$ is shown in Fig.(4.15).

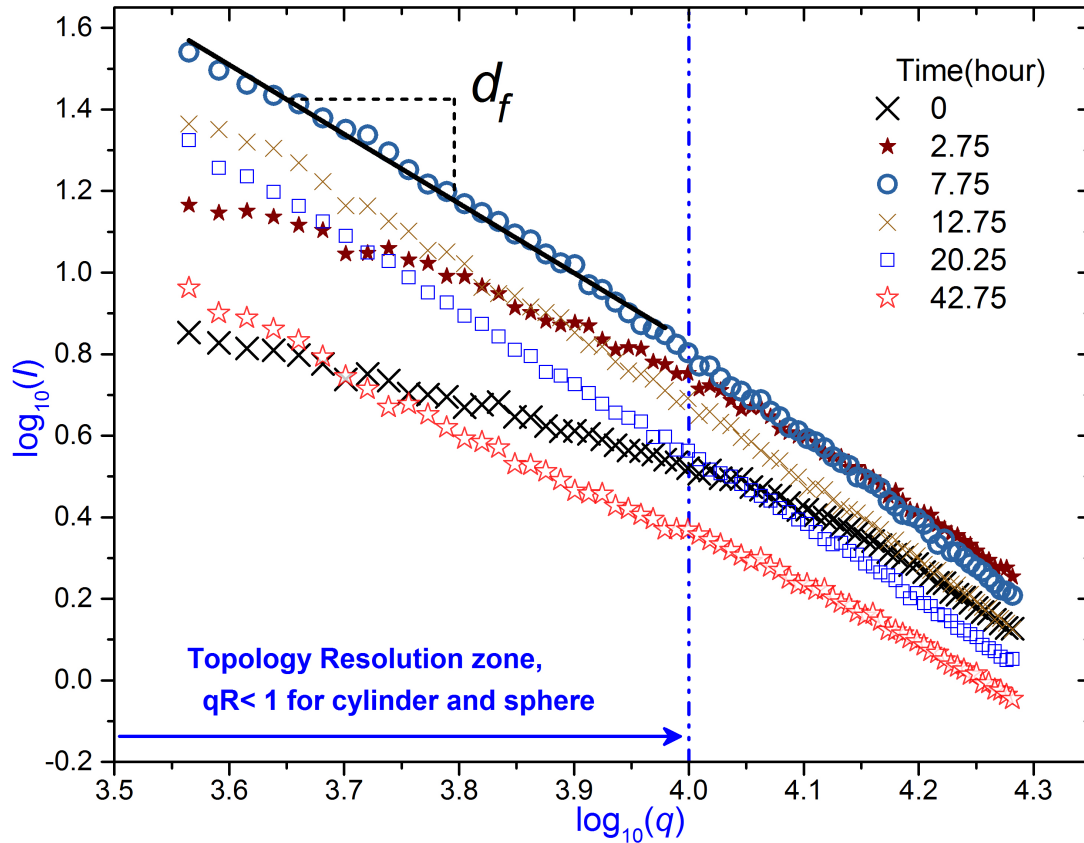


Figure 4.15: In this figure it can be shown different curves for the FAMP after it was infected by MS2 viruses. The most lower curve slope was for the curve at the time = 0 sec, whereas the largest slope curve was for time = 7.75 hours, and the last curve was at the time 42.75 hours. So, each curve represents $\text{Log}_{10}(q)$ vs $\text{Log}_{10}(I)$ at a specific time.

In this figure, it can be seen that the topology of the infected FAMP changes with time, where as one can noticed that the slope of the $\text{Log}_{10}(I)$ - $\text{Log}_{10}(q)$ curve starts rising as time progressed until it reached its maximum at the time 7.75 hours, then it went back gradually after 42.75 hours to almost reached the beginning of the time

axis, which was where the first image's time. This slope, as was mentioned earlier in FAMP topology study, is nothing but the Fractal Dimension d_f .

4.2.9 Fractal Dimension of the FAMP with MS2-Infection

As it was known from the previous result of the FAMP-MS2 topology, the Fractal Dimension " d_f " changes during the FAMP-MS2 life cycle, the same producers which were applied in the FAMP Fractal calculations, check page (116), are the same producers which were applied here to produce this curve as shown in Fig.(4.16).

In Fig.(4.16), the trend of d_f during this time is shown in this figure. After 1.2 hour the curve dropped to the minimum of the value of d_f , then the curve rose up to reach its peak value at the time 9.7 hours, then the curve dropped back gradually to the time ~ 27 hours. The curve then flatlines until the end of the experiment's time.

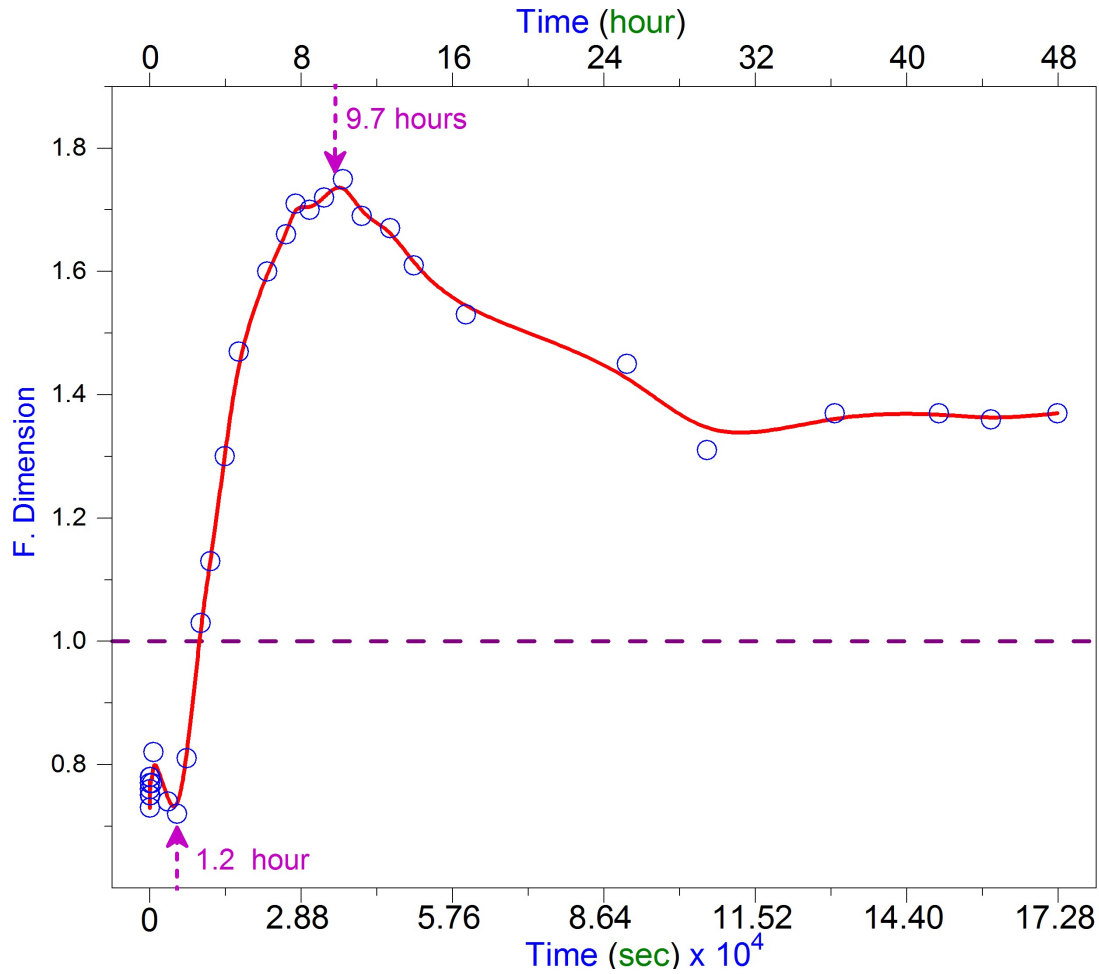


Figure 4.16: This figure shows the trend of the d_f is changing with the time progress. It can be noticed in this figure that the d_f went first down to form a valley after 1.2 hour, then the curve began rising to reach the maximum point at 9.7 hours, then the curve went back down to become horizontal after 27 hours.

4.2.10 Effective Radius of Infected FAMP with MS2 Virus

As previously discussed on FAMP effective Radius, check page (117) , the radius of bacteria was changed after infection with MS2, as seen in Fig.(4.17) where the Effective Radius was plotted versus time. In this figure it can be seen that the curve remained constant at the beginning, then dropped after one hour, then the curve of R_{eff} rose up gradually to the peak at the time 7.5 hours, then dropped down again

to a point lower than that of the first point at the beginning of the experiment's run.

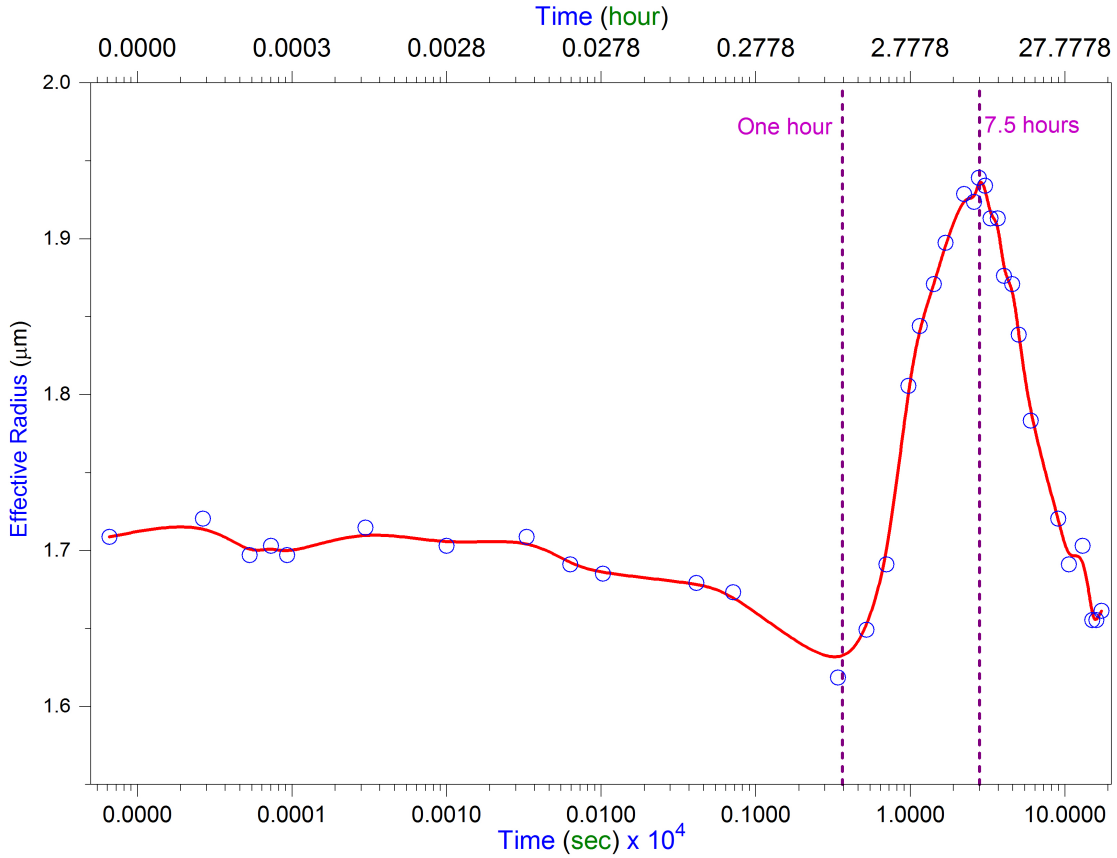


Figure 4.17: This figure shows the a plot of R_{eff} versus time for the FAMP after an infection with MS2 virus. In this plot there is a valley at time one hour, then the curve rose up until it reached a maximum 7.5 hours, then it fell down back to reach a local minimum at the end of the experiment's run.

4.2.11 Four Panels Chart of FAMP with MS2-Infection

Four panels' plot of the FAMP after it was infected with MS2 is shown in Fig.(4.18). In the first panel (a), it can be seen that the relation between the total scattered intensity of the FAMP, after infected with MS2, shows only one peak at 2 hours. In panel (b) five of Root Square Difference where all peaks occur at the time 7 hours.

Panel (c) shows the change of d_f with time, where there is a peak after 7 hours. This is the same as panel (d) with a peak occurring at the 7 hours instead.

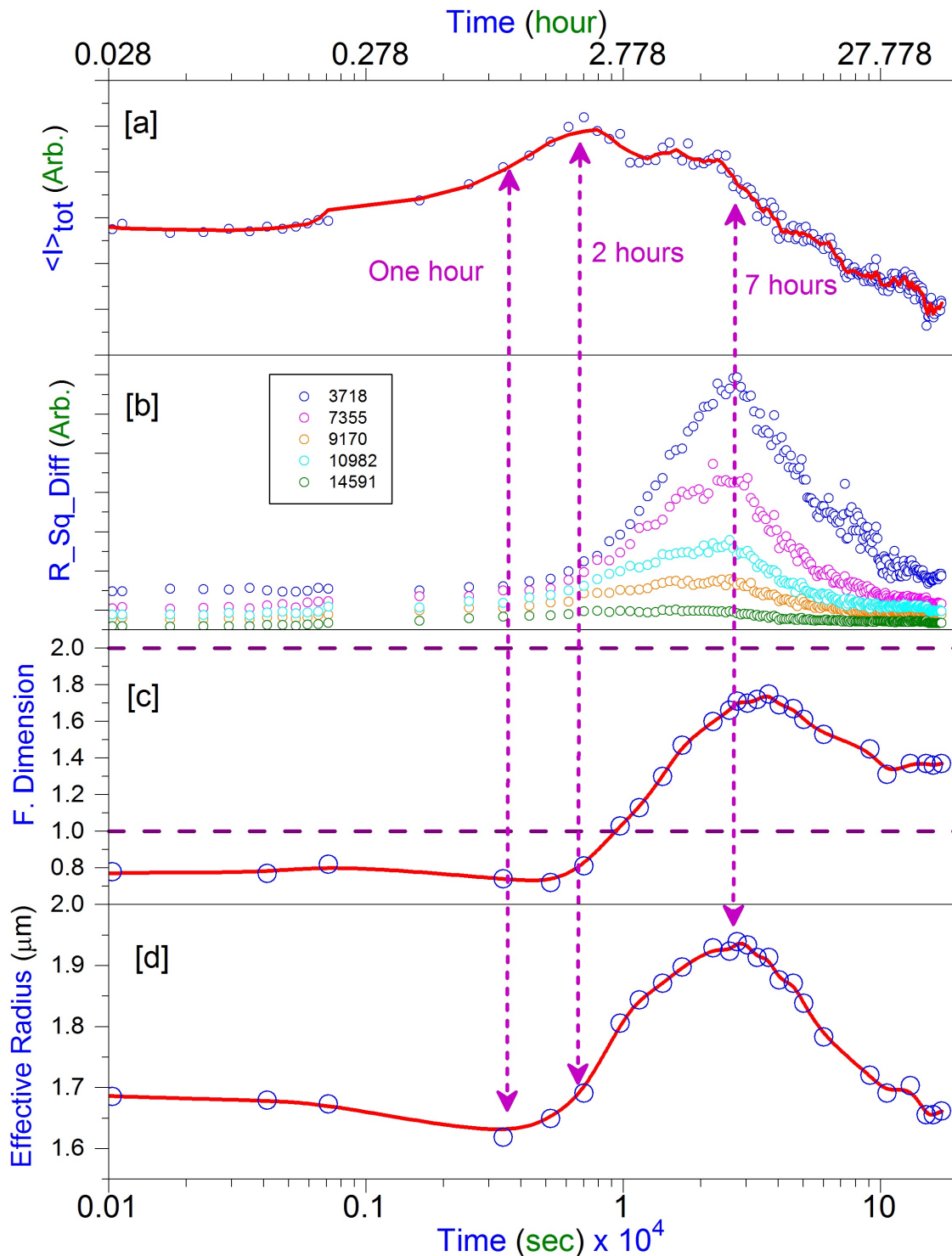


Figure 4.18: This figure summarizes the four characteristics that have been discussed for the FAMP after it was infected with MS2. Panel (a) shows the total scattered intensity from the bacteria with viruses during the 48 hours, and panel (b) is an indication tool to the dynamics of the FAMP-MS2 infection during the life cycle. panel (c) describes the the trend of the Fractal Dimension. And finally the panel (d) shows the change of the Effective Radius during the life cycle of the FAMP with MS2 viruses.

4.2.12 FAMP and FAMP-MS2-infection Gallery

In this part of the work, every two plots similar in characteristics, are merged together in one figure for comparison purposes. For example, in Fig.(4.19) a plot of the average intensity for the FAMP's specimen was only plotted in panel (a) and the same for the infected FAMP in panel (b) for a specific $q = 3714 \text{ cm}^{-1}$. As it can be seen that in FAMP case, there are two peaks in the intensity, the first peak was at the time 12.3 hours, and the second peak was at the time 20 hours, while in infected FAMP in panel (b), there is only one peak at the time 7.6 hours.

It is clear that the increasing or decreasing of the slope for the curves in panel (a) and in panel (b) in Fig.(4.19) are not the same, so, a plot of the same figure is shown again in Fig.(4.20) but on X-linear scale. The slopes of growth phase and death phase were then plotted, as it can be seen in panel (a) for the Famp and in panel (b) for the infected FAMP with MS2 virus. It is easy to see that the growth mounting "m_g" for the infected FAMP in panel (b) is twice as large as the growth mounting for the FAMP only. Also the death decline which notated by "m_d" is faster in the infected FAMP (panel b) when compared to the FAMP only in panel (a).

In Fig.(4.21), there are two panels, panel [a] represents FAMP Fractal Dimension , while panel [b] is the Fractal Dimension for FAMP after infection with MS2 virus. It can be seen that the growth stage's starting point occurs earlier, (1.2 hour) after the infection, than the case before infection (1.8 hour). Also, the peak point of the growth was reached earlier (9.7 hours) in infected sample when compared to the FAMP sample before infection which was at the time 12.7 hours. Also it can be seen that the deformation in the shape of the bacteria after infection came closer to the spherical shape more than the case before infection. Moreover, the deformation of

the shape before infection progressed towards the original shape (rod shape), thought this is not the true for the sample after infection, where the shape of bacteria stayed closer to the peak of deformation.

The last figure is Fig.(4.22), compares the size of bacteria (FAMP) radius before infection with MS2, as shown in the lower panel (a) and after the infection as shown in the upper panel (b). It can be easily noticed that the Change in the bacteria's radius started earlier after the infection with MS2 in comparison to the same case before infection. Moreover, the size of bacteria at the peak is bigger before infection with MS2 viruses when comparing the size for the same situation after infection. Also , three dashed horizontal lines were drawn on each panel, at the lower size, the lag phase (the middle line) and at the highest size.

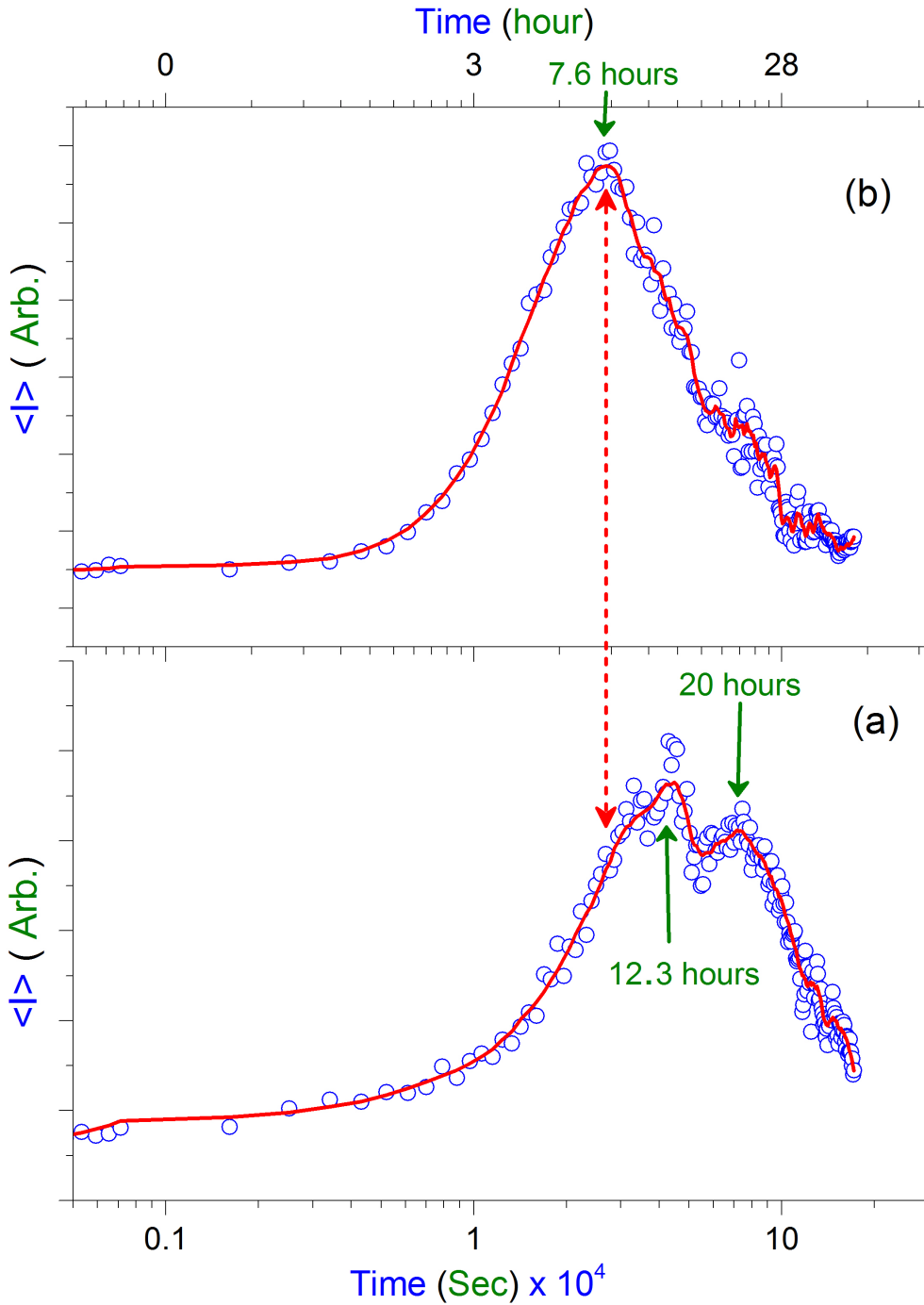


Figure 4.19: This Figure represents the behavior of the FAMP bacteria prior to infection by MS2 as in panel(a). Moreover, in panel (b) it can be seen the behavior after infection. Both sample for the same $q=3714 \text{ cm}^{-1}$. Moreover, it can be noticed that the end of growth phase ended for the infected FAMP before it occurred in the FAMP before the infection with around 5 hours difference.

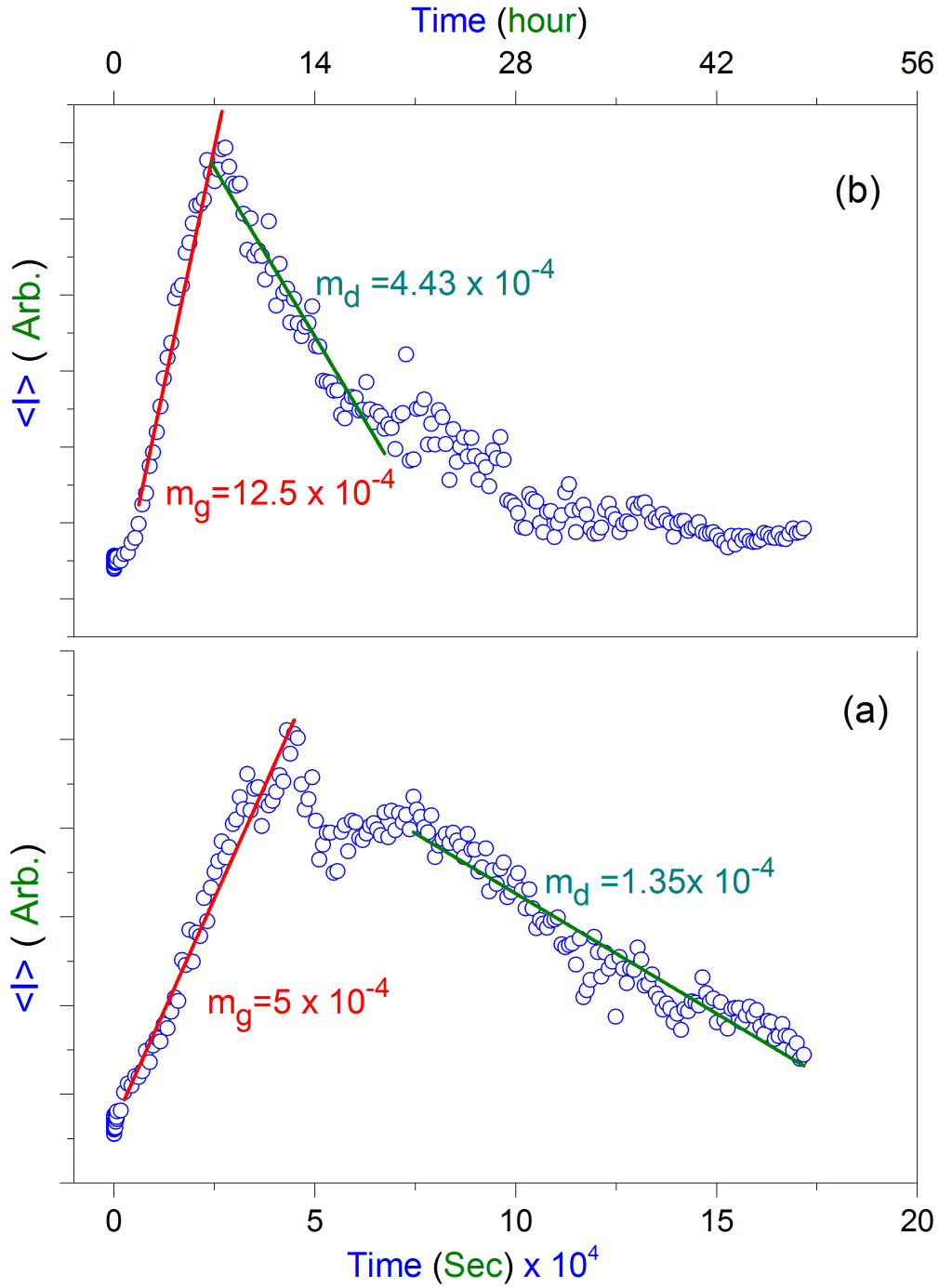


Figure 4.20: The growth rise and the death slope for the FAMP prior infection by MS2 as it can be seen in panel (a). Also in panel(b), this figure shows the same slopes after the infection by MS2 . Both sample for the same $q = 3714 \text{ cm}^{-1}$.

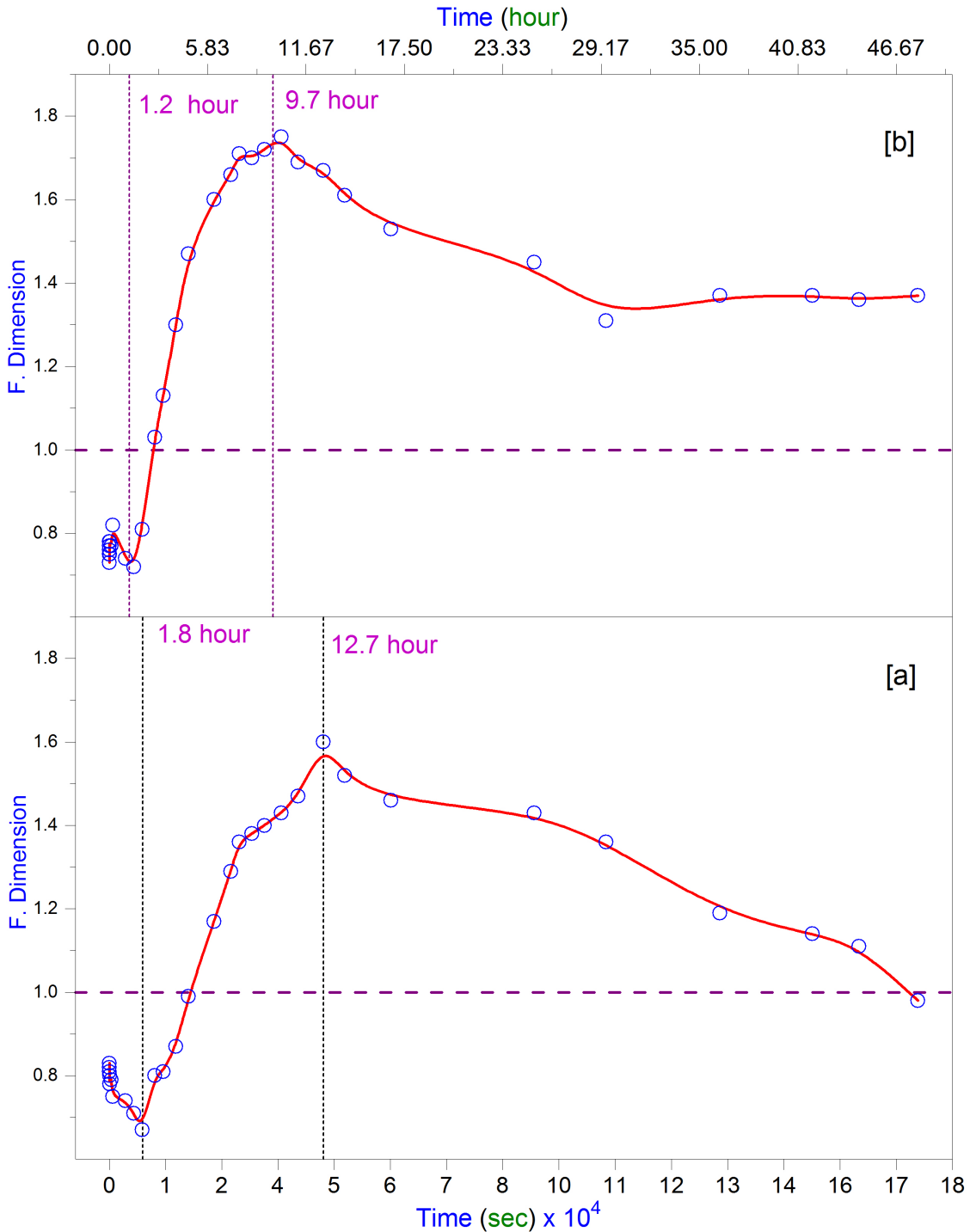


Figure 4.21: This figure shows the FAMP's d_f in panel (a) and the FAMP with MS2 infection in panel (b). The minimum point of d_f for FAMP is at 1.8 hour, while the minimum point for the infected FAMP is at point 1.2 hour. Also, the peak for the FAMP was at time 12.7 hours, while the peak for the infected FAMP was at 9.7 hours.

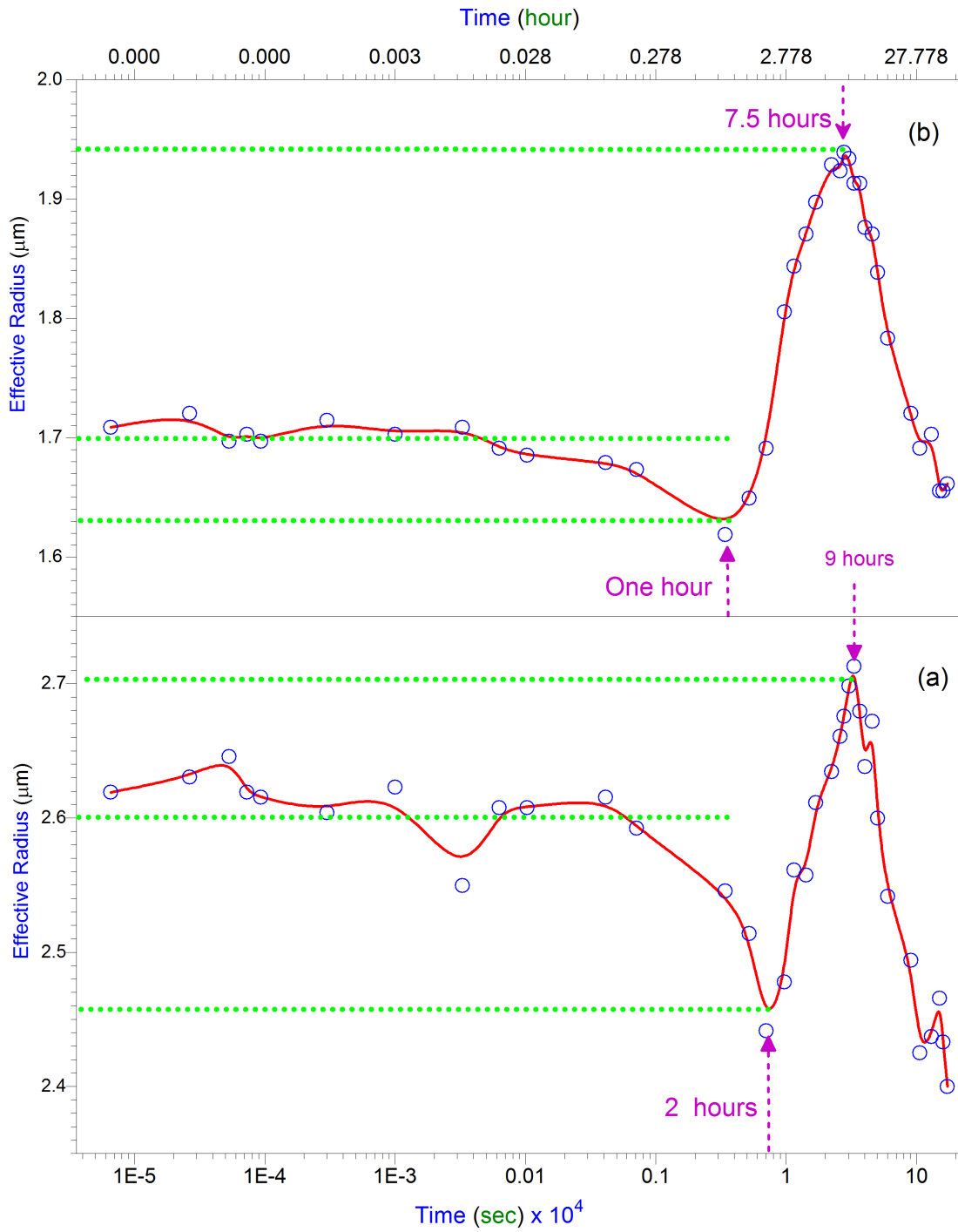


Figure 4.22: This Figure shows a comparison of effective radius of bacteria (FAMP) before infection as shown in the lower panel, and after they were infected by MS2 viruses as shown in the upper panel.

4.3 Discussions

4.3.1 FAMP Characteristics

As depicted in Fig.(4.5) that the life cycle of the FAMP is a little different compared to that of the publication [77]. Where as it can be seen in this figure, that the plateau, as shown in Fig.(4.2), which represents the stationary phase is no longer present by using ARGOS's technique and analysis, where instead of that plateau, there is one peak[†] of the growth phase occurring at the time 1.8 hour. Moreover, there is another peak at the time 26.8 hours. Furthermore, there is a valley at the time 7 hours. It follows that the stationary phase is nothing but a portion of the growth phase and the death phase, which satisfies with the theoretical concept [81, 82] of the bacteria life-cycle as seen in Fig.(4.2).

If someone wants to look in the details about the behavior of the scatterers in solution, it is necessary to check the scattered intensity at the corresponding q-regime shown in Fig.(4.5). In this figure it can be seen that the growth phase started at ~ 0.3 hour, which then reached its maximum at 12.3 hours. At this point, it appears that the stationary phase is a part of the death phase, with one stage of growth-death stage[‡] as shown in the figure. A single valley represents the end of the death stage and the next peak at 20.8 hours works as an end of a growth stage.

[†]Actually, there is another peak comes after the first one. In general we can look at both of them as a single peak regarding the large scale view.

[‡]There can be more than one stage of growth and death in this intervals base on the speed of CCD camera.

4.3.2 Effect of Temperature Change

As shown in Fig.(4.11), the trend of the life cycle of FAMP differs for the cold sample when compared to the hot one. Where Fig.(4.12) shows that the growth stage of FAMP started earlier for the higher temperature sample, which can be inferred from comparing the lower panel of the colder to the upper panel in the same figure. Also, one can notice that the time that FAMP needed to reach the maximum growth point occurred after 8 hours for the higher temperature sample compared to the colder one. This agrees with our knowledge from the biology that bio-creatures have lower activity at lower temperatures.

If someone were to look carefully at the Short Interval Zone either in Fig.(4.11) or Fig.(4.12), one would notice that the growth phase is not a straight line as it is in most biology text books and articles illustrated [83, 84]. It instead takes the shape of sinusoidal shape, which indicates that this growth phase is made of many tiny growth-death stages, or you could say tiny life cycles which take their places through the major growth phase.

4.3.3 Topology of the FAMP

It can be seen that Fig.(4.6) that the slope of the curves is changing with time as detected by ARGOS technique, which is in agreement with the behavior of this type of bacteria [80]. It was noticed that at the beginning of the experiment's run, the slope of curve was of the smallest value, then as time progresses, the bacteria's shape changed gradually until it approached the highest value of the slope at the time 12.75 hours, then the shape of the FAMP went back to a lower slope value at

time 42.75 hours where the bacteria did not come back to its original shape. This occurred because this bacteria is a new generalization which have slightly different sizes than that of the original generation. So the end of a bacteria cycle correlates with a different shape. Moreover, these shapes can be predicted based on the slope of these curves, as will be discussed later when studying the Fractal Dimension d_f .

4.3.4 Fractal Dimension of the FAMP

Figure (4.7) shows the plot of the Fractal dimension versus time. It can be seen that the curve came from a higher point at the beginning and decreased for almost 2 hours where the bacteria in this interval of time were trying to acclimate with the new environment, then the shape of the bacteria went back gradually to their original shape which is a cylinder at fractal-dimension value ~ 1.0 [80]. With the progress of the time the shape of the bacteria took the shape of 2D-objects with fractal surfaces mostly a flat dish-ship [46, 85] until it reached its most deformed in shape at ~ 12 hours, then the bacteria, because of the interaction with food and its interaction with the environment around them, started to trend towards an anticlerical shape at the end of death-phase.

4.3.5 Effective Radius

It clearly shown in Fig.(4.9), that the size of the bacteria is changing during run of the experiment could consider the 48 hours. This change of the size of the bacteria can be discussed more clearly if it could consider the big picture of all

characteristics that have been studied during this work, as shown in Fig.(4.10). It can be noticed that the size of the bacteria is correlates in someway to the change in Fractal Dimension. The first peak in total intensity(panel a), represents the end of growth phase, where the bacteria are in the healthier case, on the other hand, they are at the smaller size situation as shown in panel (d), and the they are at less shape-deformation as shown in panel (c).

4.3.6 Four Panels Chart

By looking at Fig.(4.10) we can see the whole picture of the FAMP sample during its life cycle. These four panels are depicted in the same figure so, that each panel can give a supporting explanation to the others. For example, in panel (a), the total intensity increased to form a peak at the time 2 hours, which means either the bacteria became larger in size or the concentration of the bacteria became higher!. So to figure witch of these statements is correct, that can be possible by looking at panel (d) which indicates that the bacteria's size was of small value during the life cycle. This indicates that the 2 hour peak of the total intensity is indeed a sign of higher concentration indeed. Another example is observed from panel (b), one can notice that the peak of the Root Square Difference, which can be an indication of a high dynamics, is instead consistent with panel (c), where the shape of the of the bacteria takes the shape of a saucer (close to spherical shape). This implies a less resistive force to the solvent when compared to the shape of bacteria at lower Fractal Dimension which was of a cylindrical shape in the *lag phase*. The bacteria started the growth phase moving closer to a spherical shape at the end of growth, which agrees with the photos of bacteria morphological changes taken with a microscope as shown in the literatures [86]. This also agrees with the work of Abigail J. Charest

through her use of the Phase Contrast microscope in her dissertation (2014), Civil and Environment Engineering, WPI, Worcester, Massachusetts.

4.3.7 FAMP with MS2-Infection Characteristics

As shown in Fig.(4.13), the total intensity of the scattered laser from the infected FAMP is plotted versus time in two versions, the first version was in X-Logarithm scale shown in panel (a) and the second version of this plot was in X-Linear scale as shown in panel(b). One can infer from panel (a) that the total intensity for FAMP bacteria after the infection remained constant with time until a time of ~ 0.3 hour. The growth phase then started with a sharp mounting curve until it reached the peak at time 2 hours, then immediately dropped down without forming a stationary phase which also happened in FAMP's sample only.

4.3.8 Topology of the FAMP with MS2-Infection

As shown in Fig.(4.15), the topology of the infected FAMP sample from the beginning of the sample's run until the end at after 48 hours, the lowest slope " d_f " was at time = 0 after which the d_f increased to its highest value at time 7.75 hours, where through these changes the size of the infected FAMP also changed as we will see later.

4.3.9 Fractal Dimension of the FAMP with MS2-Infection

This part is correlated to the topology in the previous section. In this part the slope of each line which is illustrated in Fig.(4.15), was plotted versus time as shown in Fig.(4.16). In this figure the Fractal Dimension decreased to its lowest value at 1.2 hours which is the shape most like the rod shape. The shape of the infected FAMP bacteria then started to gradually increasing sharply deforming from a rod shape to that of a saucer at the highest peak after 9.7 hours. The shape of these bacteria then started to slowly decrease back to the shape of a rod, but after this time the bacteria generation became smaller and weaker. As a result they could not go back to the original shape as it will be seen in the next section.

4.3.10 Effective Radius of Infected FAMP with MS2 Virus

Figure (4.17) shows the size of the infected FAMP changing with time. As shown in the figure, the size was content from the beginning of the experiment's run, then slowly reduced to have the minimum after one hour. It then increased in size sharply, hitting the maximum at 7.5 hours. After that, because of the interaction between the FAMP themselves and the virus MS2, the size decreased sharply until the curve reached an almost the minimum point.

4.3.11 Four Panels Chart of FAMP with MS2-Infection

Figure(4.18) has the full picture describing the behavior of the FAMP after it was infected by MS2 virus. The conclusion of this part is more or less the same as

discussed in page(142).

4.3.12 FAMP and FAMP-MS2-infection Gallery

Figure(4.19) shows the total intensity $\langle I \rangle$ versus time was plotted, where panel (a) is for FAMP only, while panel (b) is for the FAMP after infected with the virus MS2. Some changes to the behavior of FAMP after it infected by virus. The first noticeable change was at peak of the *growth phase* which shifted to the left, in other words, the end of the *growth phase* happened earlier at the time 7.6 hours after infection, where as, it was at 12.3 hours before infection, which means that the viruses either speed up the process of the growth, or the viruses took control over FAMP. The second change that can be seen in this plot, is that the two peaks formed in panel (a) for FAMP in the *stationary phase* have dispersed after infection as shown in panel (b), and then left with one peak with no *stationary phase* at all. The third change which occurred through this experiment, is that the growth slope and the death slope are sharper in the infection case comparing to FAMP case.

By looking at Fig.(4.20), one can see that the meaning of "sharp growth" and "sharp death" mentioned in the previous paragraph. Panel (a) represents the slope of the growth process and the slope of the death process, while panel (b) is the FAMP after infection with MS2. As one can notice, that after the bacteria were infected with viruses, the growth change became two times and a half greater than the growth change of FAMP-sample before the infection. Also, the death process of the infected bacteria in panel (b) occurred nearly four times greater than that of FAMP before infection.

Inflecting bacteria with viruses also effected on the *Fractal Dimension* of the bacteria as shown in Fig.(4.21). In this figure, the bacteria before infection is shown in panel (a) while bacteria after infection is shown in panel (b). Both panels show that the bacteria, in both cases (before and after infection), started declining in Fractal Dimension from the shape of its original shape of a rod, to the shape of thin rod (string shape) at the minimum of the curves. This occurred earlier at 1.2 hour after infection, while it was at 1.8 hour before infection with MS2 viruses. After the samples reached their minimum points taking thin-shape rods, both sample started immediately rising up passing the original morphology (rod shape) and continued to form saucer shapes "flying-saucer alike" in the middle of the increase until the curves reached the maximum deformation peak at 12.7 hours for FAMP only, and at an earlier time of 9.7 hours for infected FAMP. At the peaks of these curves, the bacteria take a shape close to spherical, which is more obvious in the infected sample when compared to the non infected bacteria. After the bacteria reached the maximum deformation at the peaks, the formation of the bacteria shape went back gradually towards rod shape again, but this formation did not reach very far for the infected bacteria, as seen from the fact that the curve stopped declining. this indicates that the infected bacteria remained in close to the "flying saucer". On the other hand, the non infected bacteria kept the formation process until it reached nearly its original shape (rod shape) at the end of experiment[§]. By looking at these two panels, one can see that the effect of the infection by MS2 viruses on the FAMP bacteria, where the virus accelerated the life-cycle process of the bacteria, so it reached the maximum three hours earlier. Also, the effective of the infection put the bacteria at the last stage of the life cycle at the time 29 hours and it built a long run plateau phase as shown in panel (b). Moreover, the infection of FAMP

[§]This experiment was chosen to run for 2 days, but it seems that it possible for the curve in panel (a) to go back to the original situation if the experiment had been run for longer time.

made the shape of bacteria takes a more spherical one at the end of growth phase when compared to FAMP's sample before infection, but the infection, on the other side, prevented the bacteria from going back to the original rod shape.

As it was described above, that infected FAMP with MS2 caused changes in the behaviors of FAMP, whether it was the trend of total intensity, dynamics of bacteria or the shape of the bacteria. So this is also true for the size (effective radius) of FAMP before infection and after the infection as was demonstrated in Fig.(4.22). In the lower panel panel (a) is FAMP before infection, while panel (b) is FAMP after infection with MS2. At the beginning of experiment's run, it was shown that there were no significant changes in the size of bacteria in either FAMP only or in FAMP after infection. As what was discussed on the effect on the Fractal Dimension, the infection with MS2 accelerated the process of change in the size of bacteria after infection. At the beginning, one can notice that the size of bacteria shrank. It seems that MS2 viruses prevent the bacteria from consuming the food and the viruses disturbed the system of bacteria so that the activities of the bacteria seem frozen as inferred from the infection panel, where the plateau line became straighter (less dynamics) as compared to the same case in the lower panel for FAMP only. Also, it can be seen that both curves (before infection and after infection) built the same minimum size values, whereas the this valley happened one hour earlier in the infected sample when compared to FAMP only. The differences between the size of the bacteria at the three locations are represented by the three horizontal dashed lines which are listed in table (4.1). It can be seen that the change in bacteria size is larger after the infection, either between the Lag phase to maximum, or between the minimum to maximum.

Table 4.1: Differences between the three major points in FAMP's effective radius plot before infection in table [A] and after infection in table [B].

	Lag Phase	Max
Min	0.14 μm	0.24 μm
Lag Phase	xxxxxxxx	0.2 μm

[A]

	Lag Phase	Max
Min	0.07 μm	0.31 μm
Lag Phase	xxxxxxxx	0.24 μm

[B]

Chapter 5

CONCLUSIONS

Studying materials by light scattering has grown rapidly, especially after the emergence of the laser in the late 1950s. Different techniques were developed since that time for applications in pure science, technology, or manufacturing.

These techniques of light scattering have focused on specific aspects of the scattered light, such as intensity measurements or a function of scattering angle, time, and /or wave length. These developments typically are optimized by trading off these aspects. Developing a new technique that attempts to optimize all major motivation for this work, with addition of a strong desire to have a customizable and a multi-functional technique*. Here, the ability to employ an Area Recording Generalized Optical Scattering (ARGOS) technique enables the collection of the most information that could be carried by the scattered light at the same time for the same sample[†].

*This can be seen more clearly in the developed software which were built for this technique.

[†]ARGOS or Argus Panoptes in Greek mythology was a giant, guardian of Io, and son of Arestor who was described as "all seeing".

The developed ARGOS system in the Order-Disorder Phenomena Laboratory of WPI contains a number of innovations. A large, translucent, screen is placed down range of the sample to convert the scattered light into spatial pattern that is captured by a digital camera imaging the entire screen. To protect the camera, a thru-beam filter (rather than a beam stop) is used that preserves the thru-beam onto each captured image for intensity calibration and image centering corrections. Finally, a time series of image can be taken in order to either average for increased spatial resolution or analyzed for dynamics information. Thus, both static and dynamics scattering experiments are performed simultaneously.

Because the entire scattering experiment is recorded digitally, new analysis algorithms may be applied to previously recorded experiments. An example of which has been demonstrated in this work. The equipment used for this work was simple and inexpensive. A He-Ne laser (633 nm, 5 mW) with a mono mounted camera (8 bit) and between them a few simple optics and the screen. A He-Ne laser was chosen because of some unique features, like, stability, and good coherence length[‡]. Also, the laser used was unpolarized laser, which allowed for more experimental configurations by using either an unpolarized source (default), or a polarized one, by adding a polarizer in the path of laser beam. The CCD camera was chosen to be a monochromatic camera since color was not important in this work but only the light intensity.

The methodology of the ARGOS is based on placing a sample in the path of laser beam, then capturing the scattered light (speckles) on a special semi-translucent screen mounted with a thru-beam filter. On the other side of this screen, a CCD monochromatic camera was placed at fixed distance from the screen to take images

[‡]Most of laser field researchers like to work in the range of the coherence.

of speckles. A LabView platform was used to control the camera, process the images, and perform all software image analysis. For the measurements and analysis, several programs were written in LabView with plugins written in C, C++, and MatLab codes. No commercial packages were available. Latex spheres (Carboxylate-modified micro spheres) of different sizes, purchased from **Life Technology**, were used to calibrate and test this technique. Based on a Mie analysis, latex spheres structural properties were measured using the static light scattering approach (time-averaged); for example, the radius of gyration by using a Guinier plot gave an accuracy of 5% for large particles ($>1.0 \mu\text{m}$). Also, the fractal dimension was equally consistent, which showed the behavior of Mie method for large particles versus small particles.

For dynamics of latex particles, a new analysis was developed in this work called the Root-Square-Difference. This new analysis method relies on the dynamics that changes same aspects of structure in the same sample, to cause changes in the speckle pattern imaged that are slower than the time between images. By taking the first image as time zero and subtracting this image from all subsequent images the changes to the speckle pattern may be quantified. This is done by taking the resulting difference image and calculating the root-mean-square intensity of the entire image. At time much shorter than the characteristic time of the sample's dynamics, the speckle pattern has not had time to change. Thus, the RSD for short time will be very small. As much long times, the maximum change to the image since time zero have occurred and so RSD between these two extremes in the form of a step-like change whose inflection point is identified or the characteristic time of the samples dynamic. Moreover, this method compliments an autocorrelation analysis of dynamics properties. The camera used in this work had a fastest time between images of 1/15 sec, and so this approach was only sensitive to dynamics

slower than this. After the ARGOS under the same experimental conditions as used for the latex particles. Also, the bacteria were studied again after infected by MS2 viruses. The life-cycle of pure *E. Coli*, revealed a new behavior, for example, the expected stationary phase for the sample showed a different behavior than what was documented in text books and publications. This phase was not observed to be a plateau as expected, but a peak followed by a decreasing oscillation. Also, the exponential phase showed different behavior than what was expected from the literature. The ARGOS technique was able to monitor the bacteria with precise time intervals and observe the shape of a sinusoidal decay in this phase. The radius of gyration and fractal dimension of the bacteria were also measured by ARGOS simultaneously and changes precisely correlated with different phases of the the life-cycle of the bacteria. All these observations of the pure bacteria showed systematic changes when infected by the MS2 virus bacteria-phage that are being constantly studied by biologists.

Future directions of this technique are promising based on the results achieved through this work. Using a faster camera with higher resolution will easily expand the spatial and the temporal light scattering . Also, using different wave-lengths will further widen the range of q vectors probed and by adding wave length detection (spectroscopy information) quasi-elastic and even inelastic scattering experiments such as temperature or pressure would add further experimental dimensions or greatly extend the utility of the technique. Also, changing the location of the screen and the incident angle of laser are options for more specialized scattering geometries and regimes. Moreover, Studying the zero-beam properties is another potential avenue for better characterization of laser systems in general.

Appendices

Appendix **A**

Programming Codes

A.1 Laser interaction with Particle Volume

This code "LPV" was built in order to show the correlation in between the concentrations and different sizes of particles. For example, if 10 particles the size $2\mu\text{m}$ were dispersed in a solvent of 1 ml of water, this correlation would be used to determine the concentration of $1\mu\text{m}$ of particles in the same amount of solvent. This is based upon the concept of what I refer to as the foot-print cross section, which states that the total area of the surface of the particles that faces the cross section of the laser beam has to be the same for different sizes.

A.1.1 LPV code

This Fig(A.1) shows the full code which is made by using LabView tools. The front panel of this code shows a clear picture about how this code works.

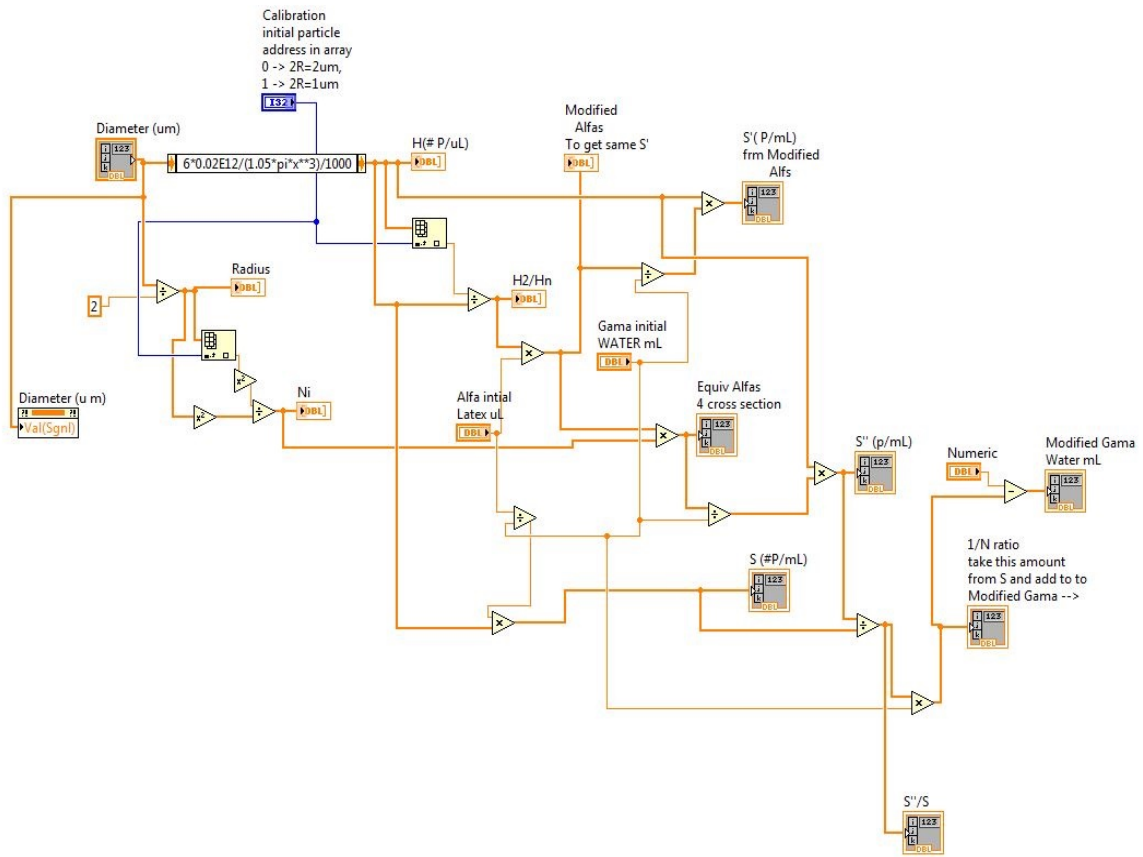


Figure A.1: This figure shows the code of the LPV program.

A.2 Taking Photos Program

This program which is referred as "TPP" was built to control the CCD to allow for photo capturing and the experiment's parameters to be held at the same time

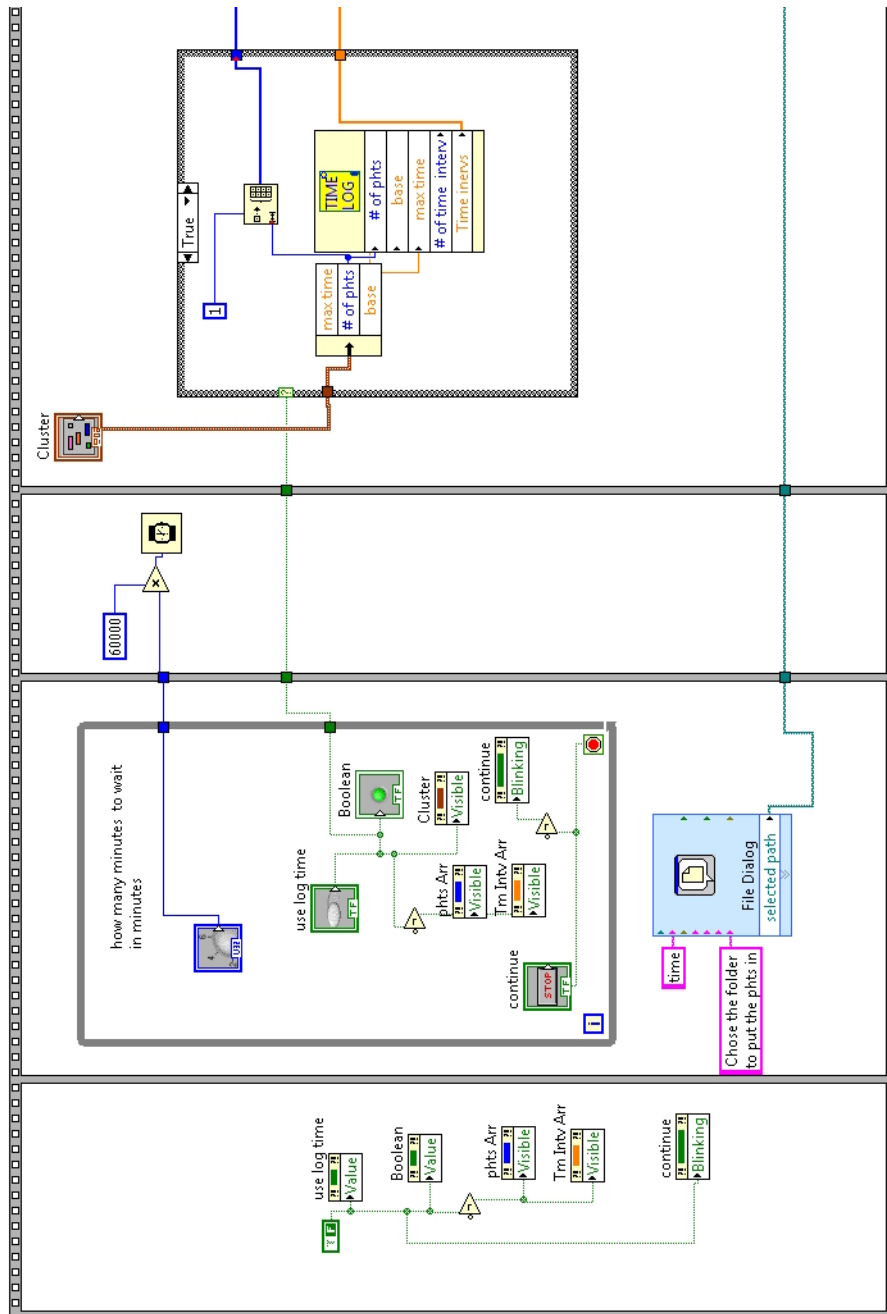
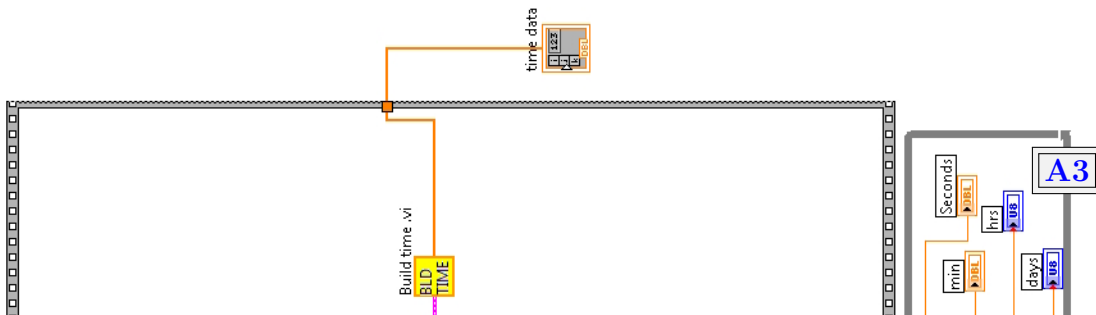


Figure A.2: This code is written to control the camera, where it was possible to chose the number of photos either in groups or individual with using different intervals of time.

A.2.1 TPP Codes



A.3 Main Analysis Program (MAP)

This program is the main program to do the analysis. It is fast and it covers most need analysis during this work or any similar works.

A.3.1 MAP Codes

This is the codes for MAP program as shown in Figs.(A.5, A.6, A.7 and A.8). The code was written in LabView platform. The panel in LabView is visual as it can be seen , so the code became too big to fit in one page, for this meson, it was necessarily to divide the code into multiple window to be embedded in the appendix.

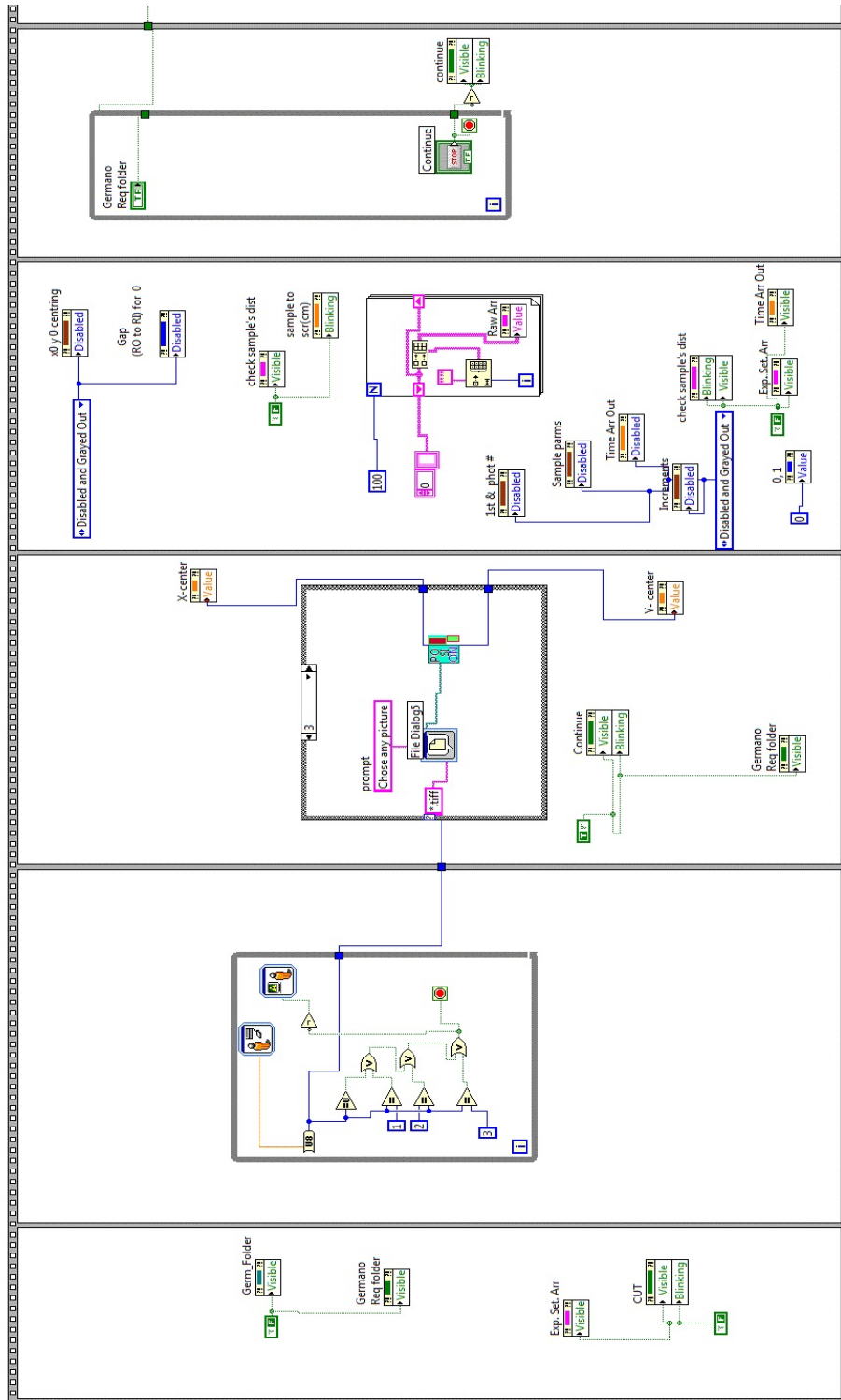


Figure A.5: Code 1

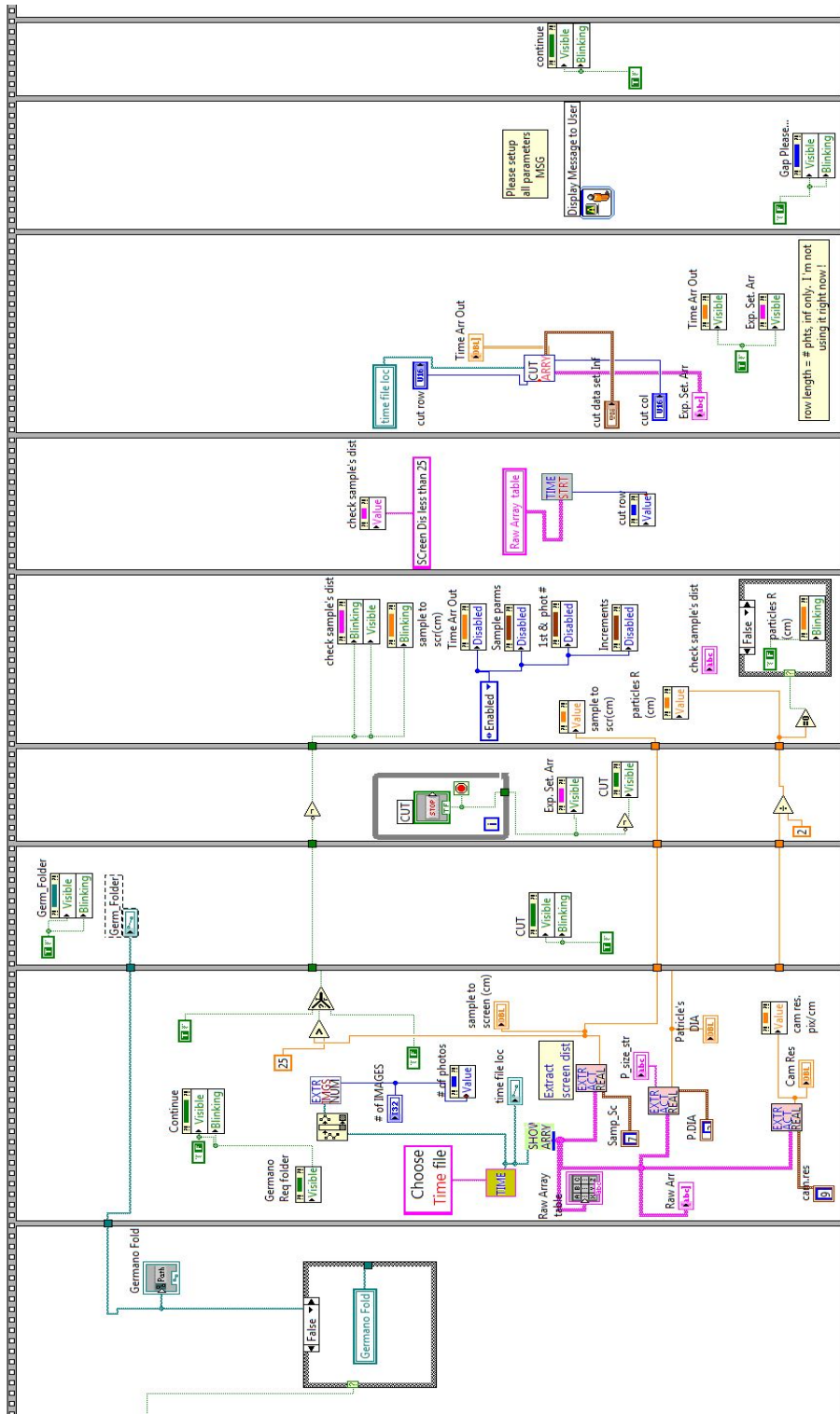


Figure A.6: Code 2

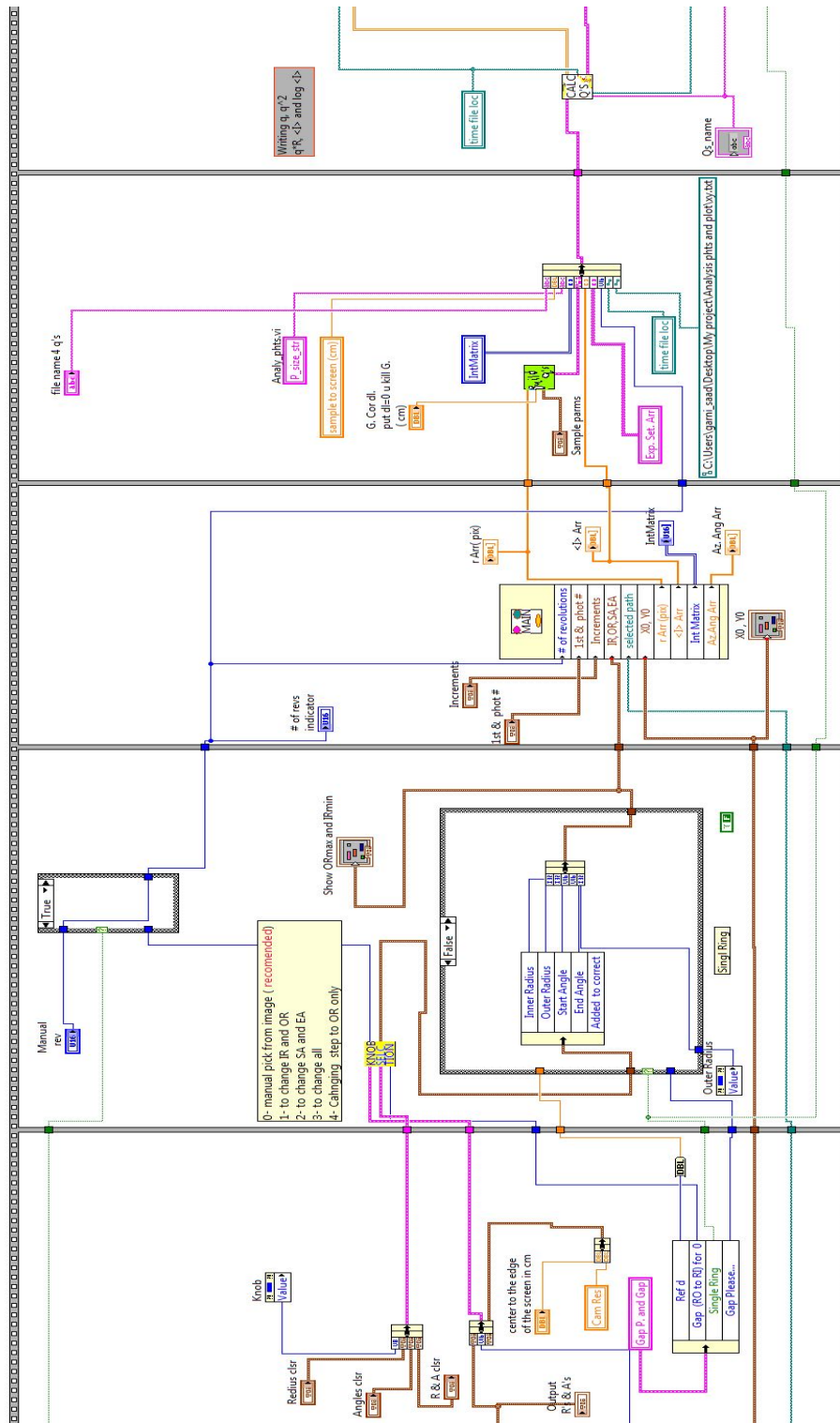


Figure A.8: Code 4

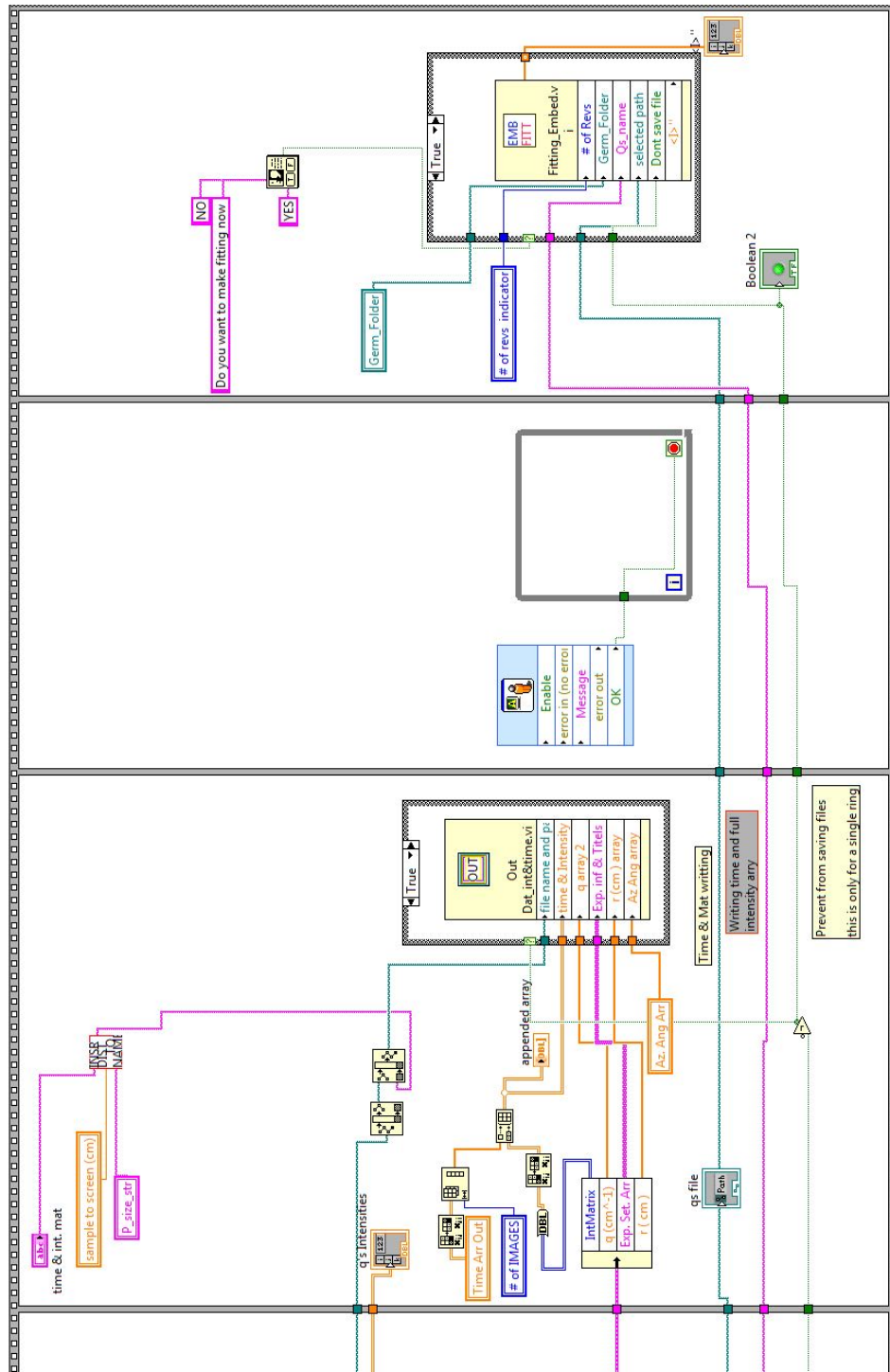


Figure A.9: All figures above are screen shoots which show the codes which were used to build the MAP program.

A.4 Box Analysis Program (OAP)

Fig(A.10) is the front panel of OAP, which is the main analysis program. This panel shows all keys and fields which are required to do the analysis as it was described in details in page(75) .

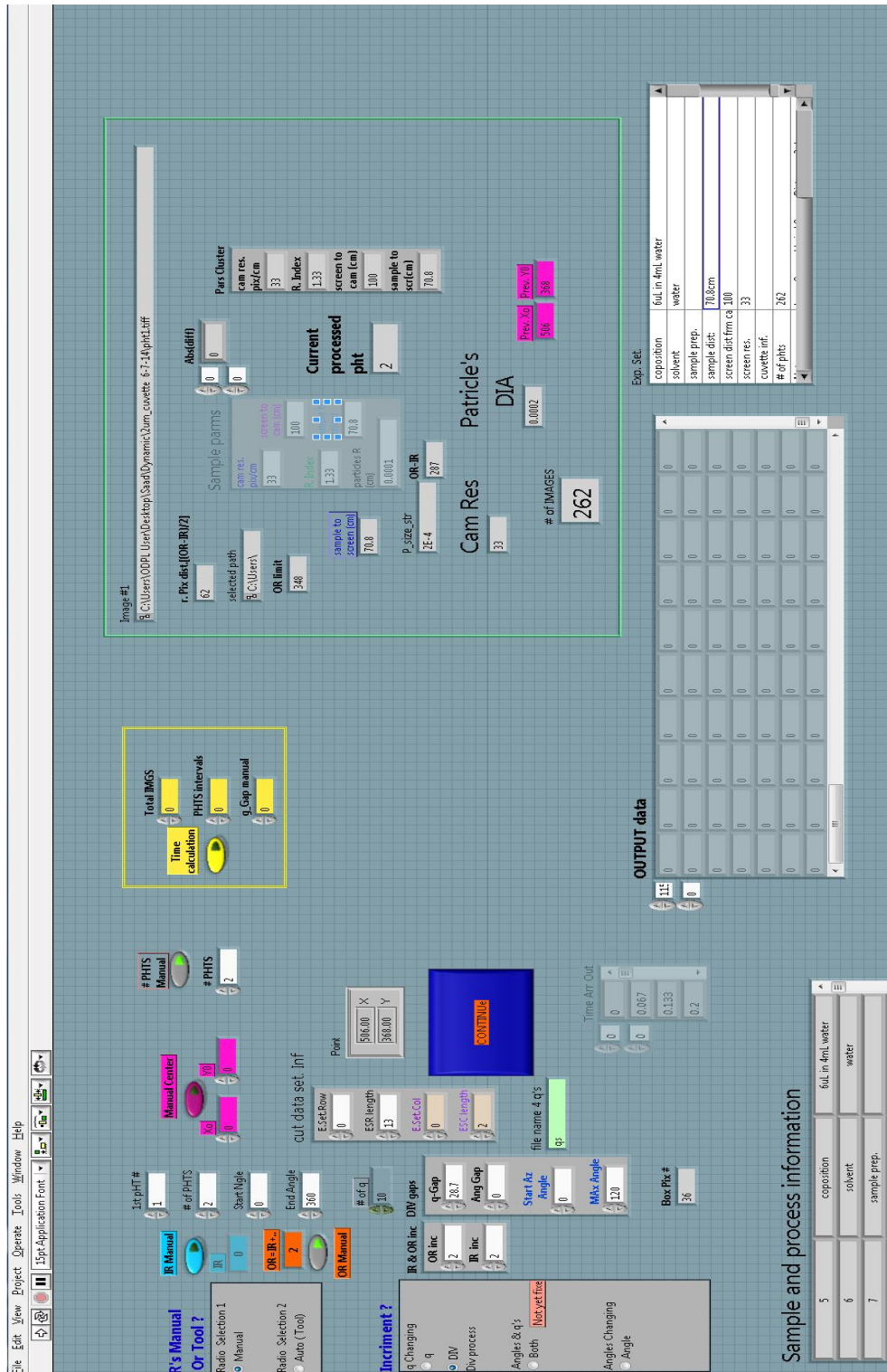


Figure A.10: This is a screen shoot which shows the front panel of OAP program.

A.4.1 Box Analysis Program codes

Since the code of this program was written in LabView environment which is a visual environment, so putting all codes in page was so difficult, so the whole code was divided into many pages as shown in Figures(A.11, A.12, A.13, A.14, A.15, and A.16).

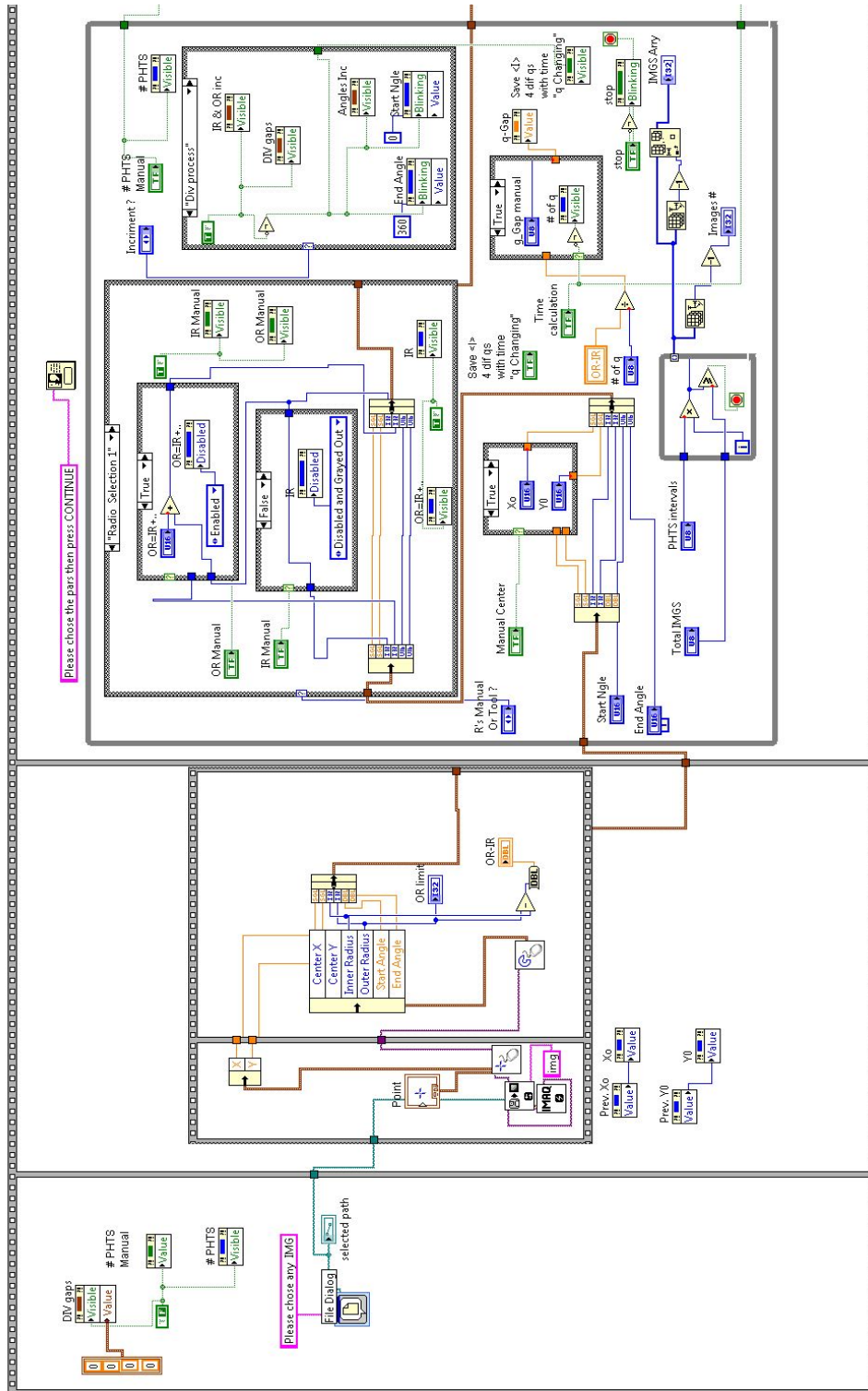


Figure A.11

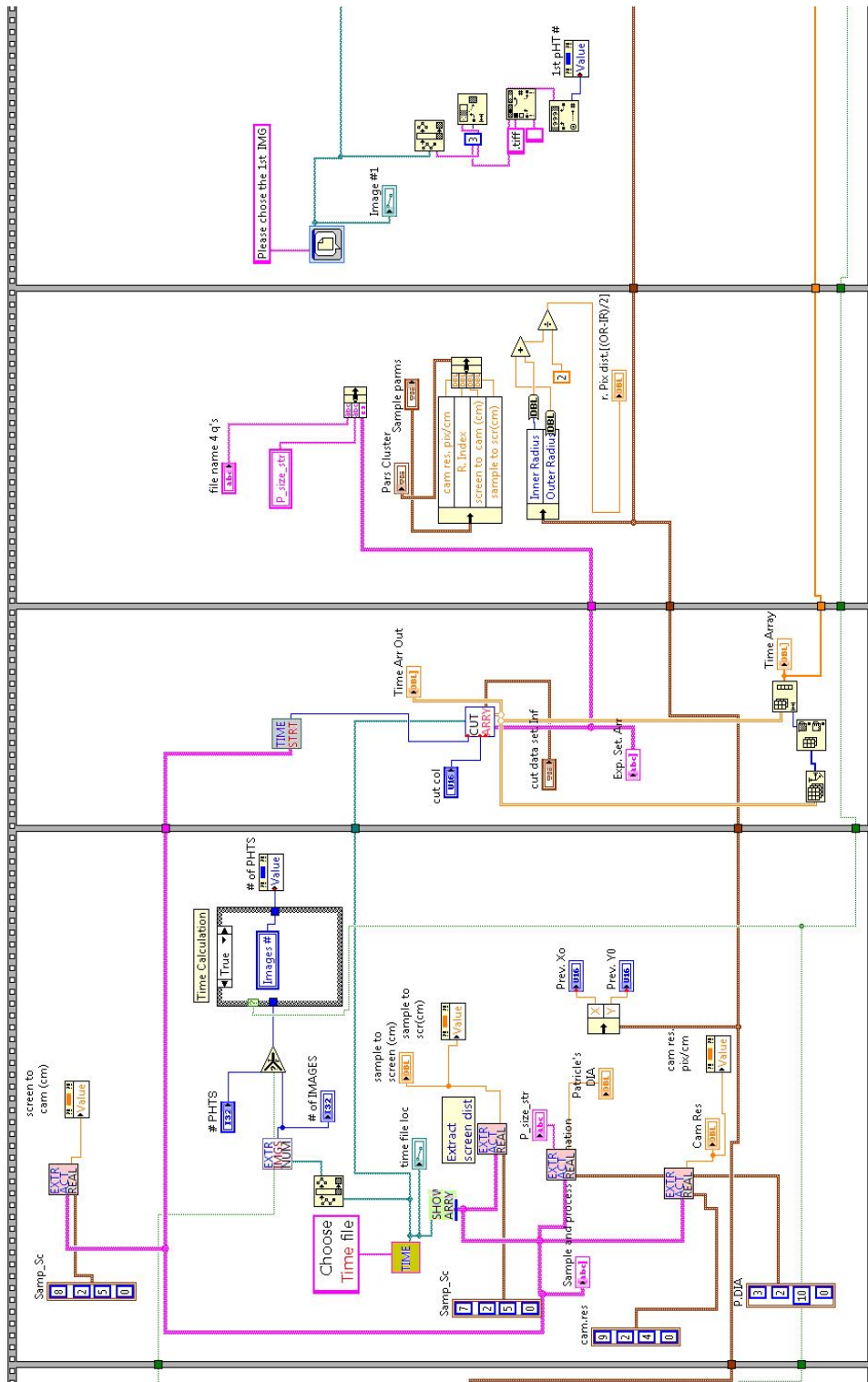


Figure A.12

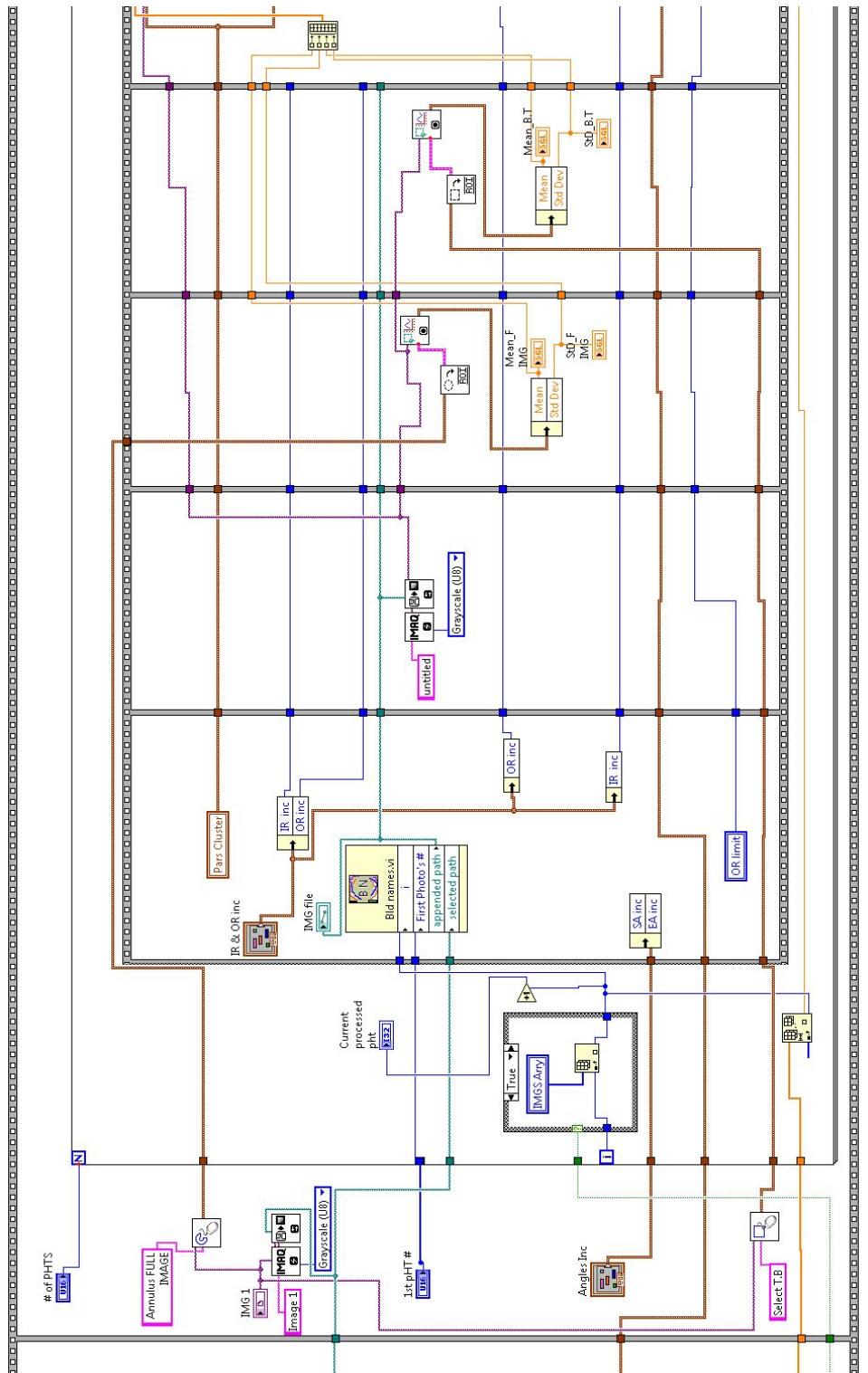


Figure A.13

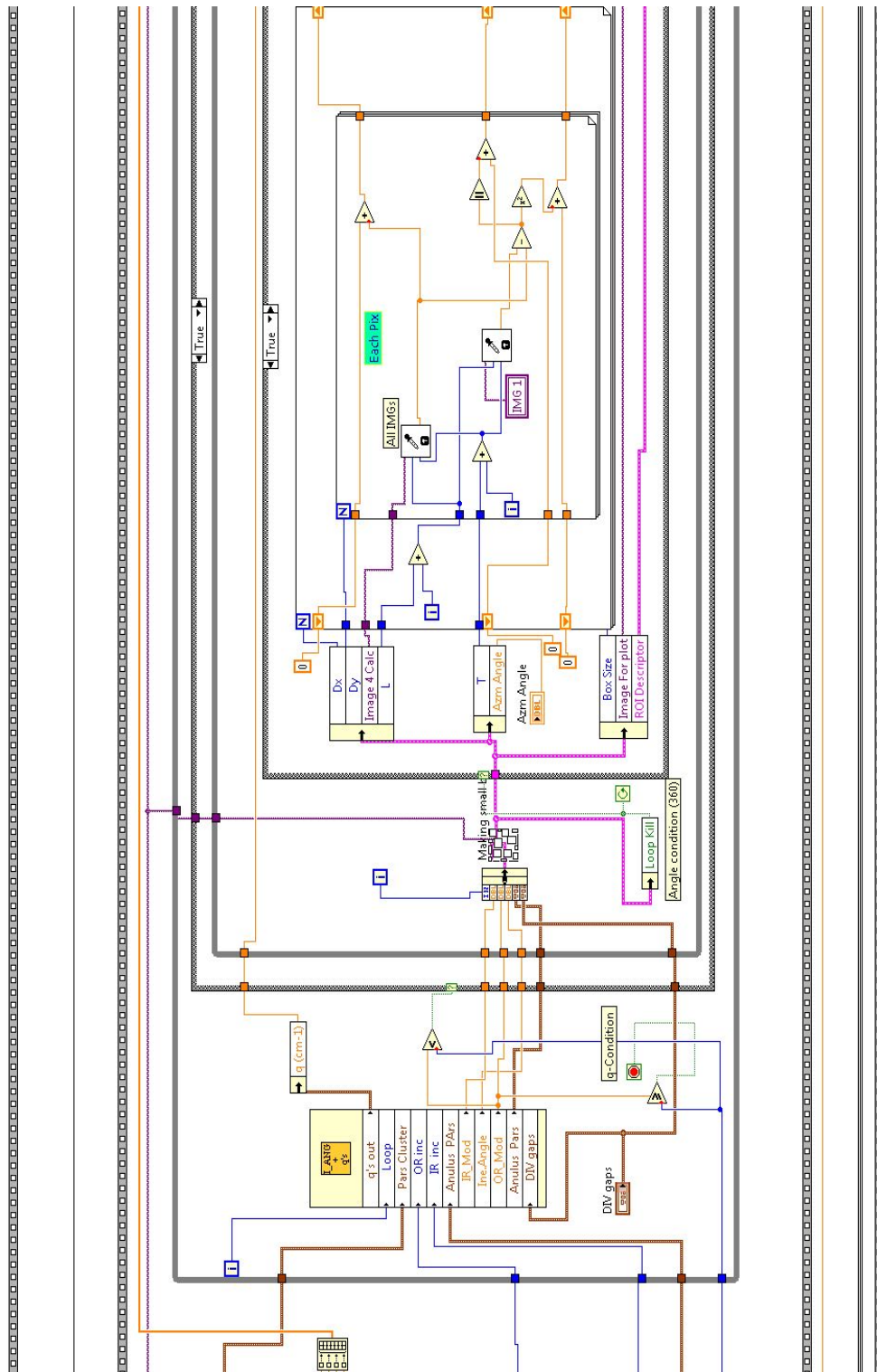


Figure A.14

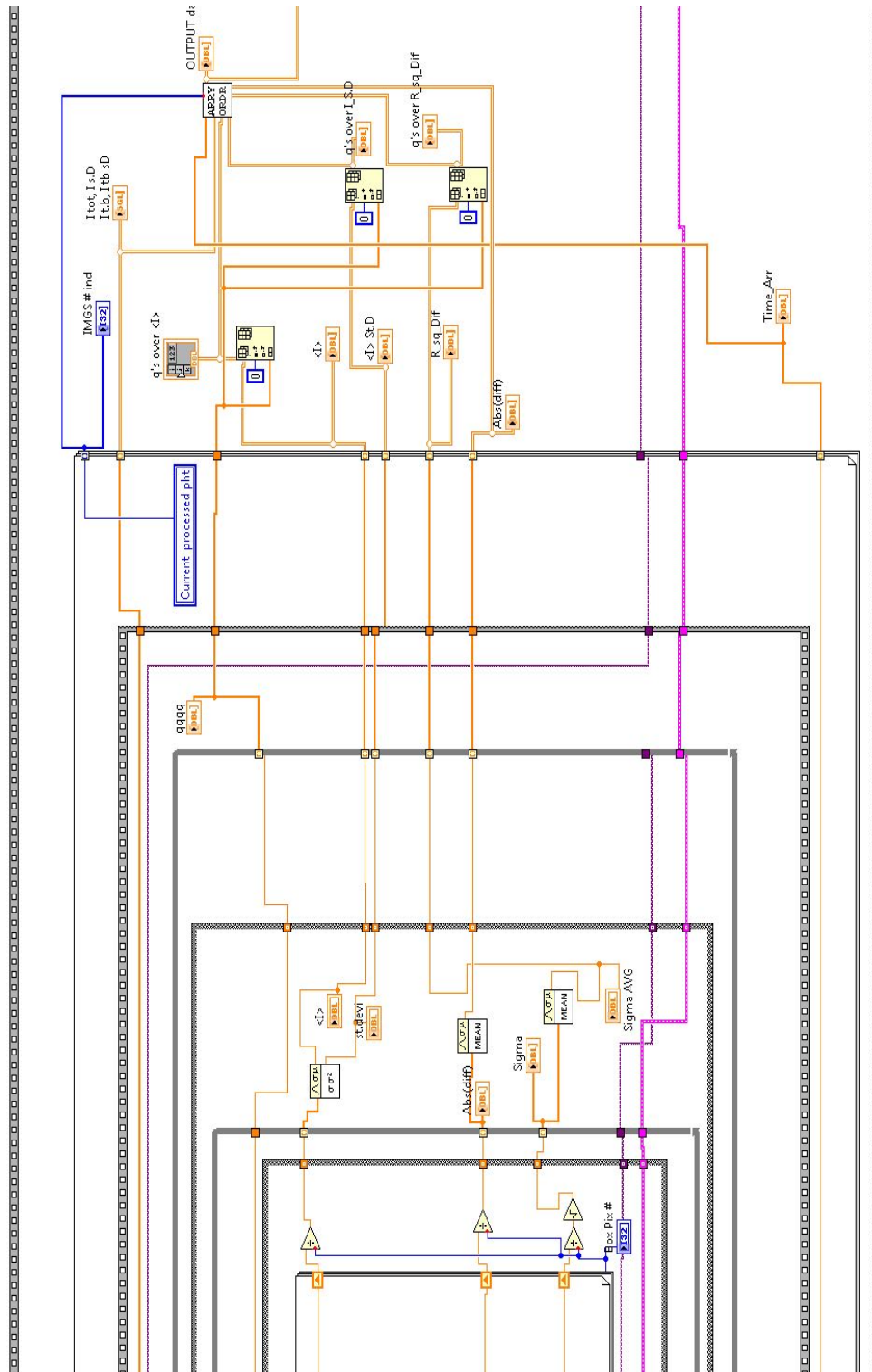


Figure A.15

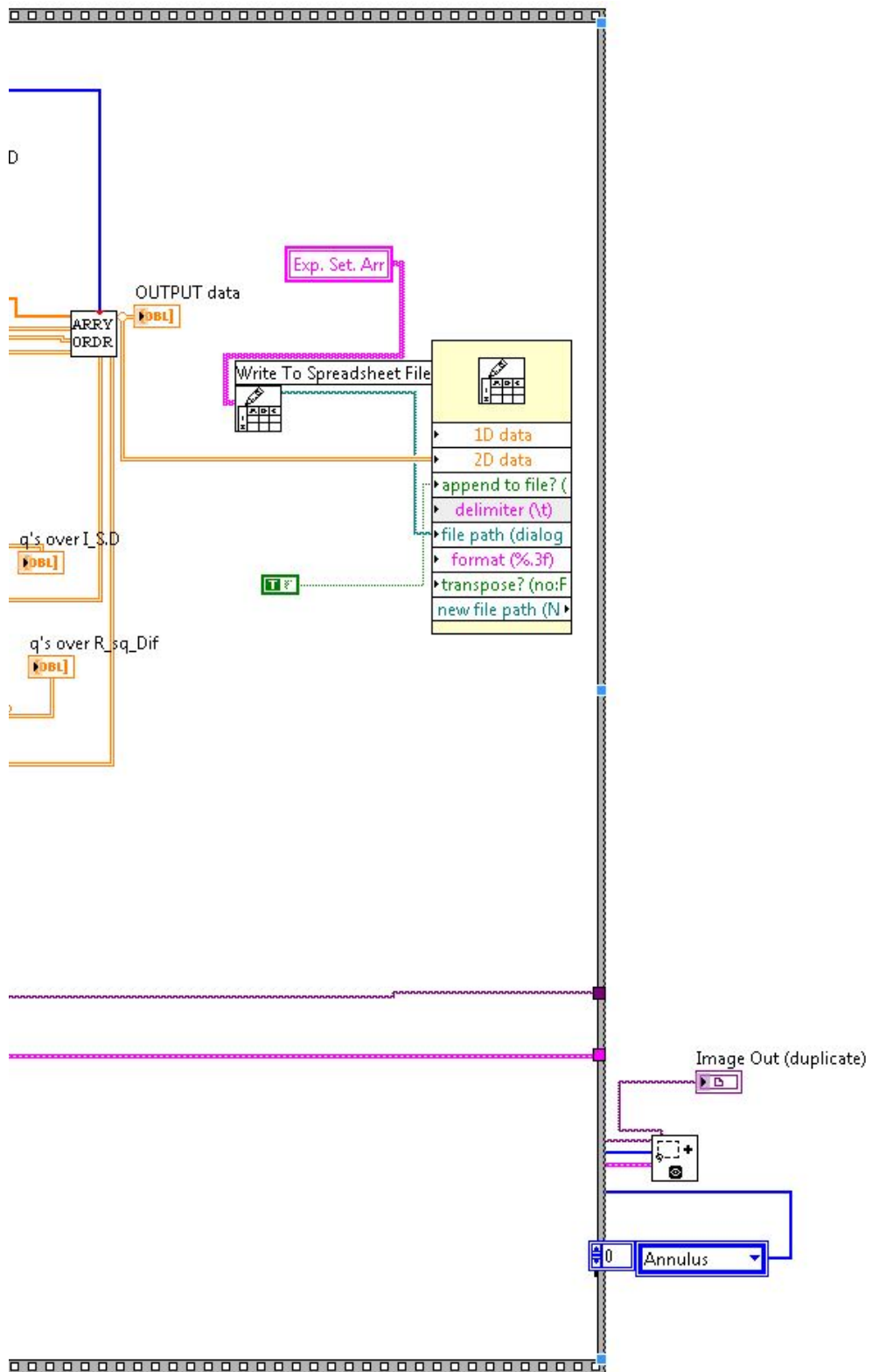


Figure A.16: These are screen shoots show the all codes which were used to build the OAP program.

Appendix **B**

Equipments and Materials

B.1 Beam Filter

The beam attenuator was made of multiple layers of filters, look at fig(B.1) with different diameters. as shown in this photo. By using this method, it was very easy to determine the exactly position of the zero-beam which causes the most distortion to the scattered speckles.

So for different intensities, a different number of layers was chosen. So that the intensity coming from the zero-beam can be reduced to an amount that ok to be distinguish by the CCD and in the same time this intensity doesn't saturate the CCD.

(a)



(b)



Figure B.1: Panel (a) shows the zero-beam coming through filters with a lower intensity, while (b) shows the multi layers which were used to build this beam attenuator

B.2 The Wafer



Figure B.2: *This photo shows the wafer which was used to carry microscope slides for cleaning and storage.*



Figure B.3: *Extra focused photo shows the groves in the wafer.*

B.3 The Sample Holder

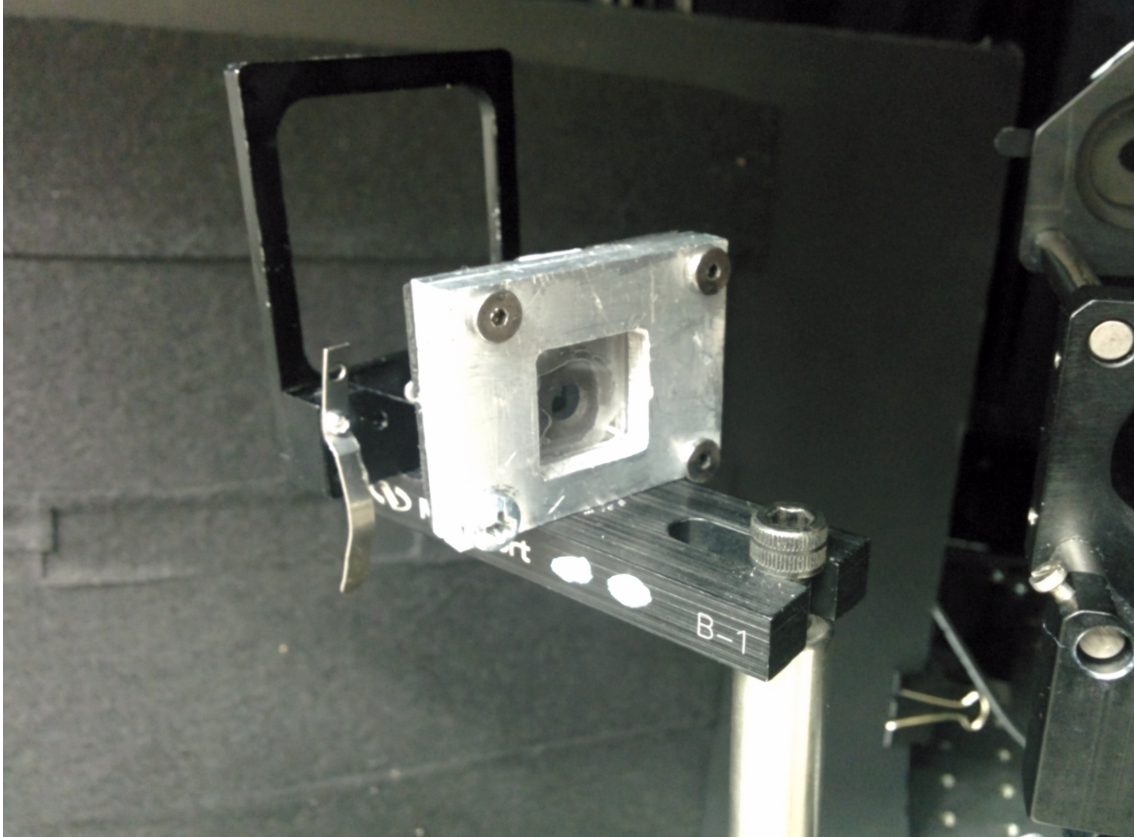


Figure B.4: A photo for the thin-planar sampler holder.

B.4 Standard Operating Procedure Sample Preparation for DLS

- Prepare Overnight *E. coli*

Check for refrigeration cultures of *E. coli* Famp. If there are none (or if they are more than 1 month old) prepare fresh cultures from frozen stocks. Make new before one month is up. Transfer no more than 6 (8 max.) times.

1. Prepare *E. coli* Famp
 2. Make two flasks
 3. Make cultures in laminar flow hood, sprayed with 40% reagent alcohol.
 4. Flame tube tops and caps and flame loop in between each use, flame loop very carefully between cultures
 - a. Add 50 mL TSB to a labeled flask: Famp Overnight
 - b. Autoclave
 - c. Add 0.5 mL 100X Strep/Amp to Famp Overnight Flask
 - d. Add 0.5 mL of refrigeration *E. coli* Famp to Famp Overnight flask
 5. Cap overnight flasks and shake/incubate at 36C at 100-150 rpm for 16-18 hrs
 6. Use after inoculation (overnight *E. coli*) or save refrigeration flasks in culture fridge (1 month)
- Prepare Log Phase *E. coli*
 1. Start 4 hr log phase *E. coli* Famp hosts from overnight *E. coli*
 2. Make Log phase *E. coli*.
 - a. Add 100 mL TSB per log-phase flask
 - b. Autoclave
 - c. Add 1 mL of 100X Strep/Amp to Famp log-phase flask
 - d. Add 0.5 mL overnight *E. coli* Famp to Famp log-phase flask
 3. Incubate at 36C, shaking at 100-150 rpm for 4 1 hours or until visibly turbid
 4. Immediately chill on ice or at 4C until ready for use
 5. Must be used within 2 hours of placing on ice
 6. For larger time window, a second set of log-phase cultures can be started an hour after the first.
 - Prepare Samples for Dynamic Light Scattering
 1. Determine sample type Bacteria Only or Bacteria and Virus

2. If bacteria only,
 - a. Add 8.9 mL of Phase PBS
 - b. Add 0.1 mL Strep/Amp
 - c. Add 1.0 mL Famp
3. If bacteria and virus,
 - a. Add 8.8 mL of Phage PBS
 - b. Add 0.1 Strep/Amp
 - c. Add 1.0 mL Famp
4. Place in beaker of water with an ice pack
5. Prepare cuvette and set up for DLS
6. If bacteria with virus, add 0.1 mL MS2 immediately prior to running the DLS
7. Run sample according to pre-determined duration Coliphage Recipes

***E. coli* :**

Tryptic Soy Broth (TSB) 1X (for small plates)

- Add 30 g tryptic soy broth to a sterile 2000 mL bottle

- Add 1000 mL Epure water

- Mix and warm to dissolve, autoclave, store refrigerated for 1 month
- Prior to sampling, autoclave 50 mL and 100 mL quantities as necessary

Antibiotics:

100X Streptomycin/Ampicillin

- Materials: Sterile beaker, (2) sterile bottles, sterile serological pipet, sterilization filter apparatus, pump
- Collect at least 100 mL of Epure water in a sterile beaker
- Add 0.15 g ampicillin to a sterile bottle
- Add 0.15 g streptomycin
- Add 100 mL Epure water using a sterile serological pipet and swirl to dissolve
- Filter sterilize into a sterile bottle
- Freeze 5 mL aliquots at -20C

Samples and Phage

Phage Phosphate Buffered Saline (PBS) Label Phage Only

- add 8.0 g NaCl to a sterile 1000 mL bottle
- add 0.2 g KH₂PO₄
- add 0.12 g KCl

- add 0.91 g anhydrous Na_2HPO_4 (or 2.9 g $\text{Na}_2\text{HPO}_4 \cdot 12\text{H}_2\text{O}$)
- bring up to 1L with Epure water
- adjust pH to 7.2-7.4 (with 1N HCl or NaOH)
- autoclave, store refrigerated for 1 year

Bibliography

- [1] SHARMA, NATTHI L AND BEHRINGER, ERNEST R AND CROMBEZ, RENE C, “A study of electric dipole radiation via scattering of polarized laser light,” *American Journal of Physics*, vol. 71, no. 12, pp. 1294–1302, 2003.
- [2] R. J. NEMANICH AND J.T. GLASS AND LUCOVSKY AND R. E. SHRODER, “Raman scattering characterization of carbon bonding in diamond and diamondlike thin films,” *American Vacuum Society*, vol. 6, p. 1783, May/June 1988.
- [3] W. J. WISCOMBE, “Improved mie scattering algorithms,” *Applied Optics*, vol. 19, no. 9, pp. 1505–1509, 1980.
- [4] RICHARD B MILES AND WALTER R LEMPert AND JOSEPH N FORKEY, “Laser rayleigh scattering,” *MEASUREMENT SCIENCE AND TECHNOLOGY*, vol. 12, p. R33R51, Feb 2001.
- [5] COX, AJ AND DEWEERD, ALAN J AND LINDEN, JENNIFER, “An experiment to measure mie and rayleigh total scattering cross sections,” *American*

Journal of Physics, vol. 70, no. 6, pp. 620–625, 2002.

- [6] CHANGSIK KIM AND NOAM LIOR AND KUNITO OKUYAMAB, “Simple mathematical expressions for spectral extinction and scattering properties of small size-parameter particles, including examples for soot and tio,,” *J. Quant. Spectrosc. Radiat. Transfer*, vol. 55, no. 3, pp. 391–411, 1995.
- [7] J. VÁVRA AND D. STOJKOVÁ AND V. CHRÁSTOVÁ , “Particle size determination of poly disperse latex by light scattering,” *Chem. zvesti*, vol. 23, pp. 481–487, 1969.
- [8] BOHREN C.F. AND HUFFMANN D.R., *Absorption and scattering of light by small particles*. New York: Wiley, 1983.
- [9] MICHAEL L. MCCONNELL, “Particle size determination by quasielastic light scattering,” *ANALYTICAL CHEMISTR*, vol. 53, pp. 1007–1008, July 1981.
- [10] BOHREN, CRAIG F AND FRASER, ALISTAIR B, “Colors of the sky,” *Phys. Teach*, vol. 23, no. 5, pp. 267–272, 1985.
- [11] MOKHTARI, T. AND KANSAS STATE UNIVERSITY. DEPARTMENT OF PHYSICS, *Studies of the Effects of Shear on Colloidal Aggregation and Gelation Using Small Angle Light Scattering*. Kansas State University, 2007.
- [12] MCCREERY, RICHARD L., *Raman spectroscopy for chemical analysis*. John Wiley & Sons, 2005.
- [13] MISHCHENKO, MICHAEL I. AND HOVENIER, JOACHIM W. AND TRAVIS, LARRY D., *Light scattering by nonspherical particles: theory, measurements,*

and applications. Academic press, 1999.

- [14] W. HELGERT AND T. WRIEDT , *The Mie Theory, Basics and Applications.* New York Dordrecht, London: Springer-Verlag Heidelberg, 2012.
- [15] MORRISON, IAN D. AND GRABOWSKI, EF AND HERB, CA, “Improved techniques for particle size determination by quasi-elastic light scattering,” *Langmuir*, vol. 1, no. 4, pp. 496–501, 1985.
- [16] CHEN, GANG, *Nanoscale energy transport and conversion: a parallel treatment of electrons, molecules, phonons, and photons.* Oxford University Press, USA, 2005.
- [17] ZIMAN, JOHN M AND ZIMAN, JOHN MICHAEL AND ZIMAN, JOHN MICHAEL AND PHYSICIST, GREAT BRITAIN, *Electrons and phonons: the theory of transport phenomena in solids.* Clarendon Press Oxford, UK, 2001.
- [18] FOX, M., *Optical Properties of Solids.* Clarendon, Oxford, England: Oxford University Press, 200.
- [19] PETICOLAS, W L, “Inelastic light scattering and the raman effect,” *Annual Review of Physical Chemistry*, vol. 23, p. 93, Oct. 1972.
- [20] FITZPATRICK, RICHARD, *Maxwell’s Equations and the Principles of Electromagnetism.* Jones & Bartlett Publishers, 2008.
- [21] KUO-NAN LIU, “A complementary theory of light scattering by homogeneous spheres,” *Applied Mathematics and Computation*, vol. 3, no. 4, pp. 331–358, 1977.

- [22] CARUTHERS, JERALD W, “On rayleigh and mie scattering,” in *Proceedings of Meetings on Acoustics*, vol. 14, p. 070001, Acoustical Society of America, 2013.
- [23] MUNDY, WC AND ROUX, JA AND SMITH, AM, “Mie scattering by spheres in an absorbing medium,” *J. Opt. Soc. Am*, vol. 64, no. 12, pp. 1593–1597, 1974.
- [24] GREEN NICOLAS G. AND MORGAN, HYWEL, “Dielectrophoresis of submicrometer latex spheres. 1. experimental results,” *The Journal of Physical Chemistry B*, vol. 103, no. 1, pp. 41–50, 1999.
- [25] QIANG FU AND WENBO SUN, “Mie theory for light scattering by a spherical particle in an absorbing medium,” *APPLIED OPTICS*, vol. 40, pp. 1354–1361, March 2001.
- [26] MILTON KERKER, *The scattering of light, and other electromagnetic radiation*, vol. 16.
- [27] WIKIPEDIA, “Scattering amplitude — wikipedia, the free encyclopedia,” 2014. [Online; accessed 6-October-2014].
- [28] PETR CHÝLEK, “Light scattering by small particles in an absorbing medium,” *J. Opt. Soc. Am.*, vol. 67, pp. 561–563, Apr 1977.
- [29] SHOJI ASANO AND MAKOTO SATO, “Light scattering by randomly oriented spheroidal particles,” *Applied optics*, vol. 19, pp. 962–974, Mar 1980.
- [30] KATKOVSKY, L. V. AND BELYAEV, B. I AND BELYAEV, YU V. AND KURIKINA, T. M. AND NESTEROVICH, A I AND SOSENKO, V. A AND

- VELLER, V. V. AND ZABIRKO, S. P. AND ZAITSEVA, V. A, “Spectropolarizational technique for detection of manmade objects in visible and near infrared spectral ranges,” in *Geoscience and Remote Sensing Symposium, 1999. IGARSS '99 Proceedings. IEEE 1999 International*, vol. 2, pp. 1381–1383 vol.2, 1999.
- [31] BERRY, H GORDON AND GABRIELSE, G AND LIVINGSTON, AE, “Measurement of the stokes parameters of light,” *Applied optics*, vol. 16, no. 12, pp. 3200–3205, 1977.
- [32] RICH WATKINS AND JOE VALLANDINGHAM, “Rayleigh scattering,” 2008. <http://home.comcast.net/~vinelandrobotics/>.
- [33] NELSON, EDWARD , *Dynamical theories of Brownian motion*. Princeton university press Princeton, 1967.
- [34] KASZUBA MICHAEL AND MCKNIGHT DAVID AND CONNAH MALCOLMT AND MCNEIL-WATSON FRASERK AND NOBBMANN ULF, “Measuring sub nanometre sizes using dynamic light scattering,” *Journal of Nanoparticle Research*, vol. 10, no. 5, pp. 823–829, 2008.
- [35] BRUCE J. BERNE AND ROBERT PECORA , *Dynamic Light Scattering With Applications to Chemistry, Biology and Physics*. 31 East 2nd st. Mineola, N.Y. 11501: Dover Publications. Inc., 2000.
- [36] MEINERS, JENS-CHRISTIAN AND QUAKE, STEPHEN R., “Direct measurement of hydrodynamic cross correlations between two particles in an external potential,” *Phys. Rev. Lett.*, vol. 82, pp. 2211–2214, Mar 1999.

- [37] N. JAKSE AND A. PASTUREL, “Ab initio based understanding of diffusion mechanisms of hydrogen in liquid aluminum,” *APPLIED PHYSICS LETTERS*, vol. 104, no. 15, p. 154101, 2014.
- [38] KARATZAS, IOANNIS, *Brownian motion and stochastic calculus*. springer, 1991.
- [39] R. XU, “Particle size and shape analysis using laser scattering and image analysis.,” *Revista Latinoamericana de Metalurgia y Materiales*, vol. 20, no. 2, pp. 80–84, 2000.
- [40] ANA M. S. MAIA AND MARCOS A. VILLETTI AND ROSANGELA R. L. VIDAL AND REDOUANE BORSALI AND ROSANGELA C. BALABAN, “Solution properties of a hydrophobically associating polyacrylamide and its polyelectrolyte derivatives determined by light scattering, small angle x-ray scattering and viscometry,” *Journal of the Brazilian Chemical Society*, vol. 22, pp. 489–500, Mar 2011.
- [41] P. DEBYE, “Light scattering in solutions,” *J. of Applied Physics*, vol. 15, pp. 338–342, Apr 1944.
- [42] ZIMM, BRUNO H, “Molecular theory of the scattering of light in fluids,” *The Journal of Chemical Physics*, vol. 13, no. 4, pp. 141–145, 1945.
- [43] D.R. VOLLET AND D.A. DONATTI AND A. IBAEZ RUIZ, “A {SAXS} study of the nanostructural characteristics of teos-derived sonogels upon heat treatment up to 1100 c,” *Journal of Non-Crystalline Solids*, vol. 306, no. 1, pp. 11 – 16, 2002.
- [44] BEAUCAGE, G., “Approximations Leading to a Unified Exponential/Power-

- Law Approach to Small-Angle Scattering,” *Journal of Applied Crystallography*, vol. 28, pp. 717–728, Dec 1995.
- [45] TEIXEIRA, J., “Small-angle scattering by fractal systems,” *Journal of Applied Crystallography*, vol. 21, pp. 781–785, Dec 1988.
- [46] WOLFGANG SCHARTL, *Light Scattering from Polymer Solutions and Nanoparticle Dispersions*. Heidelberg, German: Springer, 2007.
- [47] N.C. SANTOS AND M.A. CASTANHO, “Teaching light scattering spectroscopy: the dimension and shape of tobacco mosaic virus,” *Biophysical Journal*, vol. 71, no. 3, pp. 1641 – 1650, 1996.
- [48] SCHAEFER, DALE W. AND MARTIN, JAMES E. AND WILTZIUS, PIERRE AND CANNELL, DAVID S., “Fractal geometry of colloidal aggregates,” *Phys. Rev. Lett.*, vol. 52, pp. 2371–2374, Jun 1984.
- [49] SORENSEN, C. M., “Light scattering by fractal aggregates: A review,” *Aerosol Science and Technology*, vol. 35, no. 2, pp. 648–687, 2001.
- [50] SORENSEN, C. M. AND CAI, J. AND LU, N., “Test of static structure factors for describing light scattering from fractal soot aggregates,” *Langmuir*, vol. 8, no. 8, pp. 2064–2069, 1992.
- [51] PIAZZA ROBERTO AND DEGIORGIO VITTORIO AND CORTI MARIO AND STAVANS JOEL, “Rotational and translational self-diffusion of interacting spherical brownian particles,” *Physics Review B*, vol. 42, pp. 4885–4888, Sep 1990.

- [52] A. P. FRBA AND A. LEIPERTZ, “Diffusion measurements in fluids by dynamic light scattering, diffusion fundamentals,” *The Open-Access Journal for the Basic Principles of Diffusion Theory, Experiment and Application*, vol. 23, pp. 63.1–63.25, 2005.
- [53] GOLDMAN, LEON AND OTHERS, *Biomedical aspects of the laser*. Springer, 1967.
- [54] p. VAN DE HULST, HC, YEAR=1981, *Light Scattering by Small Particles (Dover Books on Physics)*.
- [55] CHU, BENJAMIN, *Laser light scattering*. Elsevier, 1974.
- [56] STUART, BARBARA, *Infrared spectroscopy*. Wiley Online Library, 2005.
- [57] ANDREWS, LARRY C. AND PHILLIPS, RONALD L., *Laser beam propagation through random media*, vol. 10. 2005.
- [58] ANDREWS, LARRY C AND PHILLIPS, RONALD L AND HOPEN, CYNTHIA Y, *Laser beam scintillation with applications*, vol. 99. SPIE press, 2001.
- [59] HERRIOTT, D. R., “Applications of Laser Light,” *Scientific American*, vol. 219, pp. 140–156, Sept. 1968.
- [60] JULIAN EASTOE AND PAUL BROWN AND ISABELLA GRILLO AND TIM HARRISON, “Magnetic science: developing a new surfactant,” 2012. www.scienceinschool.org/print/3631.
- [61] TURQUOIS, TRISTAN AND GLORIA, HUGO, “Determination of the absolute molecular weight averages and molecular weight distributions of alginates used

as ice cream stabilizers by using multiangle laser light scattering measurements,” *Journal of Agricultural and Food Chemistry*, vol. 48, no. 11, pp. 5455–5458, 2000. PMID: 11087501.

[62] LSinstruments, “Static light scattering,” 2013. <http://www.lsinstruments.ch/technology/>.

[63] PARKER C. A. AND REES W. T., “Correction of fluorescence spectra and measurement of fluorescence quantum efficiency,” *Analyst*, vol. 85, pp. 587–600, 1960.

[64] AZONANO STAFF WRITERS, “Dynamics light scattering - understanding the basic,” 2013. www.azonano.com/article.aspx?ArticleID=3662.

[65] S. BUZZACCARO AND E. SECCHI AND G. BRAMBILLA AND R. PIAZZA AND L. CIPELETTI, “Equilibrium concentration profiles and sedimentation kinetics of colloidal gels under gravitational stress,” *Journal of Physics: Condensed Matter*, vol. 24, no. 28, p. 284103, 2012.

[66] EDMUNDOPTICS, “Jdsu high performance helium-neon lasers,” 2013. <http://www.edmundoptics.com/lasers/gas-lasers/jdsu-high-performance-helium-neon-lasers/3053>.

[67] EDMUNDOPTICS, “Eo-0813m 1/3” ccd monochrome usb camera,” 2013. <http://www.edmundoptics.com/imaging/cameras/usb-cameras/eo-usb-2-0-ccd-machine-vision-cameras/62835>.

[68] ARTURO QUIRANTES AND FRANCISCO ARROYO AND JESUS QUIRANTES-ROS, “Multiple light scattering by spherical particle systems and its dependence

- on concentration: A t-matrix study,” *Journal of Colloid and Interface Science*, vol. 240, p. 7882, April 2001.
- [69] WEITZ, D. A. AND HUANG, J. S. AND LIN, M. Y. AND SUNG, J., “Limits of the fractal dimension for irreversible kinetic aggregation of gold colloids,” *Physics Review Lett.*, vol. 54, pp. 1416–1419, Apr 1985.
- [70] U. Kätzel, *Dynamic Light Scattering for the Characterization of Polydisperse Fractal Systems by the Example of Pyrogenic Silica*. PhD thesis.
- [71] JAE-HYUNG JEON AND NATASCHA LEIJNSE AND LENE B ODDERSHEDE AND RALF METZLER, “Anomalous diffusion and power-law relaxation of the time averaged mean squared displacement in worm-like micellar solutions,” *New Journal of Physics*, vol. 15, no. 4, p. 045011, 2013.
- [72] E. KESHMIRIZADEH AND H. MODARRESS AND A. ELIASSI AND G.A. MANSOORI, “A new theory for polymer/solvent mixtures based on hard-sphere limit,” *European Polymer Journal*, vol. 39, p. 11411150, June 2003.
- [73] J.W. VANDERHOFFA AND M.S. EL-AASSERA AND F.J. MICALEA AND E.D. SUDOL, “Preparation of large-particle-size monodisperse latexes in space: Polymerization kinetics and process development,” *JOURNAL OF DISPERSION SCIENCE AND TECHNOLOGY*, vol. 5, no. 28, pp. 231–246, 1984. Received in 21 Feb 1984 and published online in 28 Nov 2010.
- [74] W. ADAM SIGLER AND JIM BAUDER, “Total coliform and e. coli bacteria.” <http://waterquality.montana.edu/>.
- [75] SMITH, DAVID C., *Microbial source tracking using F-specific coliphages and*

quantitative PCR. PhD thesis, University of Rhode Island, 2006.

- [76] D. W. GRIFFIN AND R. STOKES AND J. B. ROSE AND J. H. PAUL III, “Bacterial indicator occurrence and the use of an f+ specific rna coliphage assay to identify fecal sources in homosassa springs, florida,” *Microb Ecol*, vol. 39, pp. 56–64, Jan 2000. Online Publication: 2 March 2000.
- [77] STEVEN E. FINKEL, “Long-term survival during stationary phase: evolution and the gasp phenotype,” *NATURE REVIEWS*, vol. 4, p. 114, Feb 2006.
- [78] GALINA RESHES AND SHARON VANOUNOU AND ITZHAK FISHOV AND MARIO FEINGOLD, “Cell shape dynamics in escherichia coli,” *Biophysical Journal*, vol. 94, p. 251264, 2008.
- [79] PIERLUIGI RESCHIGLIAN AND ANDREA ZATTONI AND BARBARA RODA AND SONIA CASOLARI, “Bacteria sorting by field-flow fractionation. application to whole-cell escherichia coli vaccine strains,” *Analytical Chemistry*, vol. 74, pp. 4895–4904, Oct. 2002.
- [80] ISHIKAWA, TAKUJI AND SEKIYA, GO AND IMAI, YOHSUKE AND YAMAGUCHI, TAKAMI, “Hydrodynamic interactions between two swimming bacteria,” *Biophysical journal*, vol. 93, no. 6, pp. 2217–2225, 2007.
- [81] NAGINA PARMAR, “Bacterial growth,” 2012. reviewed and approved by the Biology group; editor, Gaytha Langlois; lead reviewer, Gaytha Langlois ; lead copyeditors, Ruth Ifcher. and Jan Hogle.
- [82] M. H. ZWIETERING AND J. T. DE KOOS AND B. E. HASENACK AND J. C. DE WIT AND K. VAN 'T RIET , “Modeling of bacterial growth as

a function of temperature,” *Applied and Environmental Microbiology*, vol. 57, pp. 1094–1101, Apr 1991.

- [83] IVAN SONDI AND BRANKA SALOPEK-SONDI, “Silver nanoparticles as antimicrobial agent: a case study on e. coli as a model for gram-negative bacteria,” *Journal of Colloid and Interface Science*, vol. 275, no. 1, pp. 177 – 182, 2004.
- [84] I. KACENA, M. A. AND MERRELL, G. A. AND MANFREDI, B. AND SMITH, E. E. AND KLAUS, D. M. AND TODD, P., PAGES=229-234, “BACTERIAL GROWTH IN SPACE FLIGHT LOGISTIC GROWTH CURVE PARAMETERS FOR ESCHERICHIA COLI AND BACILLUS SUBTILIS,” *Applied Microbiology and Biotechnology*, VOL. 51, NO. 2, 1999.
- [85] FUJIKAWA, HIROSHI AND MATSUSHITA, MITSUGU, “Bacterial fractal growth in the concentration field of nutrient,” *Journal of the Physical Society of Japan*, volume = 60, number = 1, pages = 88-94, year = 1991, doi = 10.1143/JPSJ.60.88, URL = <http://dx.doi.org/10.1143/JPSJ.60.88> , eprint = <http://dx.doi.org/10.1143/JPSJ.60.88> .
- [86] LANGE, RV AND HENGGE-ARONIS, REGINE, “Identification of a central regulator of stationary-phase gene expression in escherichia coli,” *Molecular microbiology*, vol. 5, no. 1, pp. 49–59, 1991.